The University Of Sheffield.

Characterization of high crystal quality (11-22) semi-polar GaN overgrown on m-plane sapphire for long wavelength emitters

By:

BENBO XU

A thesis submitted in partial fulfillment of the requirements for the degree of

Doctor of Philosophy

The University of Sheffield

Faculty of Engineering

Department of Electronic and Electrical Engineering

March 2017

Abstract

High quality semi-polar (11-22) GaN has been successfully achieved by means of developing a cost-effective overgrowth approach on either nano-rod or micro-rod arrayed templates on *m-plane* sapphire using Metalorganic Chemical Vapour Deposition (MOCVD). The nano-rod or micro-rod arrayed templates are fabricated by means of using self-organized Ni nanomasks or a standard photolithography technique, respectively. Based on x-ray diffraction (XRD) and transmission electron microscopy (TEM) measurements, significant improvement in crystal quality has been confirmed as a result of the overgrowth approach. On these two kinds of templates, a fast coalescence has been obtained within a layer of less than 1 µm thick, demonstrating a much quicker coalescence process than those required by any conventional overgrowth technique (typically 10-20 µm).

The average diameter of the nano-rod template has been found to strongly influence the crystal quality and the electrical properties of the overgrown layer, which are characterized by the line-width of XRD rocking curves, strain relaxation, wafer bowing and electronic mobility. By increasing nano-rod diameter, the crystal quality of the overgrown layer is improved. In addition, by investigating the chemical etching semi-polar (11-22) GaN micro-rods using a potassium hydroxide solution on, an anisotropic and selective wet-etching has been obtained, facilitating to reduce basal stacking faults in the overgrown GaN.

Owing to the high crystal quality of the overgrown semi-polar GaN, stimulated emission has been achieved with a maximum optical gain of 130cm^{-1}, which is the first report worldwide on any semi-polar GaN grown on sapphire. Furthermore, InGaN based light emitting diodes (LEDs) from green to amber have been achieved by growth on the overgrown GaN, demonstrating a clear reduction in efficiency droop and significantly contributing to resolve the challenging “green/yellow gap” issue.

Acknowledgements

It has been a great honor for me to spend four years in the UK's pioneering research group on Nitrides in the University of Sheffield. During these years, there are a number of people who offered me great help and support. Therefore, I would like to take this opportunity to express my sincere gratitude to everyone mentioned here.

First and foremost, I would like to show my deepest appreciation to my supervisor, Professor Tao Wang for providing me with this great opportunity to work in his research team and for always giving me full guidance and support. More importantly, I couldn't thank him enough for changing my personality and helping me form a good working habit not only scientific but also in daily life.

I would like to especially thank Dr. Jie Bai for training me to operate a variety of device fabrication machines and fabricating the devices in my work. More importantly, she provided TEM characterizations for the samples of this work. Without her helping, this work couldn't complete.

I also want to express my great appreciation to Dr. Yipin Gong, Dr. Yaonan Hou, Dr. Liancheng Wang, Dr. Bing Liu, Dr. Rick Smith and Dr. Modestos Athanasiou. They offer me a lot of help and support including training me to use various systems, discussion and guidance. In addition, I owe a big thank to Dr. Liancheng Wang for proofreading the thesis for me.

There are some people who closely work with me on the project, Dr. Kun Xing, Mr. Yu Xiang, Mr. Yun Zhang, Mr. Ling Jiu, Mr. Shuoheng Shen, Mr. Zhi Li and Mr. Xuanming Zhao. I am very grateful to work with them. I also want to specially thank Mr. Yun Zhang for sharing me with the TEM images.

Finally, I would like to deeply thank my family, my dad Mr. Kezhang Xu, my mum Mrs Changchi Li and my wife Ting Su. The great belief and value you have given me enable me to get through the toughest time. Nothing in my life would have been possible without your love, support and encouragement.

Part of the results have been published or under a peer review

1. **B. Xu**, Y. Gong, J. Bai, L. Wang and T. Wang, Stimulated emission from overgrown semi-polar (11-22) GaN on sapphire substrate by using micro-rods template, *AIP ADVANCES* **7**, 045009 (2017)
2. **B. Xu**, X. Yu, Y. Gong, K. Xing, J. Bai and T. Wang, Study of high-quality (11-22) semi-polar GaN grown on nanorod templates, *Phys. Status Solidi B* **252**, 1079-1083 (2015)
3. J. Bai, **B. Xu**, F. G. Guzman, K. Xing, Y. Gong, Y. Hou and T. Wang, (11-22) semipolar InGaN emitters from green to amber on overgrown GaN on micro-rod templates, *Appl. Phys. Lett*. **107**, 261103 (2015)
4. R. M. Smith, **B. Xu**, K. Xing, Y. Gong, X. Yu, Y. Zhang, Y. Hou, J. Bai and T. Wang, An optical study of the influence of basal plane stacking faults on semipolar (11-22) InGaN/InGaN quantum wells, *NanoLett.* (to be submitted)
5. Y. Gong, K. Xing, **B. Xu**, X. Yu, Z. Li, J. Bai and T. Wang, High Efficiency Green-Yellow Emission from InGaN/GaN Quantum Well Structures Grown on Overgrown Semi-Polar (11-22) GaN on Regularly Arrayed Micro-Rod Templates, *ECS Trans.* **66** 151 (2015)
6. Y. Zhang, R. M. Smith, Y. Hou, **B. Xu**, Y. Gong, J. Bai, and T. Wang, Stokes shift in semi-polar (112-2) InGaN/GaN multiple quantum wells, *Appl. Phys. Lett*. **108**, 031108 (2016)
7. **B. Xu**, Y. Gong, K. Xing, X. Yu, J. Bai, T. Wang, Study of the strain of (11-22) semi-polar GaN overgrwon on nanorod template, UK Nitrides Consortium (UKNC) Winter Conference, University of Bristol, UK (2014)
8. **B. Xu**, X. Yu, Y. Gong, K. Xing, B. Liu, J. Bai and T. Wang, Study of electron mobility in (11-22) semi-polar GaN grown on nanorod templates, UK Nitrides Consortium (UKNC) Summer Conference, University of Sheffield, UK (2014)
9. **B. Xu**, X. Yu, Y. Gong, K. Xing, B. Liu, J. Bai and T. Wang, Study of High Quality

(11-22) Semi-polar GaN Grown On Nanorod Templates, International Workshop on Nitride Semiconductors (IWN), *Wroclaw, Poland* (2014)

10. **B. Xu**, R. Smith, Y. Zhang, Y. Gong, K. Xing, J. Bai and T. Wang, Spatial and time resolved photoluminescence of InGaN/GaN MQW with high indium on overgrown (11-22) semi-polar GaN, UK Nitrides Consortium (UKNC) Winter Conference, University of Nottingham, UK (2015)

Contents

Chapter 1 Introduction

1.1 Introduction to III-nitride Semiconductors

III-nitride (AlN, GaN, InN and their ternary alloys) compound semiconductors have attracted great attention due to their excellent chemical and physical properties for both photonic and electronic device applications, such as direct band structures, robust chemical and thermal stability, in particular their band gaps covering a wide spectral range from the deep ultraviolet (DUV) to infrared (IR) across their entire composition.

These properties make III-nitride semiconductor material suitable for the fabrication of semiconductor devices in a wide range of applications, such as general illumination, high density information storage, opto-genetics, visible light wireless communication (so-called Li-Fi), water-purification, life science, high power and high frequency electronic devices for 5G wireless communications, etc. In terms of solid state lighting applications, III-nitride based blue LED, where InGaN alloys are typically used as an active region, is the key component to fabricate a solid white lighting source due to its long lifetime, compact size and low energy consumption.

The first III-nitride based blue LED was reported by Nakamura in 1993[1]. Since then, significant progress has been achieved within last two decades. However, the major achievements made so far are still limited to the emitters in the blue spectral region, although there are a large number of publications reporting III-nitride based LEDs ranging from the deep DUV at ~210nm, through blue, to amber at 600nm.[2,3] The issues which we are facing are due to the great challenges in achieving either DUV emitters with reasonable optical performance or longer wavelength such as green/yellow emitters with accepted optical performance as a result of a number of fundamental limitations based on current c-plane III-nitride semiconductors. For the

latter, both enhanced efficiency droop and significant reduction in optical efficiency with increasing an emission wavelength lead to the so-called green/yellow gap, etc.

This chapter will start with presenting the history of the development of III-nitride materials and devices, followed by introducing current status, and then the challenges of the III-nitride semiconductors. The research objectives and thesis organization will be presented at the end of this chapter.

1.2 History of III-nitride research

In 1930s, GaN was synthesized by Juza and Hahn, aiming to study the crystal structure of GaN.[4] They obtained GaN in a powder form by means of flowing ammonia (NH_3) through liquid Ga at an elevated temperature.

H. Maruska first grew GaN on sapphire as a substrate by hydride vapour phase epitaxy (HVPE) in 1968, where gallium chloride (GaCl) and NH_3 were used to supply group III and V sources, respectively. A single crystalline GaN film was obtained at a growth temperature of 850^{o}C,[5] and the crystalline quality was improved by increasing the growth temperature to 950^{o}C. However, the surface was very rough and the crystal quality was far from satisfactory.

This situation remained unchanged until 1986, when a two-step growth approach was invented by Amano and Akasaki, representing a major technological breakthrough. This two-step growth method has become a standard growth process, widely used in growth of III-nitride materials and devices on sapphire. The typical procedure for the two-step approach by means of using metal organic chemical vapor deposition (MOCVD): a thin AlN nucleation layer with a thickness of 25 nm was prepared at a low growth temperature (500-600^{o}C) on a sapphire substrate, followed by the growth of a thick GaN buffer at a high temperature (above 1000^{o}C). With this two-step growth approach, GaN with an atomically flat surface and a step-change in crystal quality was then achieved.[6] In 1991, Nakamura modified this method by growing a thin low temperature GaN nucleation layer instead of the AlN nucleation

layer on sapphire substrates.[7]

However, any unintentional doped GaN films grown on sapphire exhibits a high background electron concentration. As a result, all the nominally undoped GaN was basically n-type, which was thought to be due to nitrogen vacancy, one of the point defects. Maruska also attempted to dope Magnesium (Mg) into GaN by HVPE in order to obtain p-type GaN, and observed an emission at 430 nm from the Mg-doped GaN in 1972.[8] However, the Mg-doped GaN did not show any p-type characteristics. Until 1989, Amano and Akasaki successfully obtained conductive p-type GaN by performing electron beam irradiation on Mg-doped GaN by accident when they carried out cathodo-luminescence (CL) measurements using scanning electron microscopy (SEM).[9] This is a very important breakthrough that makes high efficiency GaN-based LED possible to be realized. In 1992, Nakamura discovered that conductive p-type GaN can also be obtained by annealing Mg-doped GaN in nitrogen ambient at a high temperature (700-800^{o}C).[10] Compared with the electron beam irradiation approach, such an annealing process is much simpler, and can be in-situ carried out in any MOCVD reactor. Therefore, it is very cost-effective for mass production. Today, it has been widely adopted as a standard method to activate p-GaN in the III-nitride optoelectronic industry.

With the major breakthroughs mentioned above, Nakamura reported the first high brightness blue LED in 1993,[11] where InGaN layers were used as an active region and the structure was grown by a so-called two flow MOCVD.[12] In 1996-97, he also demonstrated the first room temperature continuous-wave blue laser diode (LD).[13]

In 1991, Khan firstly reported a GaN based high electron mobility transistor (HEMT), and the high electron mobility was achieved by the formation of two dimensional (2D) electron gas in AlGaN/GaN heterojunction, grown by MOCVD on a sapphire substrate.[14]

1.3 Current status

Currently, III-nitride semiconductor materials are widely used for the fabrication of short wavelength optical devices and high frequency & high temperature electronic devices, such as blue LEDs, blue LDs and high power HEMTs.[15-17] However, all the achievements made so far are limited to c-plane GaN, which is grown along a polar orientation.[18-20]

The main approach to the fabrication of white LEDs is to combine blue LEDs with yellow phosphor. As shown in Figure 1.1, over the past decade, the external quantum efficiency (EQE) of LEDs is increased from 25% to over 70%.[21] Very recently, the blue LED with an EQE of 84.3% at the output power of 47.1mW has been reported.[22]

Figure 1.2 shows an efficacy over 150lm/W achieved at a low current density in a state-of-the-art white LED. However, the efficiency droop at an increasing injection current density has been observed nearly for all LEDs, which is increasingly worse for long wavelength LEDs.

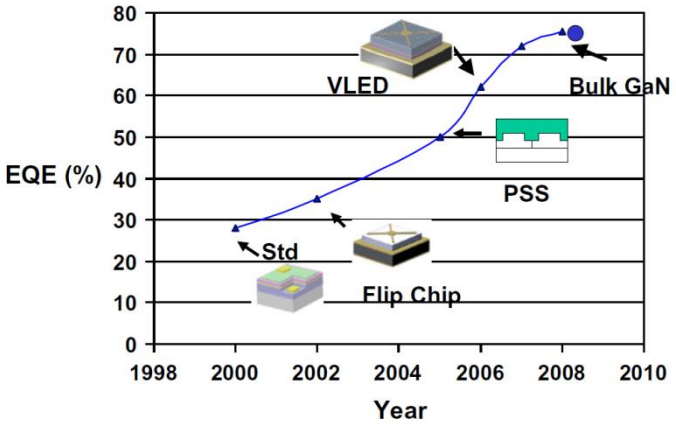

Figure 1.1 Evolution of the EQE over the past decade[23]

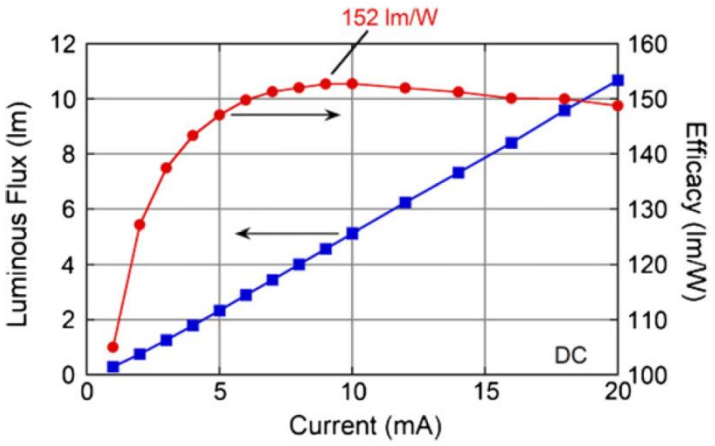

Figure 1.2 Efficacy of the state of art white LED[23]

1.4 Challenges

1.4.1 Substrate Issue

Ideally, homo-epitaxial growth of GaN would be preferred, namely, GaN grown on GaN substrates since there is no lattice mismatch. Unfortunately, unlike silicon and GaAs, standard equilibrium growth techniques cannot be used to grow bulk GaN due to its very high bonding energy.[24-26] Currently, the common way to obtain free-standing GaN substrates is to grow a thick GaN layer on a foreign substrate by a HVPE technique, which will be then separated from the substrate by using a laser lift-off process.[27] This leads to a very high cost, and thus it is not realistic to use GaN free-standing substrates for mass production, although devices with great performances on free-standing GaN substrates have been demonstrated in a laboratory level.

An alternative cost-effective way is to grow GaN films on foreign substrates, known as hetero-epitaxy. Sapphire, Silicon (Si) and silicon carbide (SiC) are the three major kinds of substrates for GaN epitaxy growth. However, in hetero-epitaxy, it is a great challenge to manage strain generated and achieve high crystal quality as a result of the lattice-mismatch and the thermal expansion coefficient difference between epi-GaN film and substrate.[28] Generally speaking, the lattice-mismatch induced strain can be released by means of the generation of defects such as

dislocations which can act as non-radiative centers, thus degrading the device performance. A large mismatch between the thermal expansion coefficients of GaN and a foreign substrate used could also cause a wafer bowing issue or even cracking after the wafer is cooled down to room temperature, as GaN is normally grown in a very high temperature (about 1000 ^{o}C in MOCVD). This issue becomes more severe when the diameter of a substrate increases.

Si substrate:

Due to the maturity of Si technology in addition to its competitive cost and availability of a large size of up to 12-inch, silicon as a substrate for the growth of GaN demonstrates its advantages, although the crystal quality of GaN on silicon needs to be further improved. Moreover, a strong demand for integrated devices further attracts huge attention on GaN growth on Si. However, Si has a cubic crystal structure which is different from the hexagonal structure of GaN. In the meantime, both the lattice-mismatch and the difference of the thermal expansion coefficients of GaN and Si are quite large, leading to a great challenge in obtaining high quality GaN films on Si.

6H-SiC substrate:

6H-SiC has a basal-plane lattice constant of 3.073 Å which is very close to that of GaN (3.189 Å). This leads to a small lattice mismatch of 3.7% between 6H-SiC and GaN. More importantly, 6H-SiC substrate has a high thermal conductivity of 3.7-4.5 W/cmK at 300K. However, the fairly high price of 6H-SiC substrates (~£500 for a 2-inch wafer) makes it less competitive for mass production, in particular the growth of optoelectronics.

Sapphire substrate

Sapphire is the most commonly used substrate for GaN growth. It has high resistivity, mechanical robustness and optical transparency. Additionally, it is also cheap. More importantly, semi-polar and non-polar GaN can be grown directly on

sapphire with different orientations. All these properties make sapphire a very attractive substrate for mass production of GaN-based devices. However, the lattice mismatch and the thermal expansion coefficient mismatch between sapphire and GaN are as high as 13% and 34%, respectively.

1.4.2 Quantum-confined Stark effect (QCSE)

Quantum well (QW) structure is commonly employed in optoelectronic devices such as LEDs and LDs. A QW structure consists of a thin layer with a narrow band gap servicing as a QW sandwiched by two barrier layers with wide band gaps. Figure 1.3 shows a typical band structure of an InGaN/GaN single QW (SQW) structure in a case without any internal electrical fields. For III-nitrides semiconductor based optoelectronics, either InGaN/GaN or AlGaN/GaN QWs are commonly used as an active region.

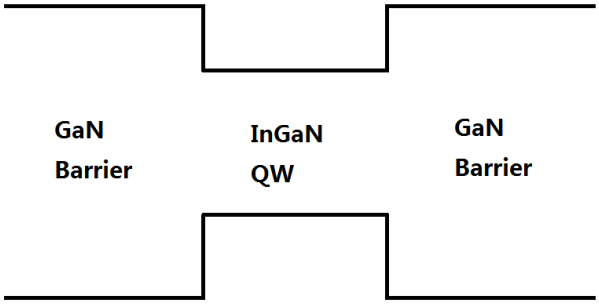

Figure 1.3 band structure of an InGaN/GaN SQW structure in a case without any internal electrical fields

However, in any III-nitride multiple quantum well (MQW) or SQW structures grown on a standard c-plane surface, this polar orientation poses an internal polarization including spontaneous and piezoelectric polarizations on the optical properties of the QW structures. Spontaneous polarization is induced as a result of an intrinsic asymmetry of a wurtzite crystal structure,[29-32] while piezoelectric polarization is generated due to a lattice-mismatch induced strain. As shown in Figure 1.4, the built-in electric fields generated as a result of the internal polarization drive

the wave functions of electrons and holes in opposite directions, tilting both the conduction and valence bands and thus leading to a reduction in the overlap of the wave functions of electrons and holes. Consequently, based on Fermi' golden law, the matrix element for the electron-hole recombination is reduced, resulting in an increase in long radiative recombination time and thus a reduction in quantum efficiency. In the meantime, it also leads to a red-shift in emission energy. This phenomenon forms a mechanism for generation of QCSE on c-plane InGaN/GaN or AlGaN/GaN MQWs.

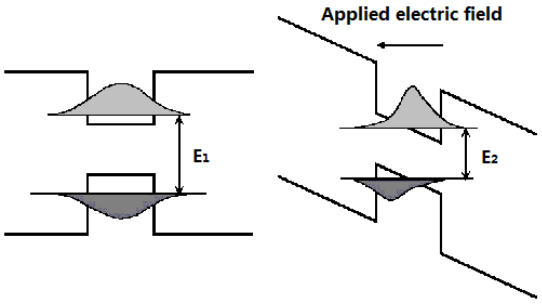

Figure 1.4 Schematic of QCSE

In order to obtain LEDs in the visible wavelength region, an InGaN/GaN MQW as an active region is adopted. Longer wavelength requires higher indium content in InGaN, leading to an enhanced lattice mismatch and thus stronger QCSE. One way to eliminate QCSEs is to manage the strain in InGaN/GaN structures, using strain relaxing buffer layers such as super-lattices and nanostructures.[33-36] Another way is to grow InGaN-based structures along non-polar or semi-polar orientations. For example, when an InGaN layer is grown perpendicular to the c-axis, i.e., along a non-polar orientation, the piezoelectric fields can be reduced to zero and thus the recombination rate can be greatly enhanced.[37]

1.4.3 Efficiency droop

Another fundamental limit is the efficiency droop which occurs to all current InGaN LEDs, resulting in a significant reduction in internal quantum efficiency (IQE)

with increasing injection current. This issue becomes more severe as the emission wavelength shifts towards the green/yellow spectral region. As shown in Figure 1.5, the efficiency droop can be observed in violet, blue and green InGaN LEDs. The origins of the efficiency droop are still under a debate in the III-nitride community with many proposed models including indirect Auger recombination,[38] current leakage,[39] and density affected defect recombination (DADR).[40,41]

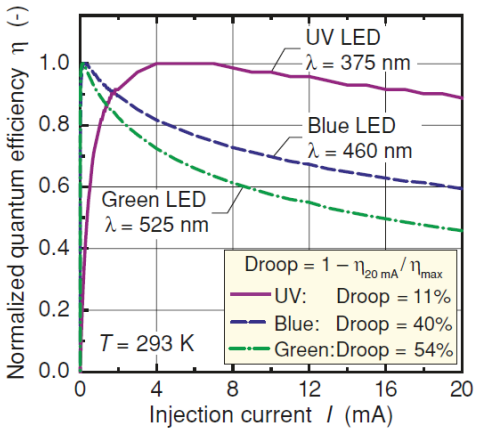

Figure 1.5 Efficiency droop of InGaN MQW based LEDs by Cho et al.[39]

The model based on indirect Auger recombination was proposed by Shen et al in 2007.[42] An Auger recombination process requires three carriers, either one electron and two holes (ehh) or one hole and two electrons (eeh). Figure 1.6 shows the process of the Auger recombination. As an electron recombines with a hole, instead of emitting a photon, this energy released is transferred to a second electron and excites the electron into a higher energy level.

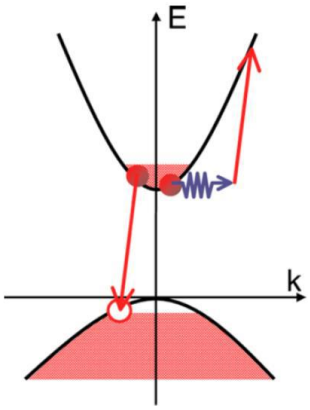

Figure 1.6 Schematics of Auger recombination[43]

In 2013, Iveland et al reported a direct observation of high energy electrons associated with an indirect Auger recombination process in an InGaN LED device

under electrical injection.[38] In his work, the device was cleaved in a vacuum chamber and coated with cesium. When electrons have sufficient energy to excite cesium atomic transitions, under a high injection current density, the cesium electroluminescence can be observed if an Auger recombination process occurs.

1.4.4 Green/yellow gap

III-nitride semiconductors are excellent candidates for the fabrication of visible LEDs, since the In compositions in InGaN QW can be adjusted to obtain emission wavelength covering the whole visible spectrum. However, when the emission wavelength extends toward longer wavelength region such as green and yellow, the optical efficiency of LEDs is significantly reduced as higher indium content is required.[44] Firstly, InGaN layer with high In composition requires a lower growth temperature, which results in a significant reduction in crystal quality. Secondly, the higher In composition in InGaN, the larger lattice mismatch between InGaN QW and GaN barrier. As a result, the strain-induced QCSE becomes more severe. Furthermore, there also exists an indium incorporation issue when InGaN is grown on a c-plane GaN surface.

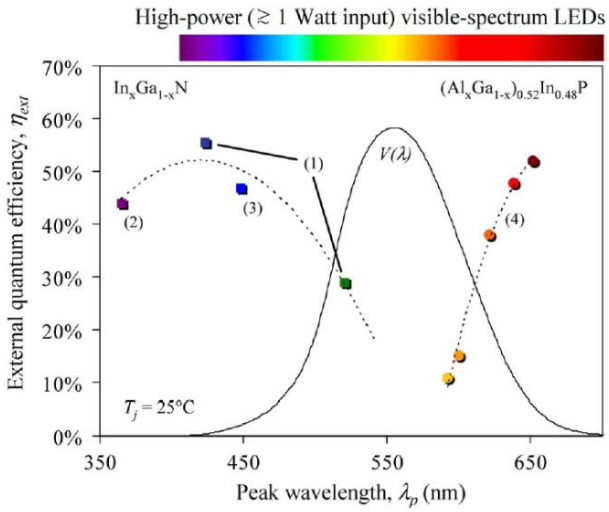

Figure 1.7 EQE at various wavelengths[45]

Figure 1.7 show the EQE of current LEDs as a function of wavelength provided by Krames et al.[45] The optical efficiency of III-Nitride LEDs show a significant

reduction with increasing wavelength from blue to green/yellow, whereas III-Phosphide shows a reduction in optical efficiency with reducing wavelength from red to green/yellow, forming a gap which is so-called 'green/yellow gap'.

1.5 Motivation and research objectives

The Intergovernmental Panel on Climate Change (IPCC) states that carbon emission is one of the main causes of the climate change since the start of the industrial revolution.[46] Currently, a traditional approach still dominates electrical power generation plants, leading to a major carbon emission source. General lighting illumination holds a big share of the civil power consumption, and it is currently dominated by employing traditional lighting sources, such as fluorescent tubes or incandescent lamps, which are both neither efficient nor environmentally friendly.

Compared with these conventional lighting sources, solid state lighting sources, which are fabricated mainly based on visible LEDs, are energy-saving and environmentally friendly. LEDs also have a number of major advantages compared with those traditional lighting sources, such as long lifetime (25 to 100 thousand hours), robust, compact size (~1cm^2), etc. InGaN-based LEDs can cover the complete visible spectral region by tuning Indium composition, making InGaN-based LEDs become an ideal next generation opto-electronic device for general illumination. High brightness and high efficiency InGaN-based LEDs with emission color from blue to amber color have attracted great research attention, which is one of the aims for this Ph.D. work.

Considering the issues discussed in section 1.4, growth of semi-polar (11-22) GaN on sapphire becomes a promising approach to achieve high efficiency InGaN-based LEDs. Firstly, semi-polar (11-22) GaN is expected to reduce the QCSE and thus improve the quantum efficiency of InGaN LEDs. Secondly, semi-polar (11-22) facet is expected to be favorable for incorporating high indium into GaN which is particularly required to achieve longer wavelength such as green and yellow LEDs. In addition, sapphire still remains the major substrate due to its competitive cost. Our

group has started the research in this area since 2009, and has developed an overgrowth technology based on nano-rod or micro-rod arrayed templates on sapphire, which has led to achieving high quality semi-polar (11-22) GaN.

The objectives of the research in this thesis are: I) study the influence of GaN nano- or micro- rod arrayed templates on crystal quality and electrical property of the overgrown semi-polar (11-22) GaN; II) investigate chemical wet etching processes on the GaN micro-rod arrayed templates which will be further used for overgrowth; III) for the first time demonstrate a stimulated emission optically pumped on our high quality overgrown semi-polar GaN, validating the excellent crystal quality of semi-polar GaN; IV) fabricate and characterize electrically injected semi-polar GaN-based LEDs with emission wavelengths ranging from green to amber, showing a significant reduction in both QCSE and efficiency droop compared to c-plane GaN-based LEDs.

1.6 Thesis organization

This thesis contains 8 Chapters:

Chapter 1: A brief history and current challenges of III-nitride semiconductor research are introduced, and research motivation of this thesis is presented.

Chapter 2: The backgrounds of semiconductors including III-nitride semiconductors are introduced. The fundamental properties and advantages of semi-polar (11-22) GaN are also expounded.

Chapter 3: The experimental techniques related to this work are introduced, including Metal-Organic Chemical Vapor Deposition (MOCVD), material characterizations (structural, electrical, and optical).

Chapter 4: The influence of the nano-rod diameter of the nano-rod arrayed templates on overgrown (11-22) GaN has been investigated in detail.

Chapter 5: A chemical treatment approach has been developed on micro-rod arrayed template prior to overgrowth.

Chapter 6: A stimulated emission has been achieved on our overgrown (11-22) semi-polar GaN, which is the first report so far on any semi-polar GaN on sapphire. An optical gain has been measured and discussed in detail.

Chapter 7: Semi-polar (11-22) GaN-based LEDs with an emission wavelength from green to amber have been successfully achieved on our overgrown (11-22) GaN. Details about growth, device fabrication and characterization have been presented.

Chapter 8: Conclusion and future work are provided

Chapter 2 Background

2.1 Semiconductors

In terms of band structure, semiconductor can be divided into two types, namely, direct band gap semiconductor and indirect band gap semiconductor. If the minimal potential of the conduction band of a semiconductor material shares the same momentum with the maximal potential of its valence band, it is defined as direct band gap semiconductor. Otherwise, it is defined as indirect band gap semiconductor. Figure 2.1 show typical band diagrams of a direct and an indirect semiconductor, respectively.

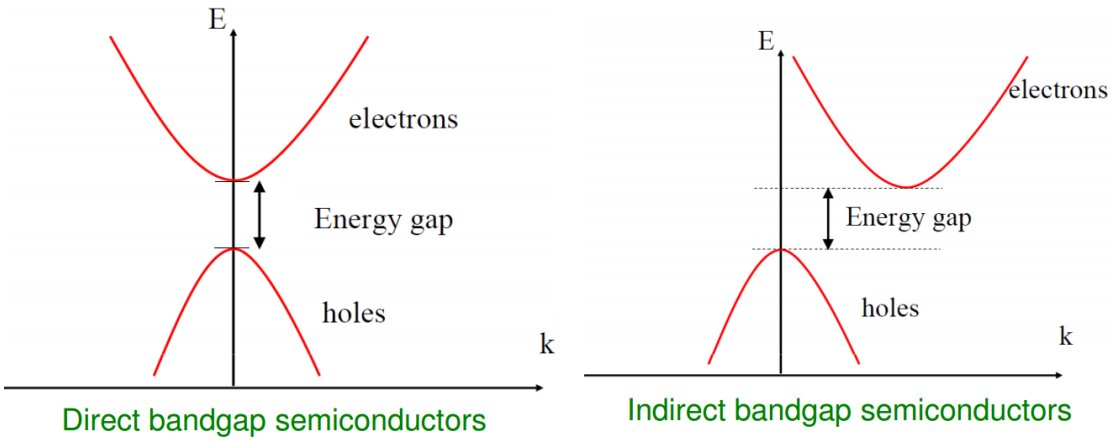

Figure 2.1 Band diagram of direct/indirect semiconductors

After optical or electrical excitation, electrons in the conduction band recombine with holes in the valence band and then emit photons, which is called radiative recombination. To satisfy the conservation of both energy and momentum, the photons have the energy which is equivalent to the band gap. For a direct bandgap semiconductor, there is no any extra momentum involved. For an indirect band gap semiconductor, extra momentum is required in order to satisfy the momentum conservation for the recombination of electron-holes, where the extra

momentum is provided through phonons. Therefore, the radiative recombination process cannot be carried out so efficiently as that in a direct bandgap semiconductor. Consequently, indirect band gap semiconductor materials are not ideal for being fabricated into efficient emitters. III-nitride semiconductors (AlN, GaN, InN and their alloys) all have direct band gap structures across their entire composition, and therefore can be used for the fabrication of high efficient emitters.

2.2 III-nitrides semiconductors

Figure 2.2 show the band gaps of all the semiconductors as a function of their lattice constants. Homo-epitaxial growth of III-arsenide and III-phosphide based semiconductors have been well-established, leading to high performance optoelectronics. However, the major achievements based on III-arsenide and III-phosphide optoelectronics are fundamentally limited to the infrared and red spectral range. III-nitride semiconductors have direct band gaps across a wide range from ~0.7 to 6.2 eV, corresponding to the emission wavelengths from deep UV to infrared.

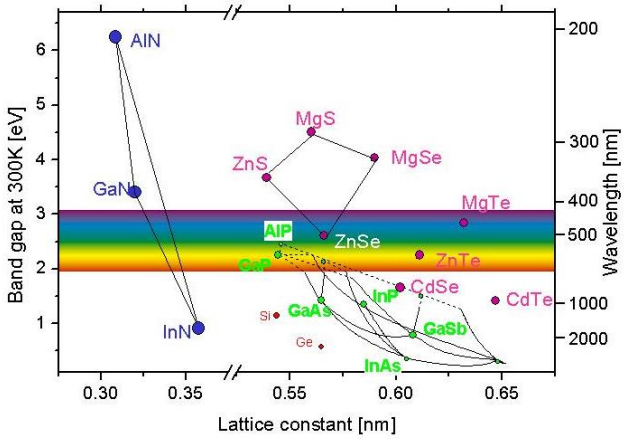

Figure 2.2 Band gaps, emission wavelengths and lattice constants of semiconductors at room temperature[47]

2.2.1 Crystal structure of III-nitrides

III-nitride semiconductors can exist in two main kinds of crystal structures: hexagonal wurtzite structure which is stable and cubic zincblende which is metastable structure, respectively. The wurtzite structure is more commonly seen for III-nitrides and suitable for practical applications, as shown schematically in Figure 2.3. The GaN or InGaN samples studied in this thesis all have the wurtzite structure.

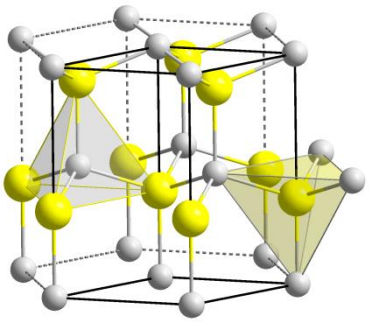

Figure 2.3 Schematic of a wurtzite crystal structure[48]

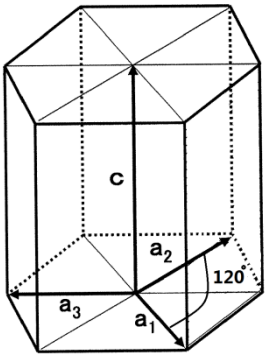

Figure 2.4 Schematic of Mill indices in a hexagonal unit cell

Lattice planes in a crystal structure can be described by means of using three integers h, k, and ℓ, namely, the Miller indices, which are generally used to denote the family of planes orthogonal to $h\mathbf{b_1}+k\mathbf{b_2}+l\mathbf{b_3}$, where $\mathbf{b_i}$ is a reciprocal lattice vector in a unit cell. For a wurtzite structure, four integers (i.e., *hkil*) are typically used as shown in Figure 2.4, where the three vectors in a basal plane $\mathbf{a_i}$ are always angled at 120° to each other, and the fourth vector is perpendicular to the basal plane. Actually, a three-index notations (*hkl*) can also represent a crystal plane or a direction in a

wurtzite crystal structure, as $i = -(h + k)$. For example, (11-22) is equivalent to (112). Additionally, the notation [*hkl*] denotes a direction orthogonal to a crystal plane (*hkl*).

Figure 2.5 shows some common planes in an III-nitride wurtzite structure, which are named as r-, m-, c-, and a- planes.

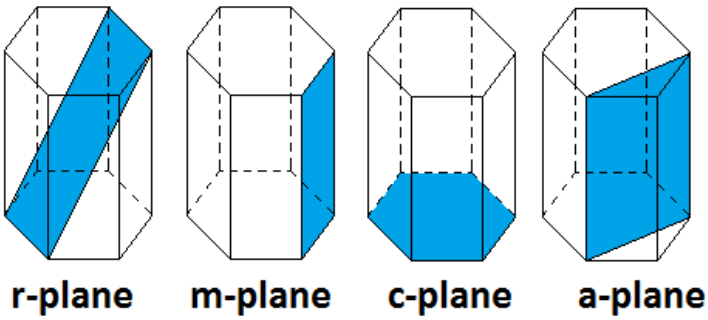

Figure 2.5 Schematic of some commonly planes in an III-nitride wurtzite structure

2.2.2 Epitaxial growth of III-nitrides

Metal Organic Chemical Vapour Deposition (MOCVD)[49-51] and Molecular Beam Epitaxy (MBE)[52,53] are two major kinds of growth techniques used for the growth of III-nitride semiconductors. MOCVD shows some advantages compared with MBE in terms of mass production, and thus is more attractive for the semiconductor industry.[54]

For the MOCVD growth of III-nitride semiconductors, metalorganic (MO) sources, such as trimethylgallium (TMG), trimethylaluminium (TMA), Trimethylindium (TMI) and ammonia (NH_3), are typically used as the precursors to supply group III and V elements, respectively. MOCVD has been widely used to grow III-nitride semiconductors in industry mass production.

In terms of configurations, MOCVD systems can be divided into two major types in terms of gas flowing, namely, vertical type [50] and horizontal type.[55] In a horizontal MOCVD reactor, MO sources flow laterally into the reactor and a substrate is placed

in a small angle of inclination to a horizontal direction in order to deposit a uniform film on the substrate. In a vertical reactor which will be discussed in section 3.1 in detail, MO sources are introduced vertically into the reactor and then a substrate. In this work, all growth activities have been carried out by a vertical type MOCVD.

Ideally, epitaxial growth requires a substrate which has the same crystal structure, lattice constants and thermal expansion coefficient as an epitaxial layer in order to achieve high crystal quality. However, as discussed in section 1.4, free standing GaN substrates are not available cost-effectively. Consequently, GaN is commonly grown on a foreign substrate, which is called as hetero-epitaxy. In this work, sapphire is used as a substrate for GaN growth.

There exist a number of different orientated sapphire substrates, such as c-plane (0001) sapphire which is widely used for growth of c-plane polar GaN; (10-10) sapphire, denoted as m-plane sapphire, is typically used for growth of (11-22) semi-polar GaN; (1-102) sapphire, labeled as r-plane sapphire, is typically for the growth of (11-20) non-polar GaN. The in-plane lattice-mismatch between sapphire and GaN can be calculated based on their individual in-plane lattice constants. However, it is worthwhile to point out that the GaN basal plane need to rotate by 30^{o} around its c-axis in order to match sapphire energetically favorably.[56] Consequently, the lattice mismatch between (0001) sapphire and c-plane GaN in basal plane is 16%.

2.2.3 Defects in III-nitride semiconductors

As stated above, GaN is typically obtained through hetero-epitaxial growth on a foreign substrate. As a result, there exist a large number of defects in GaN. Typically, there are three main types of defects in III-nitride semiconductors: point defects, dislocations and stacking faults.

A point defect is a kind of zero-dimensional defects. When an atom is missing or located in a wrong site, a point defect is generated. To be specific, a point defect can be due to an atomic vacancy, a self-interstitial atom, interstitial impurity or substitution impurity, etc. A vacancy is generated where an atom is missing from the

lattice site; a self-interstitial atom is an extra atom located in a non-lattice site; an interstitial impurity atom is a foreign atom staying in a non-lattice site; and a substitution impurity atom is a foreign atom substituting a bulk atom in a lattice site. The most commonly point defect observed in a GaN epitaxial layer is due to nitrogen vacancies.

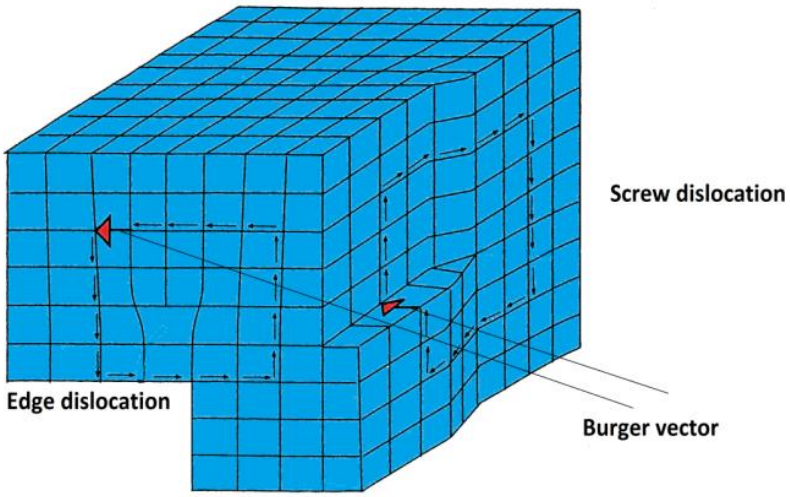

Figure 2.6 Schematic of edge and screw dislocations

A dislocation is a kind of one-dimensional defects. Basically, there are three major types of dislocations, namely, edge dislocations, screw dislocations, and mixed dislocations. As schematically illustrated in Figure 2.6, an edge dislocation is produced when a half plane is missing or an extra half plane is inserted into a lattice. A screw dislocation is produced when atoms slip across one plane from the crystal by a lattice vector forming a boundary plane. The Burger vector **b** represents the magnitude and the direction of the lattice distortion resulting from a dislocation in a crystal lattice. As shown in Figure 2.6, the Burger vector for an edge dislocation is perpendicular to the dislocation line, while the Burger vector for a screw dislocation is parallel to the dislocation. Generally, a dislocation normally acts as a non-radiative recombination centre in III-nitride semiconductors.

A stacking fault (SF) is a kind of planar defects, which changes the stacking sequence of the atomic planes in a crystal. In hexagonal III-nitrides, the most dominant type of SFs is the basal plane SF (BSF), which is formed where an ABC cubic structure exists locally within a usual …ABABAB… hexagonal staking sequence.

Therefore, it actually introduces a quantum-well like cubic GaN region within a wurtzite structure. In c-plane GaN, BSFs are usually generated at the interface between GaN and sapphire, and lie along a basal plane which is perpendicular to the growth direction. Consequently, the BSFs do not propagate to any overlying layer, and thus do not affect material property and device performance. However, for semi-polar or non-polar GaN, the BSFs are inclined to the growth direction. As a result, they can extend to the surface of the whole epi-layer. Generally speaking, semi-polar or non-polar GaN directly grown on sapphire without any extra process exhibit high density of BSFs, and BSFs related emissions can be observed by measuring low temperature photoluminescence spectra. It has also been reported that BSFs also lead to broadening in the line-width of XRD rocking curves.[57,58]

Figure 2.7 is a typical TEM image of c-plane GaN grown on sapphire, where a number of black lines indicate screw/edge dislocations and BSFs can be observed at the interface between GaN and sapphire.

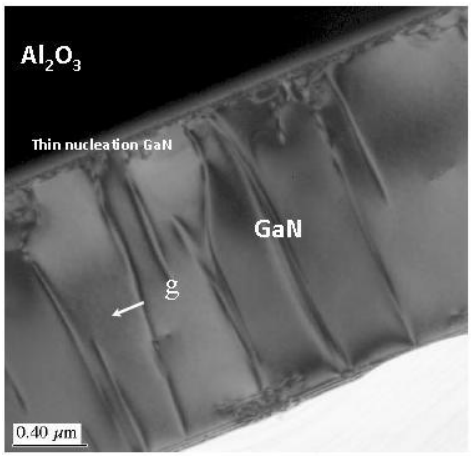

Figure 2.7 Cross-sectional two-beam bright-field TEM images of typical GaN grown on c-plane sapphire[59]

2.2.4 Material properties of III-nitrides

Electron Mobility

Carrier mobility is used to describe the ease with which electrons or holes can flow through a crystal such as a semiconductor. Under an electric field across a semiconductor, the relationship of drift velocity, mobility and electric field can be

expressed by equation 2.2.

$$v = \mu E \qquad (2.2)$$

where v is the drift velocity, μ is the mobility and E is the electric field used.

Electron mobility is an important parameter to evaluate crystalline quality, as it is generally very sensitive to defects due to scattering effects.

Carrier (electrons or holes) mobility can be measured through an equation given.

$$\rho = 1/q(n\mu_n + p\mu_p) \qquad (2.3)$$

Where ρ is the resistivity of the semiconductor; n is the density of free electrons measured; p is the density of free holes measured; μ_n and μ_p are the mobility of electrons and holes, respectively.

Normally, one type of majority free carriers (either electrons or holes) dominate a semiconductor, meaning that the density of the majority carriers is a few orders magnitude higher than that of the minority carrier. For example, for a n-type semiconductor, equation 2.3 can be simplified as given below.

$$\rho = 1/(q\, n\mu_n) \qquad (2.4)$$

Equation 2.5 can be obtained from equation 2.4.

$$R_s = 1/(qn_s\mu) \qquad (2.5)$$

Where,

$$R_s = \frac{\rho}{t} \qquad (2.6)$$

And,

$$n_s = nt \qquad (2.7)$$

R_s is the sheet resistance, n_s is the sheet carrier density and t is thickness of the semiconductor.

$$\mu = 1/(qn_sR_s) \qquad (2.8)$$

Therefore, carrier mobility can be obtained by means of measuring the sheet carrier density and the sheet resistance of a semiconductor. To obtain sheet carrier density and sheet resistance, the Van der Pauw method is the commonly used technique. Currently, the typical electron mobility of standard c-plane undoped GaN

grown on a sapphire substrate is ~900 cm^2/Vs at room temperature.

Doping

Doping is the process of adding different elements to intrinsic semiconductors to alter their properties, mainly electrical properties. In III-V semiconductors, a group III atom provides three valance electrons while a group V atom gives five valance electrons. If a group IV atom replaces a group III atom in an III-V semiconductor, the group IV atom acts as a donor supplying an extra electron, leading to n-type doping, where the major carriers are electrons. Likewise, when a group II atom replaces a group III atom, the system misses one valance electron, generating p-type doping, where the major carriers are holes.

To be more specific for III-nitride semiconductors, Si is a commonly used dopant for the growth of n-type GaN and Mg is typically used for p-type doping. Nominally undoped GaN shows characteristics of n-type, showing a high density of residual carriers which is mainly caused by point defects as a result of nitrogen vacancy. Si-doped GaN exhibits a wide range of free electron densities, typically from 10^{17} to $10^{19}/cm^2$. For Mg-doped GaN, it is a little complicated. As-grown Mg-doped GaN grown by MOCVD is typically n-type or semi-insulating, because Mg-H complexes are formed during the growth of Mg-doped GaN under hydrogen ambient. P-type GaN can be obtained only after breaking the Mg-H complexes and removing hydrogen atoms from Mg-doped GaN. This can be achieved using a low energy electron radiation or through a high temperature annealing process under nitrogen ambient. This process is called as p-type activation.

Lattice constant and band gap

Table 2-1 shows the lattice constants and the band gaps of III-nitride semiconductors. The bandgap of AlN, GaN, InN and their ternary alloys can span from 6.2 to 0.7 eV, allowing III-nitrides to be fabricated for emitters ranging from the DUV to infrared. However, for InGaN/GaN MQWs based LEDs with high indium composition, one of the great challenges is due to significantly enhanced QCSE as a

result of the large lattice mismatch between InN and GaN.

Material	In-plane lattice constant (Å)	Out-of plane lattice constant (Å)	Band gap (eV)
AlN	3.112	4.982	6.2
GaN	3.189	5.185	3.4
InN	3.533	5.693	~0.7

Table 2-1 Lattice constants and band gaps of III-nitride semiconductors

Chemical properties

Generally speaking, III-nitride semiconductors exhibit excellent chemical stability, thus allowing III-nitride based devices to work in harsh environment. This feature broadens the application areas of III-nitrides-based devices.

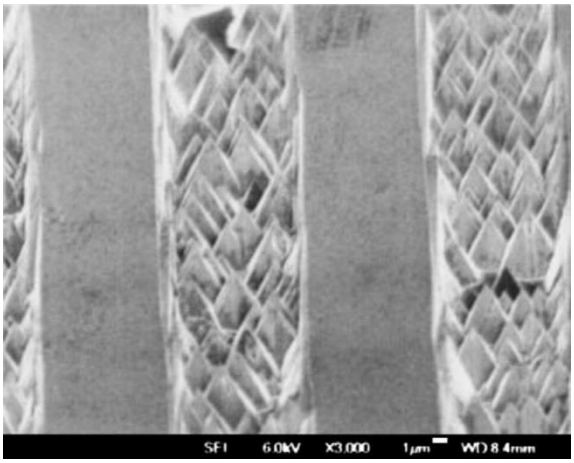

Figure 2.8 Surface morphology of the N-polar and Ga-polar area after KOH etching [61]

However, under some circumstances, wet etching needs to be employed on III-nitrides. Various etchants have been studied on GaN etching, including nitric acid (HNO_3), phosphoric acid (H_3PO_4) and potassium hydroxide (KOH). It has been found that etching rates on III-nitride semiconductors strongly depend on material quality and polarity, in addition to etching conditions. For example, Palacios et al. reported that N-polar GaN can be easily etched by aqueous KOH at a temperature between 26°C to 80 °C while no etching happens to Ga-polar GaN.[60] After the KOH etching, the N-polar surface is covered by hexagonal hillocks with facets of (10-1-1) planes

while the surface morphology of the Ga-polar GaN remains unchanged.[61-63] Similar results occur to GaN etching using hot H_3PO_4. The N-polar GaN can be etched away quickly, while for the Ga-polar surface there are only pits formed associated with defects and the surface morphology of the defect-free GaN area remains unchanged.[64-68] Figure 2.8 shows the different surface morphologies of the N-polar and the Ga-polar areas after KOH etching at 90 °C for 45mins. Furthermore, the etching rates of GaN and AlN using various etchants are shown in Table 2-2.

Etchant	GaN etch rate (nm/min)	AlN etch rate (nm/min)
Nitric acid	0 (85 °C)	0 (85 °C)
Phosphoric acid	0 (82 °C)	0 (82 °C)
Hydrofluoric acid	0	0
Sulfuric acid	0	0
Sodium hydroxide	0	50 (75 °C)
Potassium hydroxide	0	2265
$HCl/H_2O_2/HNO_3$	0	0

Table 2-2 GaN and AlN etching rates using different chemical solutions at room temperature unless noted[69]

2.3 Semi-polar (11-22) GaN

2.3.1 Crystal structures and advantages

C-plane (0001) GaN has been widely used by the semiconductor industry. Currently, c-plane GaN growth technologies on sapphire have approached their limitations in terms of performance and crystal quality. Semi-polar and non-polar GaN have become increasingly interesting due to their potential advantages over c-plane GaN. Non-polar GaN, such as the (11-20) orientation, is grown along a direction which is perpendicular to c-direction; and semi-polar GaN is tilted with respect to the c-direction. There are a number of different types of oriented

semi-polar GaN, including (11-22), (10-13) and (20-21),[70-72] among which (11-22) and (20-21) are the most important semi-polar GaN. In this thesis, the project is focused on a study of semi-polar (11-22) GaN. The schematic of (11-22) crystal plane is shown in Figure 2.9.

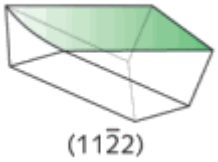

Figure 2.9 Schematic of (11-22) crystal plane

As summarized in section 1.5, semi-polar GaN grown along the [11-22] orientation is favorable for achieving high efficiency emitters with longer emission wavelengths. As shown in Figure 2.10, the piezoelectric polarization along the (11-22) orientation is much weaker than that for c-plane GaN, leading to a significant reduction in QCSE for semi-polar (11-22) InGaN/GaN QW structures.[73, 74] Furthermore, (11-22) GaN exhibits a significantly enhanced indium incorporation rate compared with non-polar or c-plane polar GaN.[75,76] The indium incorporation rate on the (11-22) GaN surface is also higher that on the (20-21) semi-polar surface.

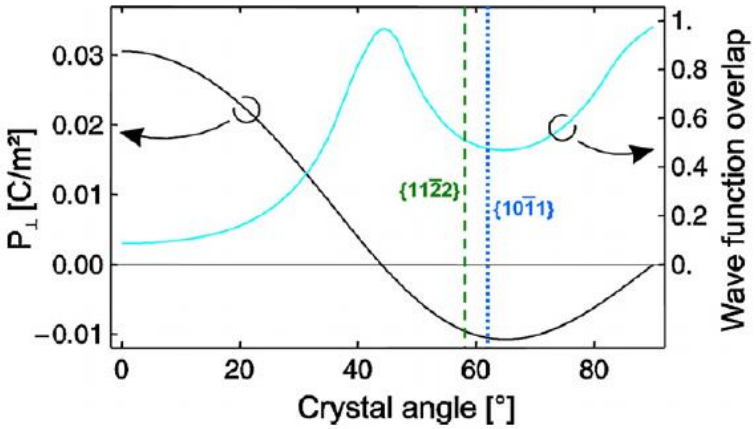

Figure 2.10 Piezoelectric polarization and wave function overlap as a function of crystal angle with respect to c-plane orientation.[77]

As a result of a significant reduction in piezoelectric fields induced polarization, the recombination life time of excitons in InGaN/GaN QW structures grown on the (11-22) GaN surface is expected to be significantly reduced,[78] which is very good for

the fabrication of visible emitters for ultrafast Li-Fi system. In addition, semi-polar (11-22) GaN-based LEDs intrinsically exhibit polarized emission,[3] which plays an important role in back-lighting. Current backlighting devices require polarizers, leading to absorption of extra 30% energy.

To date, the growth of semi-polar GaN along the (10-13) or (11-22) orientation on planner sapphire substrates has been reported. However, (10-13) GaN suffers from intrinsic surface problems, namely, the formation of micro-twining structures, while a smooth surface can be obtained for (11-22) GaN.[79-83]

2.3.2 Current status

The earliest attempt at the growth of semi- or non- polar GaN was reported by Sasaki, *et al.* in 1986,[84] who obtained semi- or non- polar GaN unintentionally. The first deliberate attempt at non-polar GaN growth was reported in 2000,[85] where the substrate was $LiAlO_2$ and the deposition technique was MBE instead of MOVPE, because the MOVPE growth of GaN generally requires a high temperature which leads to severe diffusion of Li and Al atoms into the overlying GaN. The classic two-step growth approach can be used for the growth of semi- or non- polar GaN on sapphire, but the crystal quality is far behind that of c-plane GaN. Our group has developed a high temperature AlN buffer approach,[86] leading to some improvement in crystal quality, but it is still far from requirements.

Conventional epitaxial lateral overgrowth (ELOG) and the techniques evolved from the ELOG, which were developed originally for c-plane GaN, have been used to improve the crystal quality of the semi-/non-polar GaN grown on sapphire substrates.[87-94] Some good results have been achieved. However, it is still not good enough. The ELOG techniques basically use a selective area overgrowth approach, thus requiring an ex-situ fabrication process.

Recently, our group demonstrated an overgrowth technique, with both improved crystal quality and good uniformity, by using a nano-rod template formed with self-organized Ni masks.[37,95] Most recently, our group has developed a new

overgrowth technique by using a regularly arrayed micro-rod template. Further improved crystal quality with a massive reduction in BSF density has been achieved.[96]

The research of semi-polar GaN grown on Si substrates has attracted great attention. Dadgar *et al* have demonstrated semi-polar GaN grown on a high index Si (11h) substrate.[97] Currently, most semi-polar GaN grown on Si is grown on a stripy Si substrate with (1-11) and (-11-1) facets being exposed, which are obtained by using an anisotropic wet etching approach.[98,99] However, at high growth temperature, the reaction between Ga and Si (-11-1) takes place, stopping the growth process. This is so called "Ga melting back".[100] In order to prevent the Ga melting back issue, our group has demonstrated a semi-polar (11-22) GaN grown on a patterned (113) Si substrate with periodical inverted-pyramids.[101] These inverted-pyramids have four facing-up Si (111) facets. Three of them can be selectively covered with SiO_2, leaving the fourth (111) facet to remain uncovered for further growth of semi-polar (11-22) GaN.

Regarding semi-polar GaN based devices, the first room temperature continuous-wave semi-polar (20-21) InGaN based laser with an emission wavelength at 520nm was achieved by Y. Yoshizumi et al. in 2009, and this was grown on extremely expensive free standing semi-polar GaN substrates with a limited size. The threshold current and the current density of the laser are 95mA and 7.9kA/cm^2, respectively.[102] Recently, our group has reported semi-polar (11-22) InGaN/GaN based LEDs on sapphire, with emission wavelengths ranging from green to amber.[3]

2.3.3 Substrate issue

Semi-polar (11-22) GaN with very low defect density can be grown on free-standing semi-polar (11-22) bulk GaN substrate. However, the semi-polar free-standing GaN substrate is typically prepared by cleaving thick c-plane bulk GaN grown by HVPE along the (11-22) orientation, which results in not only a size limitation but also an extremely high cost. Apart from the HVPE growth technique, semi-polar bulk GaN substrates can be grown by Ammonothermal method.[103]

It would be very difficult to grow semi-polar GaN on a planar Si substrate. So far, all the reported semi-polar (11-22) GaN-on-Si is obtained by utilizing a patterned Si substrate, fabricated by means of using an isotropic chemical wet etching approach.[98,104,105]

Sapphire substrates are also available for semi-polar GaN growth. Semi-polar (11-22) and (10-13) GaN can be grown on m-plane (10-10) sapphire substrates which are commercially available. Additionally, m-plane sapphire substrates with a large size beyond 2 inch are also available.

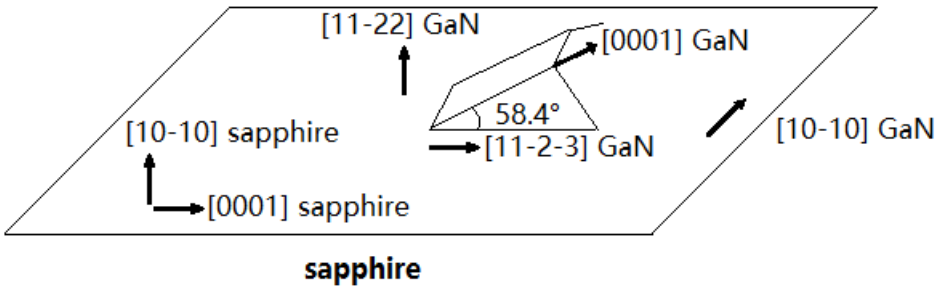

Figure 2.11 Epitaxial relationship between semi-polar (11-22) GaN and a *m-plane* sapphire

Figure 2.11 shows the epitaxial crystallographic orientation between semi-polar (11-22) GaN and m-plane sapphire. To be specific, the in-plane epitaxial relationships between (11-22) GaN grown on m-plane sapphire are $[11\text{-}2\text{-}3]_{GaN} // [0001]_{sapphire}$ and $[1\text{-}100]_{GaN} // [1\text{-}210]_{sapphire}$, respectively.

In semi-polar (11-22) GaN, the $[0001]_{GaN}$ is 58.4° inclined to the m-plane sapphire surface, with a projection on the surface along [11-2-3] orientation. Due to the large lattice mismatch between the epi-layer and the substrate, a large number of defects are generated. Unlike c-plane GaN, BSFs in (11-22) GaN formed at the interface between GaN and sapphire can extend to the surface of epilayer. As a result, the crystal quality of current semi-polar GaN on m-plane sapphire is far from requirements for the growth of devices. Typically, the dislocation density and the BSF density are on the order of $10^{11}/cm^2$ and $10^6/cm$, respectively.[87,106-111] Therefore, it remains a great challenge to achieve high quality semi-polar GaN

2.3.4 Epitaxial overgrowth

As mentioned above the ELOG-related approaches are based on selective area overgrowth on a periodically patterned template, which requires an ex-situ fabrication process normally with a dielectric mask. The regions without any dielectric mask are defined as window regions while the areas covered with the dielectric masks are called wing regions. During an overgrowth process, GaN growth starts from the window regions and then extends laterally to coalesce in the wing regions. A flat epitaxial film is finally obtained. The crystal quality of the overgrown layer can be largely enhanced since the dielectric masks can block defect penetration. However, for any conventional ELOG approach, a template is patterned normally with stripes whose width is typically on the order of tens of micrometers. An atomically flat surface cannot be obtained until the overgrown layer has reached 10–20 μm thick. In addition, defects in the window regions still can propagate to the upper layer, thus leading to a non-uniformity issue on the crystal quality of overgrown GaN. For semi-polar GaN, there are a number of other issues, such as anisotropic growth rate, penetration of basal stacking faults along an inclined angle with respect to the vertical direction. Therefore, the ELOG employed for the semi-polar GaN needs to be further developed in order to achieve high quality and good uniformity semi-polar GaN on sapphire.

2.4 Etching of GaN

2.4.1 Dry etching

Dry etching is an approach to remove material by means of using ion bombardment. Dry etching can be performed either with physical processes, chemical processes or both them. The chemical processes refer to the removal of material by a chemical reaction between etchant and material surface. The physical

process takes advantages of high energy ions to knock atoms out of a material. Compared with a wet etching process, dry etching has a high etching rate, and exhibit uniformity in etching rate and a flexibility in controlling an etching process.[112]

Inductively Coupled Plasma (ICP) etching techniques have been widely used in etching GaN.[113] The ICP etching involves a combination of physical and chemical processes. In the physical process, the ions accumulate a high energy from the applied electric fields. In the meantime, a plasma is created to obtain an active etchant. For GaN etching using ICP in our case, argon ions and chlorine plasma are used as the physical and chemical etchants, respectively.[114]

2.4.2 Wet etching

Wet etching is used widely in the field of semiconductors. In an electronic industry, the most commonly used wet etching is using HF acid to remove a thin oxide layer on Si wafers. Basically, III-nitrides with Ga or Al polarity are intrinsically chemically inert. However, defects in III-nitrides can be attacked. Consequently, wet etching can also be used to facilitate defect evaluation as a simple method. In contrast, III-nitrides with nitrogen polarity can be etched by a chemical solution, such as potassium hydroxide.[115,116]

Generally, speaking, wet etching has advantages of a high selectivity, simple equipment requirement and producing negligible crystal damage. However, the key issue is to find a right solution and to optimize etching conditions. III-nitrides are very stable in any chemical solution. Consequently, photo chemical etching is an effective method. Two processes are involved in photon-assisted chemical etching of III-nitrides, namely, oxidation of the material surface and then the dissolution of the resulting oxides. The oxidation of the material surface requires holes which can be supplied by exiting electrons from a valence band to a conduction band. For example, an ultraviolet light source is typically employed for photon-assisted chemical etching on GaN in a KOH solution. The mechanism of the photo-assisted etching will be discussed in Chapter 5 of this thesis.

Chapter 3 Experimental techniques

3.1 Metal Organic Chemical Vapour Deposition (MOCVD)

In the last two decades, MOCVD has been the major method for III-nitride growth. In this chapter, the main structure of a MOCVD system, including main carrier gas lines, metal-organic (MO) source bubblers and a reactor chamber, will be briefly introduced. Subsequently, MOCVD growth mechanisms will also be discussed. Figure 3.1 shows an image of the MOCVD system which is used to grow samples for the present study.

Figure 3.1 MOCVD

The main structure and key components of MOCVD are described as follows:

Carrier gas lines

Figure 3.2 shows a schematic illustration of a configuration of gas lines in a Thomas Swan MOCVD system, where the solid lines represent different kinds of gas lines and the different colors indicate different kinds of carrier gas (either hydrogen or nitrogen). Hydrogen (H_2) and nitrogen (N_2) lines are labeled as the green and the blue lines, respectively. The yellow lines stand for the two main carries gas lines

which are carrying metal-organic (MO) source and ammonia (NH_3) into the reactor as the precursors of group III and V elements, respectively.

The precursors of group III and V elements are introduced into the reactor by the carrier gases through a manifold which is used to allows them to enter either the reactor chamber or the vent line.

Mass flow controllers (MFC) are widely used in a MOCVD system, and allow us to accurately control the flow rates of any gas passing through. Consequently, the growth rate can be accurately controlled.

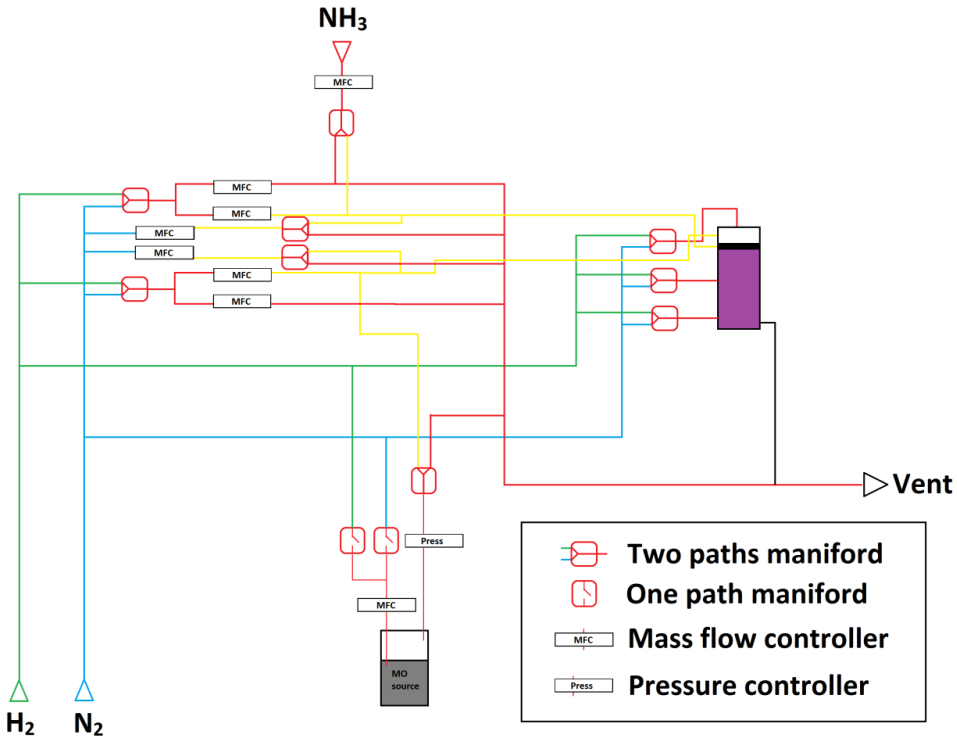

Figure 3.2 Schematics of the gas lines in MOCVD

MO source bubbler

Three major MO sources as the precursors of group III elements are widely used for the MOCVD growth of III-nitrides, namely Trimethylgallium (TMGa), Trimethylalluminium (TMAl) and Trimethylindium (TMIn). At room temperature, TMGa and TMAl are in a liquid state, while TMIn can be either in a liquid or solid state.

Figure 3.3 schematically demonstrates how a MO bubbler works. An input tube is inserted into the bottom of a bubbler, and an output tube locates on the top part

of the bubbler, which needs to be above the surface of a liquid MO. During growth, a carrier gas is introduced to a MO bubbler through an input tube, and then takes the MO out of the bubbler through an output tube. In order to eliminate any condensation issue, a thermal tape is used in order to keep the output tube warm.

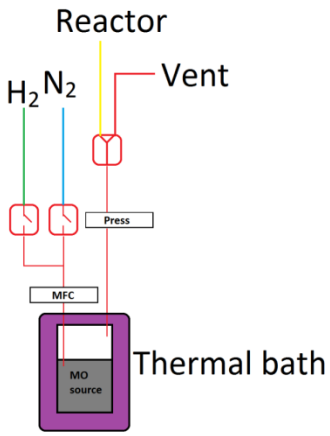

Figure 3.3 Schematic of a MO source bubbler

The mole flow rate of a MO source is determined by the bubbler pressure, the bubbler temperature and the MFC flow rate in a sccm (standard cubic centimeter per minute) unit. The molar flow rate of a MO source can be calculated based the equations provided below:

$$\mathrm{P_{partial}} = 10^{(\mathrm{a}-\frac{\mathrm{b}}{\mathrm{T}})} \ \mathrm{torr} \qquad (3.1)$$

$$f_{MO}(mole/min) = \frac{P_{partial(MO)}}{p_{bubbler}} \times \frac{1}{22.4} \times f_{MO}(litre/min) \qquad (3.2)$$

where $\mathrm{P_{partial}}$ is the partial pressure of a MO source at a given temperature; $\mathrm{P_{bubbler}}$ is the bubbler pressure controlled by a pressure controller; T is the bubbler temperature in a water bath; and $f_{MO}(litre/min)$ is the flow rate in a sccm unit, which is controlled by a MFC, $f_{MO}(mole/min)$ is the flow rate in a molar per minute.

Equation 3.1 indicates that the partial pressure of a MO source sensitively depends on the temperature of a bubbler which is used to store a MO and the partial pressure of the bubbler. Table 3-1 shows the “a” and “b” values used in Equation 3.1 for all the MO sources used for the growth of III-nitrides.

Compound	a	b
TMAl	10.48	2780
TMGa	8.50	1825
TMIn	9.74	2830
Cp_2Mg	10.56	3556

Table 3-1 Vapor partial pressure constants of common MO source

NH_3

The NH_3 as the group V element precursor used in our MOCVD is so-called 'white ammonia' with a purity of 99.99999%. It is stored in a standard gas cylinder and a purifier is normally required before the NH_3 is introduced into the gas line of the MOCVD as schematically shown in Figure 3.4.

The molar flow rate of NH_3 can be simply calculated by using the equation below.

$$f(mole/min) = \frac{f(litre/min)}{V_m} \quad (3.6)$$

Where V_m is the molar volume which is 22.4L/mol at 273K and under a standard atmospheric pressure.

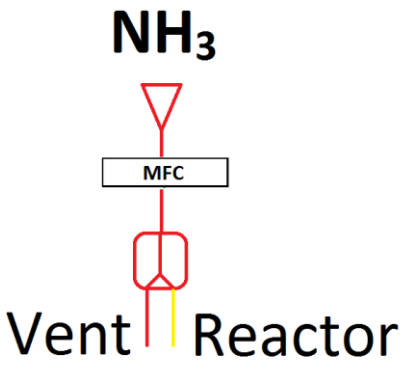

Figure 3.4 Schematics of a NH_3 gas line

Carrier gas

In a MOCVD system, hydrogen is generally used as a carrier gas due to its high purity. The high purity of the hydrogen can be achieved by using a hydrogen purifier. As shown in Figure 3.5, the key component for a hydrogen purifier is a palladium

membrane, allowing only hydrogen molecules to pass through at a high temperature.

However, for InGaN growth, it has been found that hydrogen as a carrier gas can significantly reduce indium to be incorporated into GaN even at a low temperature. In the meantime, it has been found that N_2 as a carrier gas facilitates to incorporate indium into GaN at a similar temperature. Consequently, N_2 as a carrier gas has been widely used as a carrier gas for InGaN growth.

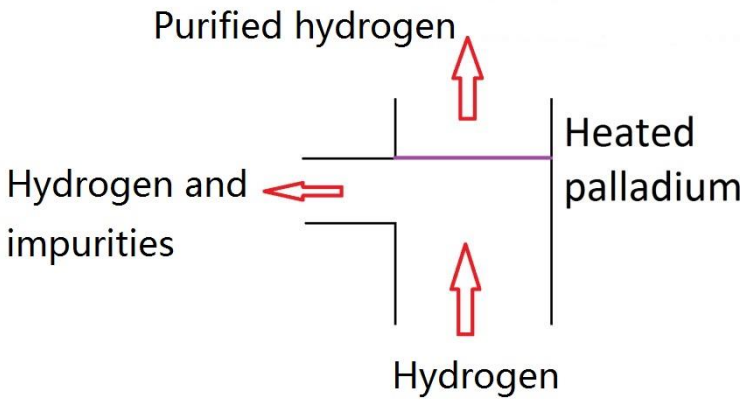

Figure 3.5 Schematic of the hydrogen purifier

Close coupled showerhead (CCS) reactor

The MOCVD system which is used for the present study was manufactured by Thomas Swan (Scientific Instrument) Ltd, which is now part of Aixtron Ltd in Germany, where the key component is a stain-steel made showerhead located above a susceptor. Figure 3.6 shows a schematic illustration of a typical CCS reactor, having many tiny pipes uniformly distributed across the showerhead. These pipes are divided into two groups: one is used to supply the precursors for Group III elements, and another to supply the precursors for group V element. With such a design, the precursors for group III and V elements mix just above a substrate in order to minimize any pre-reaction. The excellent uniformity in growth can be obtained by the rotation of the susceptor. A water cooling system is used to cool the showerhead; and another separate cooling system is used to maintain the temperature of the whole reactor chamber constantly at ~50 ^{o}C. GaN growth is performed at a high temperature, typically above 1000 °C. Furthermore, in order to minimize any

chemical reaction between the susceptor and NH_3, the susceptor is made of graphite coated with SiC. A heater is located under the susceptor. A thermal couple is used, and just put below the susceptor. An in-situ monitoring system based on three LDs (405 nm, 635 nm and 980 nm LDs) is used to monitor the reflectivity of the wafer, surface temperature and wafer bowing of different layers during growth.

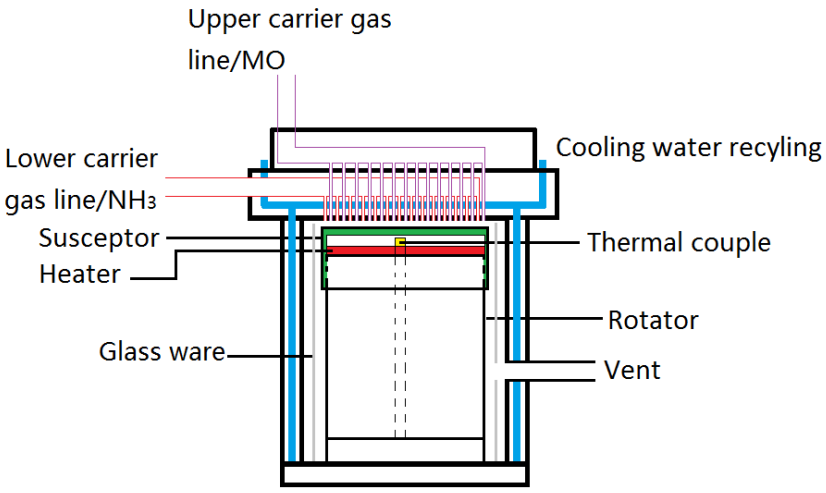

Figure 3.6 Schematics of the CCS reactor

Standard GaN growth using TMGa as a group III element precursor in MOCVD can be expressed by the following chemical equation 3.7.

$$(CH_3)_3Ga + NH_3 = GaN + 3(CH_4) \quad (3.7)$$

A number of processes are involved. At a high temperature, TMGa and NH_3 are decomposed in order to supply Ga and N ions, and a chemical reaction then happens between them.

3.2 X-ray diffraction (XRD)

XRD is a rapid and non-destructive material characterization technique. XRD measurements have been widely used to investigate the crystal quality, layer thickness, alloy composition and strain status of epi-layers and QW structures in the field of semiconductor materials and devices.

The principle of XRD can be interpreted based on Bragg's law, as expressed by Equation 3.8:

$$2\mathrm{d}\sin\theta = n\lambda \qquad (3.8)$$

where λ is the wavelength of x-ray, θ is the incident angle with respect to the planes, and d represents the lattice constant. Constructive interference will occur and the diffracted intensity will reach the maximum when the path difference, 2dsinθ, is equal to an integer number of wavelengths, nλ.

X-ray diffractometer

An x-ray diffractometer typically consists of an x-ray generator, a sample stage, a goniometer and a detector, as shown in Figure 3.7 (b). X-ray is generated by bombarding a metal by high energy electrons. The x-ray beam used for this work is generated using copper (Cu) as a target material, corresponding to a wavelength of 1.5418Å. The generated x-ray beam is then introduced into an optics unit which consists of a Goebel mirror, a monochromator and divergence slits. The Goebel mirror, the monochromator and the divergence slits are used to collimate and limit the divergence of the x-ray beams. The goniometer is used for aligning a sample with a detector. The detector can be either an open type or further confined by a secondary optics unit. The secondary optics unit contains similar components to the incident x-ray optics unit.

Figure 3.7 (b) illustrates a relationship between an incident angle and a diffraction angle used for XRD measurements in a typical Omega-2θ mode. Omega (ω) is defined as an angle between an incident x-ray beam and the sample stage used, while 2theta (2θ) is an angle of the detector used (a diffracted beam) with respect to the incident beam direction.

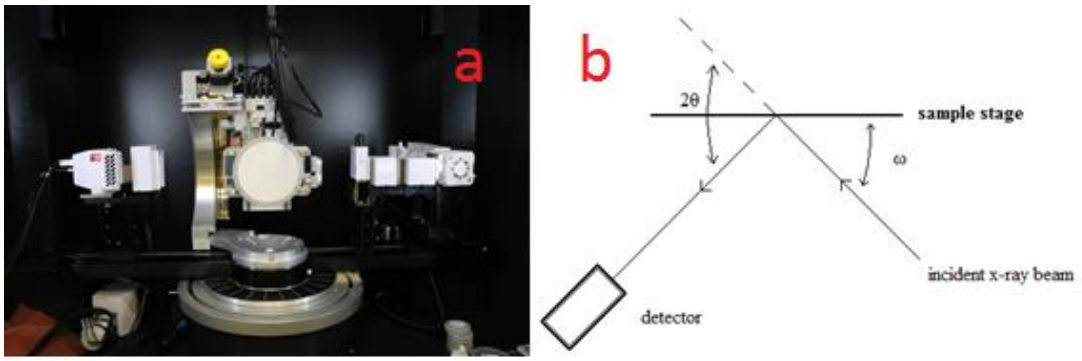

Figure 3.7 (a) The image of Bruker D8 x-ray diffractometer; (b) Schematic illustration of the angles (omega and 2theta) used in a diffractometer.

The movement of the sample stage along x, y and z axis can be precisely controlled as shown in Figure 3.8. An in-plane rotation angle (rotate around z axis) or azimuth angle, phi, and an inclination angle (rotate around x axis), chi, are finely controlled by the goniometer.

Figure 3.8 Illustration of the movement of the sample stage and rotating angles

In addition to the omega/2theta scanning mode for XRD measurements mentioned above, XRD measurements can be performed in other modes for different purpose, such as XRD rocking curve mode, reciprocal space mapping (RSM), etc. XRD rocking curve measurements are normally performed as a function of ω while keep 2θ fixed. Through measuring the full width at half maximum (FWHM) of a XRD rocking curve, the crystal quality of a semiconductor can be evaluated. As an example, Figure 3.9 shows a typical XRD rocking curve of a GaN layer grown on (0001) sapphire, indicating that the FWHM of the XRD rocking curve is around 250 arcsec.

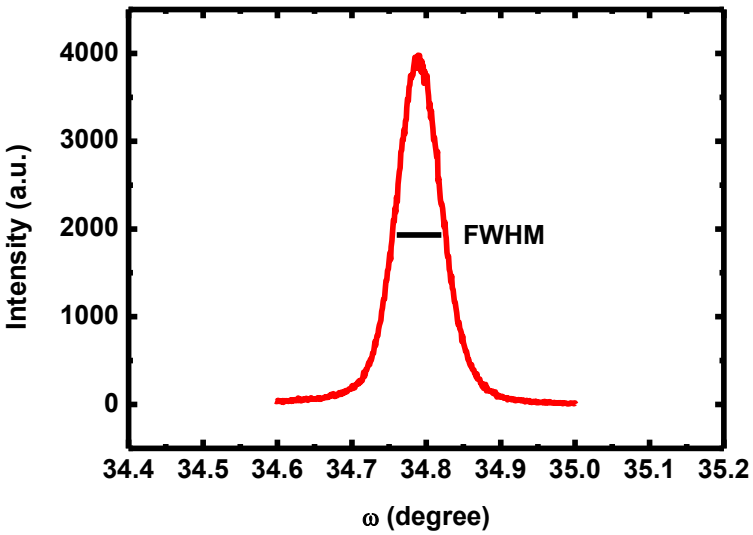

Figure 3.9: a typical XRD rocking curve of a typical GaN layer grown on (0001) sapphire

XRD measurements conducted in the Omega-2theta mode can be used to characterize alloy composition, QW thickness, strain, etc.

Detailed information on strain relaxation can be obtained through measuring RSM. The RSM can be obtained when omega/2theta scans are repeated for a sequence of omega offset values.

3.3 Scanning electron microscopy (SEM)

SEM measurements can be used to characterize surface morphology of a semiconductor epi-wafer. When electrons are incident on the surface of a layer, the electrons will experience reflection or back-scattering, forming so-called second electrons. A SEM image is formed through such second electrons, and thus an image formed in such a way displays the topography of the surface of the layer.

Figure 3.10 schematically illustrates our SEM system used in our laboratory, which consists of three main parts: an electron column, a scanning system and a vacuum system. In the electron column, an electron beam produced by an electron gun, which typically has an energy ranging from 0.24 to 40 keV, is focused by a few condenser lenses to a spot with a diameter of 0.4 to 5 nm. It then passes through

pairs of scanning coils and then deflected by a final lens along x and y directions. Finally, the electron beam can be used to scan a sample surface.

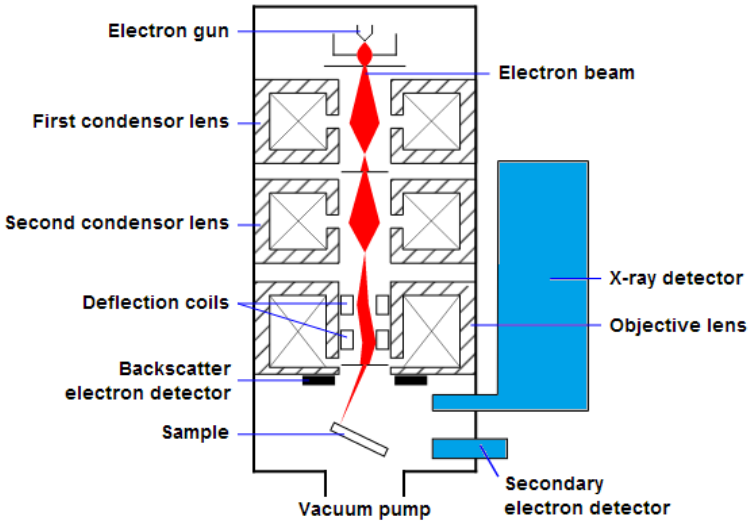

Figure 3.10 Schematic diagram of a SEM system

3.4 Atomic force microscopy (AFM)

AFM can be used to characterize the surface morphology of a semiconductor epi-wafer on a nano-meter scale. One of the core components in an AFM system is a cantilever with a sharp tip (probe) at its end that is used to scan a specimen surface. Figure 3.12 shows a schematic illustration of a standard AFM system. By scanning the tip across a sample surface, the deflection of the cantilever which contains the local information about the surface morphology, will be recorded by a detector and then converted into an electrical signal. The intensity of this signal represents the surface morphology.

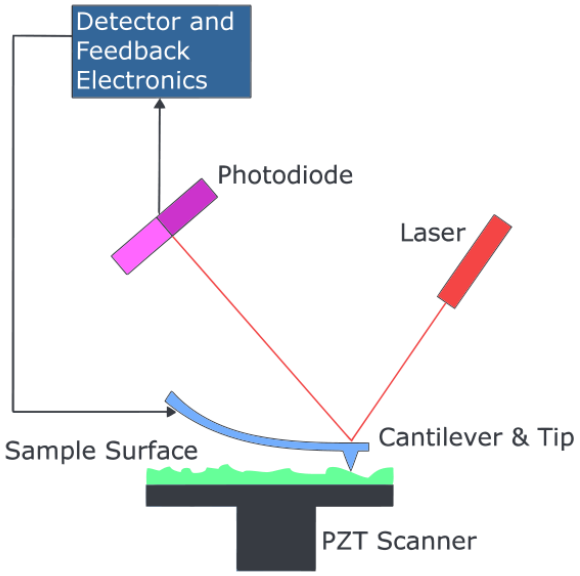

Figure 3.11 Schematic of an AFM system

AFM measurements can be conducted typically in three modes: contact mode, non-contact mode and tapping mode. In a contact mode, the tip keeps touching a sample surface when it scans across the sample. The signal is obtained either directly from the deflection of the cantilever, or from the feedback signal which is required to keep the cantilever at a constant position.

In a non-contact mode, the tip does not contact a sample surface and the cantilever is oscillating at a resonance frequency. The amplitude of the oscillation is from 1 to 10 nm above the sample surface. In this distance range, the van der Waal force dominates and tends to reduce the resonance frequency of the cantilever. A non-contact mode does not suffer from tip or sample degradation effects that are sometimes observed in a contact mode after taking numerous scans. This makes a non-contact mode preferable, in particular in a contact mode for measuring soft samples.

A tapping mode is the one used in our AFM measurements. In this mode, the cantilever is oscillating up and down above a sample surface at or near its resonance frequency with an amplitude typically from several nm to 200 nm. Both the frequency and the amplitude used remain constant in the case that there is no any interaction between the cantilever and the sample surface. When the tip approaches the sample surface, due to the van der Waals forces, the dipole-dipole interactions

and the electrostatic forces, etc, the amplitude of the cantilever oscillation will be changed, which is then recorded by an electronic servo. By this way, the servo adjusts the height to maintain the oscillation amplitude of the cantilever. An AFM image formed in such a tapping mode is therefore produced.

3.5 Hall Effect and Van der Pauw measurement

Hall Effect

Hall Effect measurements are typically used to characterize electrical properties of a semiconductor, providing information on carrier density and carrier mobility. Figure 3.13 shows a schematic illustration of a system which can be used to perform measurements for Hall Effect, where a conductor studied with a current **I** passing through is placed in a magnetic field **B**. While electrons in the conductor are flowing along -x direction, they are forced to move towards -y direction due to a magnetic Lorentz force. As a consequence, the electrons will accumulate at one side of the conductor, which leads to the formation of an electric field along an opposite direction, i.e., y axis. Once the electric field force is equal to the Lorentz force, a steady state is reached.

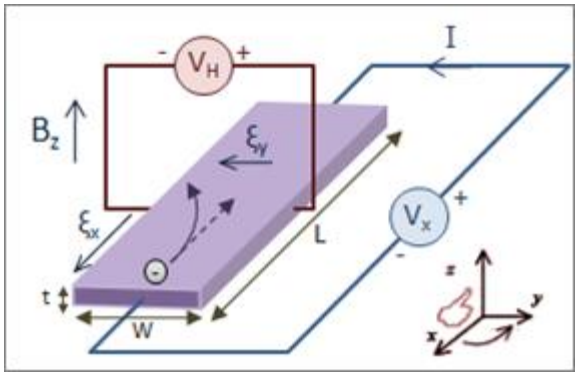

Figure 3.12 Schematic of the setup of the Hall Effect

At a steady state, a Hall voltage can be calculated by using Equation 3.9.

$$\mathrm{qvB} = E_y w = qV_H \qquad (3.9)$$

where q is the electron charge, v is the velocity of the electron, B is the strength of the manganic field; E_y is the electric field along y axis; w is the width of the conductor; m is the effective mass of the charge carrier; and V_H is defined as the Hall voltage.

Hence, a sheet carrier density can be calculated by using equation 3.10.

$$V_H = vB = \frac{IB}{nqwt} = \frac{IB}{q\boldsymbol{n_s}} \rightarrow \boldsymbol{n_s} = \frac{IB}{qV_H} \quad (3.10)$$

where t is the thickness of the conductor; n_s is the sheet density and I is the current applied on the conductor.

Van der Pauw measurement

For standard Hall-effect measurements using the Van der Pauw method, there are some requirements for sample preparation. Firstly, the film thickness must be much smaller than other dimensions of the sample. The shape of the sample needs to be symmetrical, typically a square shape. Metal contacts should be located on the boundary of the sample, in each corner. In addition, in order to minimize any effect as a result of the metal contacts, the ratio of the diameter of the contacts to the length (or width) of the sample needs to be as small as possible.

Figure 3.14 shows a typical setup for Hall-effect measurements using the Van der Pauw method, where a sample holder is placed in a controllable magnetic field and four contacts of the sample are connected to a matrix box which can be used to switch the connection of the circuit between different contacts to a voltage meter and a current source.

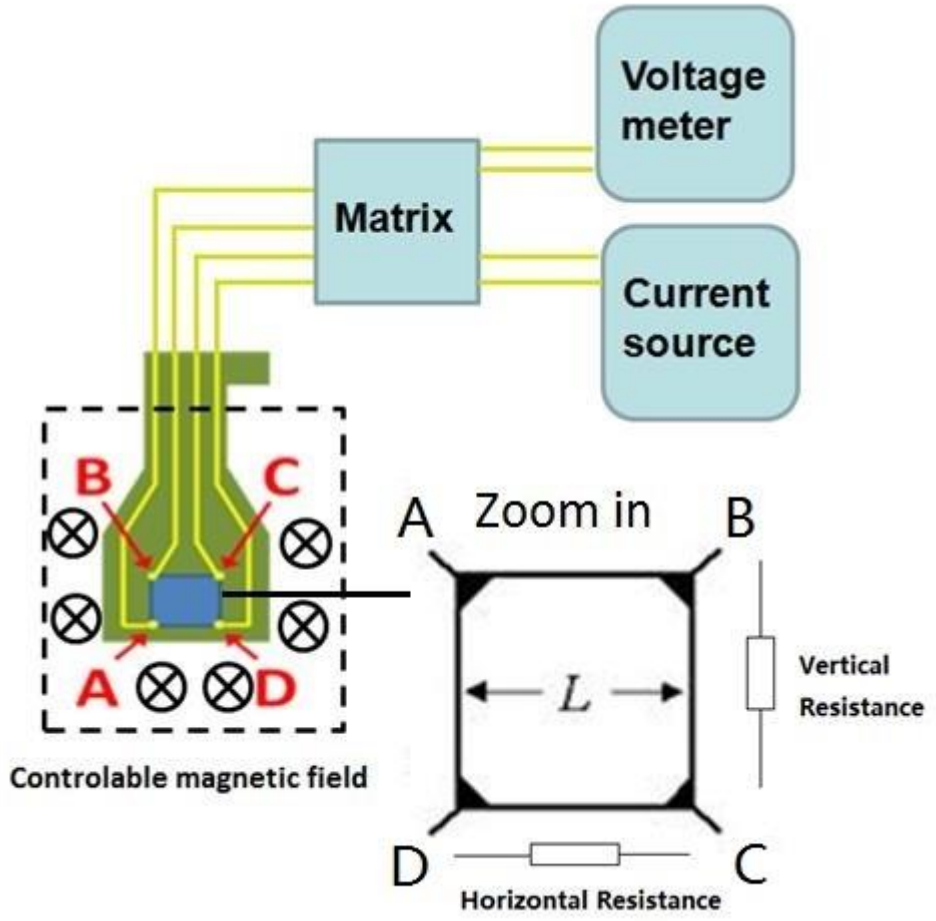

Figure 3.13 Schematic of a sample configuration for Hall-effect measurements using the Van der Pauw method

The first parameter obtained from the Van der Pauw measurements is the sheet resistance of a sample. For measuring the sheet resistance, the magnetic field is turned off and a current is applied. By reading the voltage meter, both vertical and horizontal resistance as shown in Figure 3.14 can be obtained. By using equation 3.11 provided below, the sheet resistance can be calculated.

$$e^{-\pi R_v/R_s} + e^{-\pi R_h/R_s} = 1 \qquad (3.11)$$

where R_s is the sheet resistance, R_v is the vertical resistance, which can be obtained by calculating the average resistance between the metal contacts labeled as AD and BC in Figure 3.14; and R_h is the horizontal resistance, which can be obtained by calculating the average resistance between the metal contacts labeled as AB and CD.

The second parameter obtained from the measurement is the Hall voltage, which can be calculated by using equation 3.12.

$$V_H = \left(V_{AC-plus} + V_{CA-plus} + V_{BD-plus} + V_{DB-plus}\right) - \left(V_{AC-minus} + V_{CA-minus} + V_{BD-minus} + V_{DB-minus}\right) \quad (3.12)$$

where V_H is Hall voltage, $V_{AC\text{-}plus}$ is the voltage between the metal contacts labeled as A and C under the "+" magnetic field direction and $V_{AC\text{-}minus}$ is the voltage between metal contacts labeled as A and C under the "-" magnetic field direction, etc.

3.6 Photoluminescence (PL)

Photoluminescence (PL) measurements are typically used to characterize optical properties of a semiconductor sample. Figure 3.15 (a) and (b) show the schematic illustration of a typical PL system, and an image of our temperature-dependent PL system, respectively. An incident laser beam is reflected by a number of mirrors and finally focused by a lens into a spot with a typical diameter of 100 μm on a sample. The luminescence is collected and then focused by a pair of lenses into the slit of a monochromator. A shutter is also placed in front of the monochromator entrance to control the exposure time on a detector.

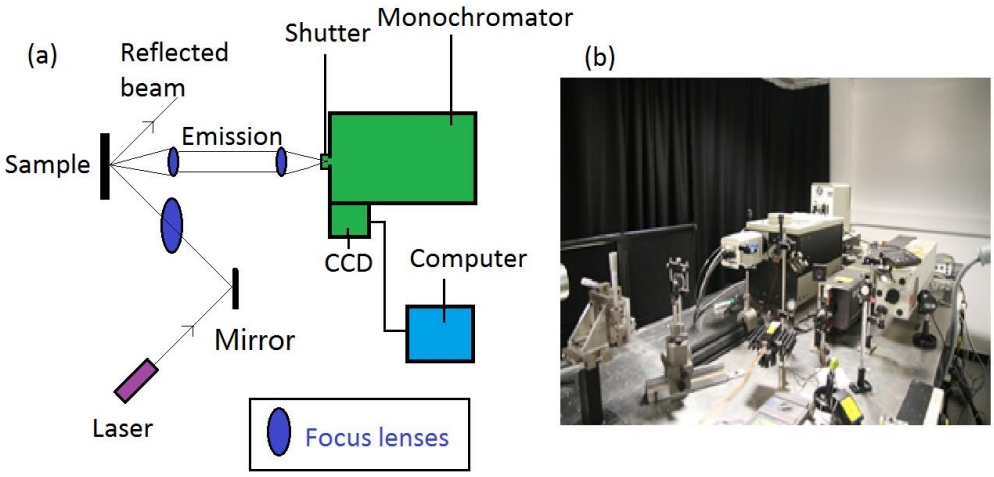

Figure 3.14 (a) Schematic of a typical PL set-up (b) image of our PL system

Chapter 4 Study of high-quality (11-22) semi-polar GaN grown on nano-rod templates

One of the major challenges in “lattice mismatched heteroepitaxy” is due to strain engineering. The typical example is to grow GaN on sapphire, where the lattice mismatch is up to 16% and there further exists a severe thermal stress as a result of the large mismatch in their thermal expansion coefficients in addition to high growth temperatures requested. It is becoming a severe issue with scaling up to larger size substrates beyond 2 inch wafers currently used, leading to enhanced wafer-bowing effects and thus non-uniformity issues. The growth of III-nitrides along semi-polar orientations is becoming increasingly attractive, as they can effectively suppress or eliminate the well-known QCSE resulting from built-in piezoelectric fields, the fundamental limit in further improving GaN-based optoelectronics.[117] Unfortunately, the greatest challenge in growth and fabrication of semi-polar III-nitride optoelectronics is due to the crystal quality of current semi-polar GaN grown on sapphire, which is far behind the requirements for the growth of epiwafers with device performance. Conventional epitaxial lateral overgrowth (ELOG) and the techniques evolved from ELOG have been used to improve the crystal quality of semi-polar GaN. However, the non-uniformity issue remains a great challenge due to the spatial limitations of current standard photolithography. Furthermore, an atomically flat surface cannot be obtained until an overgrown layer has reached 10–20 μm thick.

Recently, we have reported a cost-effective overgrowth technology based on self-organized nickel (Ni) nano-masks, leading to a massively improved crystal quality in both non-polar and semi-polar GaN on sapphire with an atomic flat surface within only a few micrometers.[37,95] It would be worth highlighting that our approach exhibits a major advantage compared with other techniques, such as

nano-imprinting, in terms of costs and process simplicity. Therefore, our approach would be attractive to industry. We can tune both the diameter and the shape of the nano-rods to some degrees by controlling the thickness of the deposited nickel and the temperature of the subsequent annealing process. The details of the fabrication of the nano-rods can be found elsewhere.[37]

In this chapter, a systematic investigation is performed on the overgrown semi-polar GaN layers as a function of the nano-rod diameter of templates, with respect to crystal quality, strain relaxation, wafer bowing and electrical properties.

4.1 Experiment details

4.1.1 Semi-polar GaN nano-rod templates

Standard (11-22) GaN layers with a thickness of around 1.3μm as template are grown using our high temperature AlN buffer layer on 2-in. m-plane sapphire by using low pressure MOCVD.[118]

To be specific, initially, ammonia is flown into the reactor chamber at 550°C to perform a nitridation process in order to ensure that only single phase (11-22) GaN is formed instead of a mixed phase of (10-1-3) and (11-22) GaN.[119] A 250 nm thick high temperature AlN buffer layer is firstly grown on a m-plane sapphire substrate.[86] Subsequently, a thin GaN layer with thickness around 50nm is grown on top of the AlN buffer layer. The growth pressure is 225 torr, this layer is employed to improve the crystal quality of the GaN template. Finally, a 1.3μm thick GaN is grown under a growth pressure of 75 torr,[120] and an atomic flat surface can be obtained.

The as-grown wafer undergoes an ex-situ nano-rod fabrication process.[37] Simply speaking, a layer of SiO_2 is initially deposited on the as-grown GaN, followed by preparing a thin layer of Ni film on its top and a subsequent annealing process in order to form self-organized Ni nano-islands as masks for further etching into GaN nano-rods as templates. The diameter of the final GaN nano-rods is determined by the size of the formed Ni nano-islands, which can be controlled through tuning the

thickness of the nickel film deposited and the subsequent annealing process, such as annealing temperature. Figure 4.1 shows the schematic of our fabrication procedure. Figure 4.2 is a SEM image of our typical nano-rod array template.

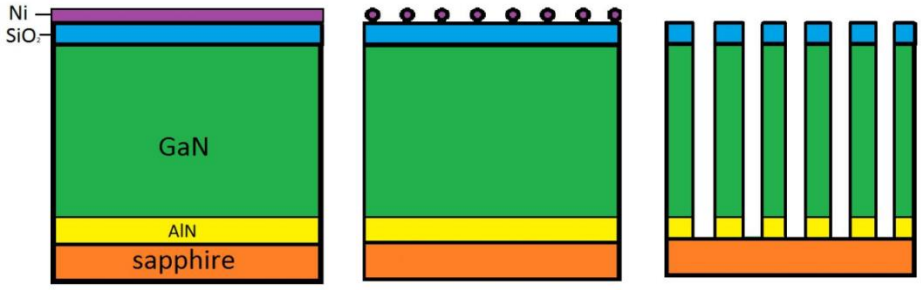

Figure 4.1 Schematic of our nano-rod template fabrication

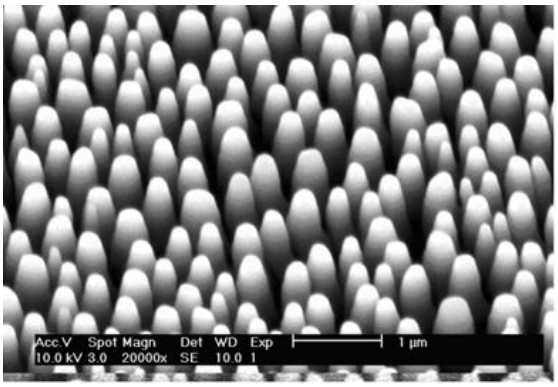

Figure 4.2 SEM image of nano-rod template

In order to evaluate the average nano-rod diameter, standard SEM measurements are initially performed in a top view scan mode. As an example, a top view SEM image of the nano-rods is shown in Figure 4.3, and then the US National Institutes of Health image analysis software (ImageJ) is utilized to process the SEM image in order to determine the average nano-rod diameter. This open source software has been utilized for particle analysis across a range of topics[121-123]. By the means of ImageJ the SEM image can be processed into digital signals, and also converted into a high contrast SEM image in white and black colors as shown in Figure 4.3 (b). Finally, the average diameter of nano-rods can be obtained. In this study, a series of nano-rod templates with diameters ranging from 300 to 827 nm have been prepared. Additionally, the samples grown on nano-rod template with an

average diameter of 300 and 827 nm have been defined as sample A and B, respectively.

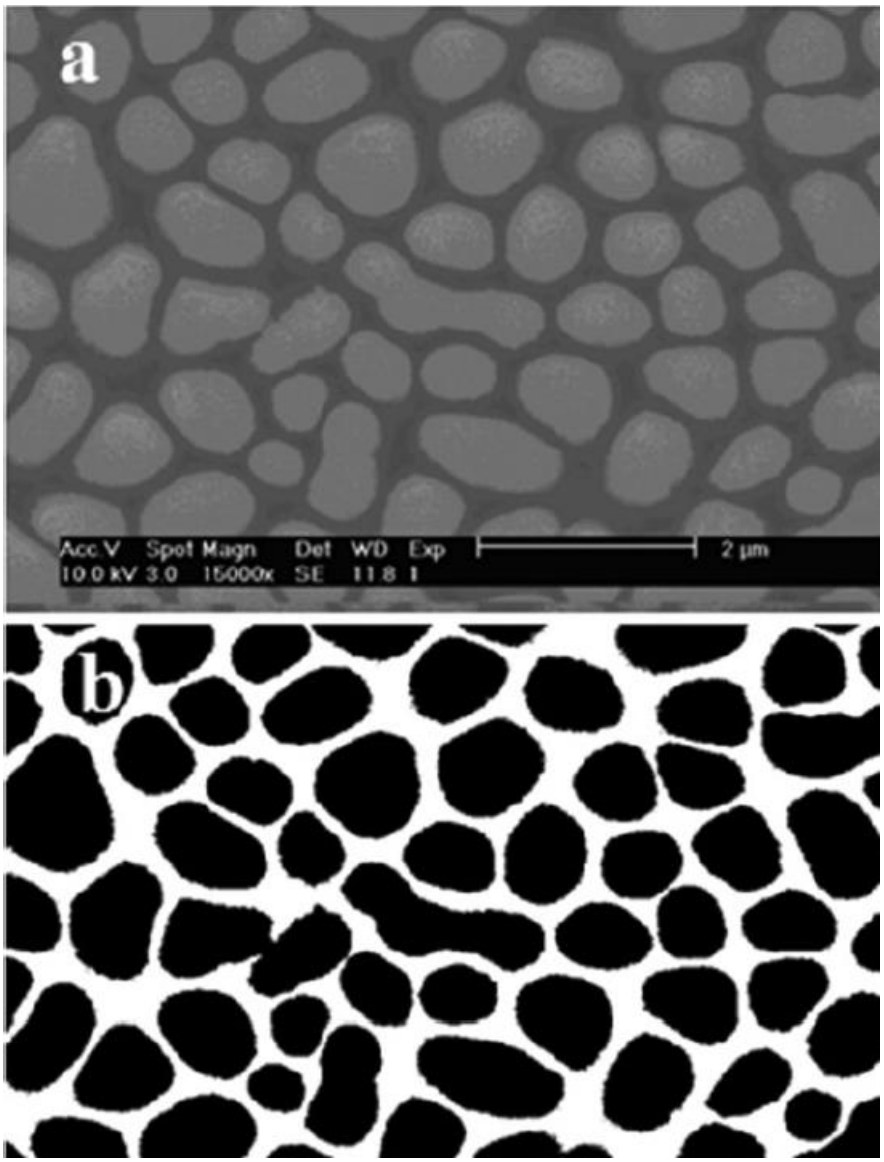

Figure 4.3 (a) Typical top-view SEM image of nano-rods (b) processed SEM image by using ImageJ.

4.1.2 Overgrowth of semi-polar (11-22) GaN

The individual nano-rod template is reloaded into the reactor chamber of the MOCVD for subsequent overgrowth. For all overgrown layers, the total thickness is about 5μm in each case. All samples are nominally undoped. The overgrowth

procedure is a single step GaN growth with a V/III ratio of 1600. The growth temperature and pressure are 1120°C and 75torr, respectively.

As shown in Figure 4.4, the overgrowth initiates from the sidewalls of GaN nano-rods as GaN cannot directly grow on the SiO_2 nano-masks. Due to the fast lateral growth, air voids are formed when the growth fronts from the sidewalls meet each other. Then, the growth extends laterally over the SiO_2 nano-masks and completes the coalescence process eventually. An atomically flat surface can be obtained with an overgrown thickness of around 5 μm. It is worth highlighting that a quick coalescence (less than 1 μm) is observed by an in-situ optical monitoring system.

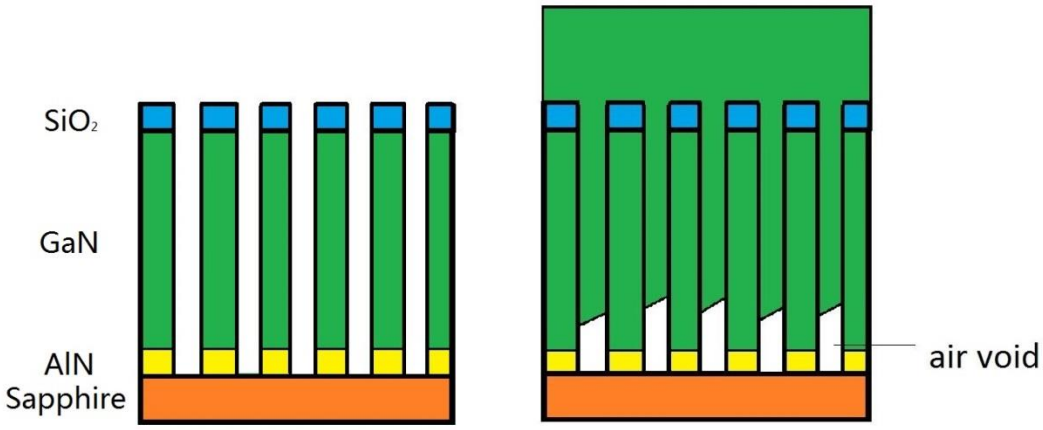

Figure 4.4 Schematic of our GaN overgrowth process

4.2 Surface characterizations of overgrown (11-22) GaN

Both AFM and SEM have been used to characterize the surface morphology of our overgrown semi-polar (11-22) GaN. Figure 4.5 (a) shows a typical AFM image of our overgrown sample, demonstrating a root mean square (RFM) roughness of 1.46 nm. The detailed AFM study of the samples grown on the nano-rod templates with a nano-rod diameter ranging from 300 to 800 nm indicates that there is no a direct relationship between surface roughness and nano-rod diameter. In order to examine

a large area, Figure 4.5 (b) shows a typical optical microscopy image with 1000x magnification, showing a clear smooth surface with weak stripe features.

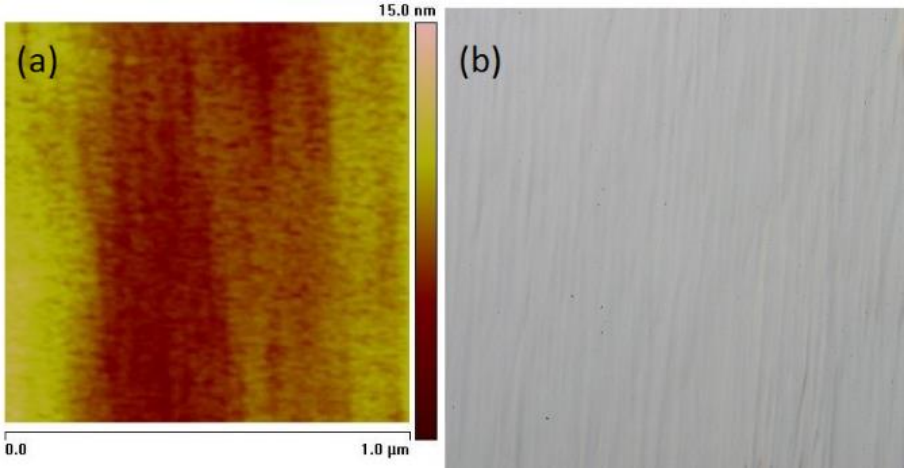

Figure 4.5 Typical AFM image (a) and optical microscopy image with 1000 × magnification (b) of the overgrown semi-polar GaN.

4.3 Influence of nano-rod diameter on overgrown semi-polar GaN

4.3.1 Influence of nano-rod diameter on crystal quality

Bruker D8 high resolution XRD (HRXRD) with a four bounce Ge (022) monochromator is utilized for the material characterization of the overgrown GaN layers. Unlike c-plane GaN, semi-polar GaN exhibits an anisotropic nature in properties and crystal quality. Therefore, XRD rocking curve measurements as a function of an azimuth angle are used to study the crystal quality of the overgrown semi-polar GaN layers. 0° and 90° azimuth angles are defined when the projection of incident x-ray beam is parallel to (1-100) and (11-2-3) orientations of semi-polar (11-22) GaN, respectively. Typically, the rocking curve measurements along (1-100) and (11-2-3) directions (i.e., at the azimuth angles of 0° and 90°, respectively), which provide the maximal and minimal line-width (FWHM) for each sample, are simply used to make comparison of crystal quality.

Using two extreme cases as examples, Figure 4.6 shows FWHM of the XRD rocking curve measurements of two overgrown semi-polar GaN (300 and 827 nm nano-rod as templates, respectively) as a function of an azimuth angle (the XRD rocking curves along (1-100) and (11-2-3) orientation of these two samples are shown in Figure A.1 and A.2 of appendix A, respectively). Clearly, the overgrown semi-polar GaN layer on the nano-rod template with a large nano-rod diameter exhibits much narrower FWHM compared with the overgrown semi-polar GaN layer obtained using small nano-rods as a template.

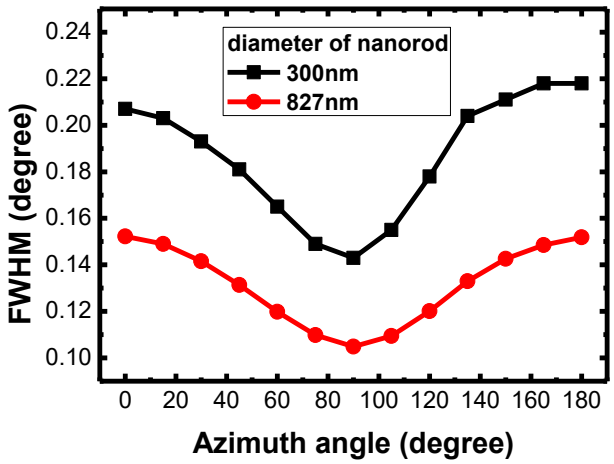

Figure 4.6 FWHMs of XRD rocking curves as a function of azimuth angles for two overgrown samples using nano-rod arrayed templates with different nano-rod diameters

Figure 4.7 shows the FWHMs of the XRD rocking curves measured along the (1-100) and (11-2-3) directions as a function of nano-rod diameter from 300 to 827 nm, demonstrating a clear trend, namely, the FWHMs along both directions are reduced with increasing nano-rod diameter (the XRD rocking curves along (1-100) and (11-2-3) orientation of the second best sample which overgrown on template with 800nm diameter is shown in Figure A.3 of appendix A). In detail, the FWHMs of the XRD rocking curves have been reduced down to 0.152° along (1-100) direction and 0.104° along (11-2-3) direction, respectively. These results are comparable to the XRC data from other reports.[124,125]

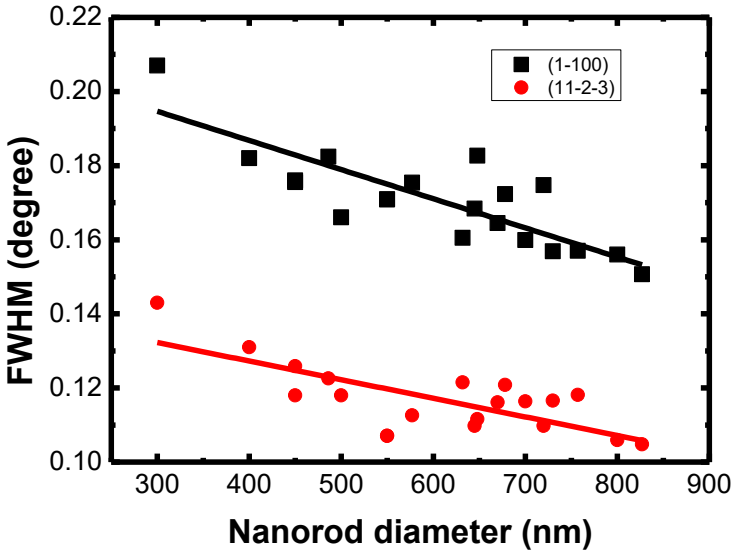

Figure 4.7 FWHM of XRD rocking curves as a function of the nano-rod diameter, the solid lines are the linear fittings of the FWHMs of XRD rocking curve along (1-100) and (11-2-3), respectively

4.3.2 Influence of nano-rod diameter on strain relaxation

XRD reciprocal space mapping (RSM) measurements have been performed to study the strain. Standard RSM measurements have been performed along asymmetric (11-24) direction. Simply, the reciprocal lattice point (RLP) of the m-plane sapphire substrate along (40-44) direction has been used as a reference assuming that sapphire is fully strain-relaxed (or at least the strain which sapphire suffers is negligible or equal for all the samples) due to its much larger thickness (430μm) than that of the overgrown layers. These two crystal planes are chosen because they are relatively close to each other in reciprocal space and both have reasonable XRD intensities. The scanning range in each RSM measurement is shown in Figure 4.8.

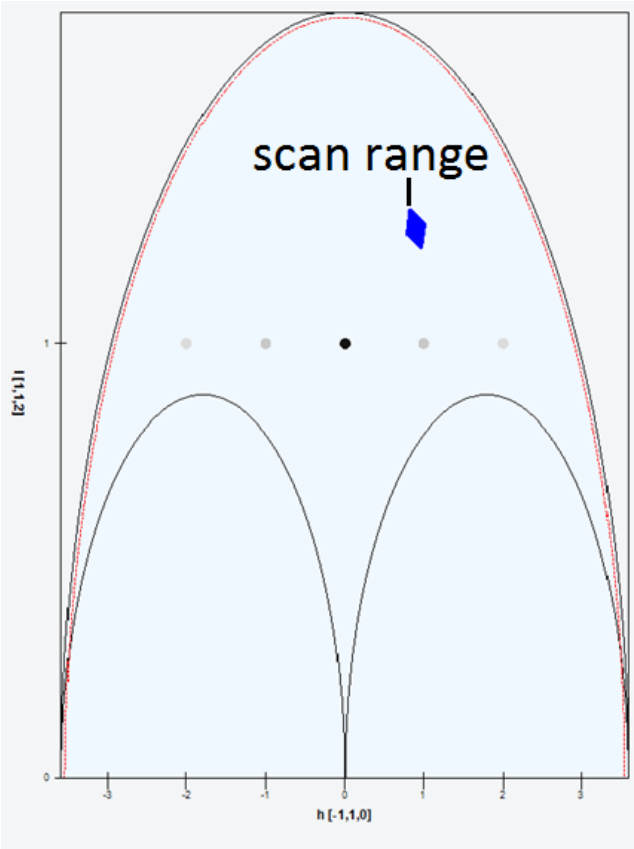

Figure 4.8 Schematic of the RSM scanning range in an Edwald sphere.

Figure 4.9 (a) and (b) shows the RSMs of sample A and B, respectively, as two extreme cases. In each case, two RLPs have been obtained, corresponding to (40-44) sapphire and (11-24) GaN, respectively. The coordinates of each RLP on q(x) and q(z) axis represent its in-plane and out-of-plane lattice constants for each individual layer, respectively. Comparing the RLP of the GaN between sample A and B, there is a clear shift, indicating that sample A and B exhibit different strain relaxation.

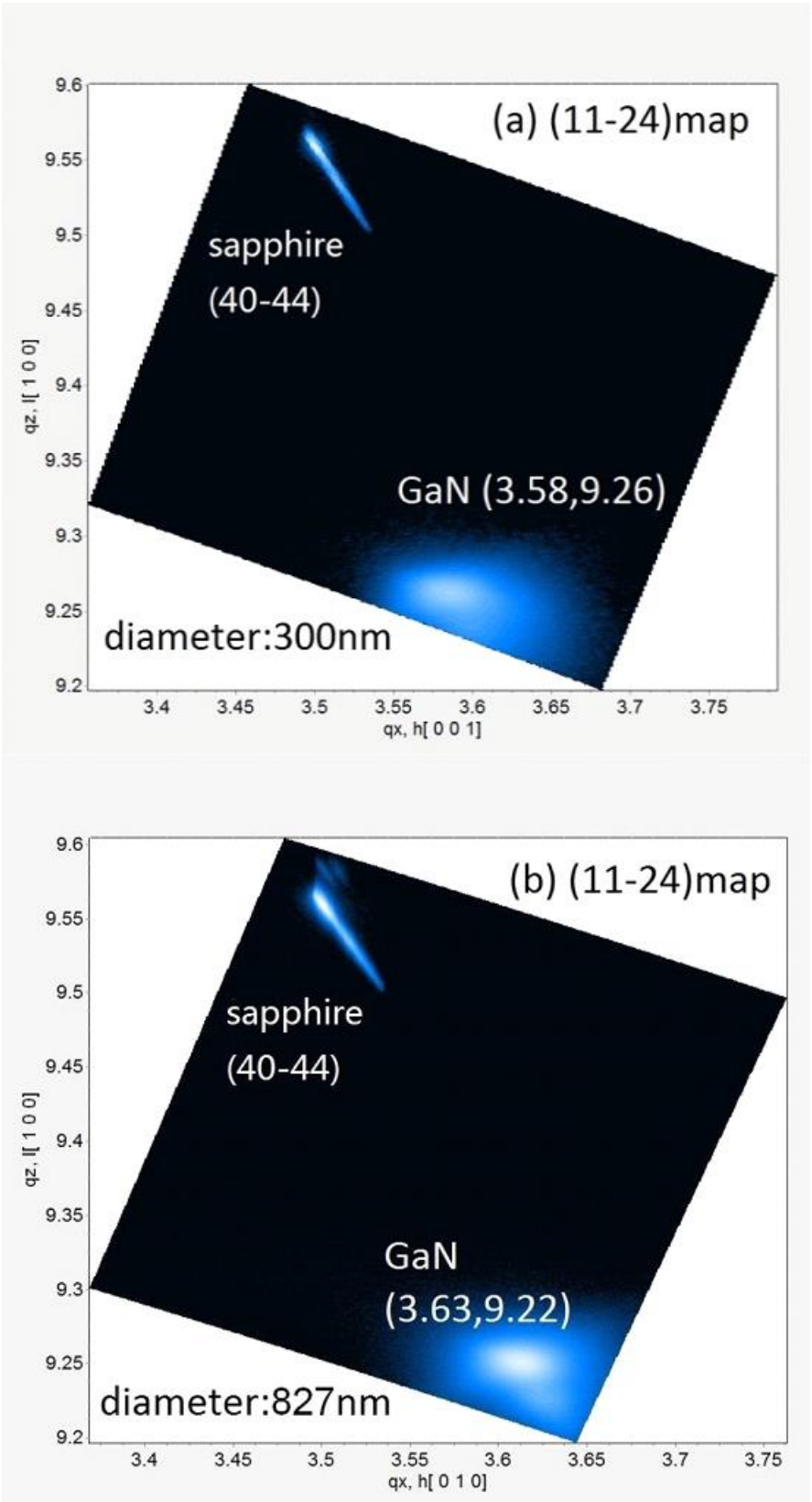

Figure 4.9 RSMs of (a) sample A and (b) sample B

In order to calculate the strain relaxation of the overgrown GaN layers, the coordinates of the GaN RLP from the RSM need to be normalized by using the RLP of

sapphire as a reference. Figure 4.10 shows the normalized coordinates of overgrown GaN and theoretically strain-free GaN as a function of nano-rod diameter, respectively, exhibiting that the RLP coordinate of the overgrown GaN approaches that of the strain-free GaN with increasing a nano-rod diameter.

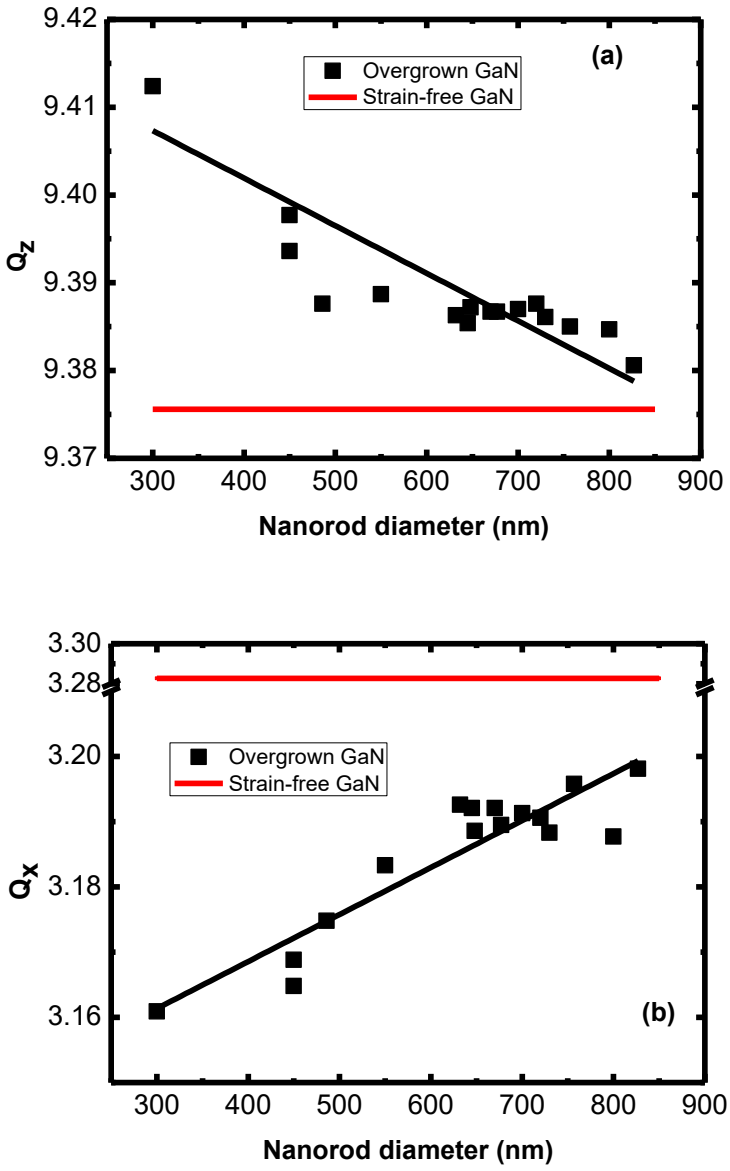

Figure 4.10 (a) Q_z and (b) Q_x of our overgrown GaN as a function of nano-rod diameter, respectively. The data from strain-free GaN are also provided as a reference (red solid lines), the black solid lines are the linear fittings of Q_z and Q_x value, respectively

Furthermore, the strain of the overgrown GaN layers can be calculated using equation 4.1 while the tilting angle of the overgrown layer needs to be taken into

account.

$$\epsilon = \frac{a_{measured} - a_{free}}{a_{free}} = \frac{\frac{1}{q_{measured}} - \frac{1}{q_{free}}}{\frac{1}{q_{free}}} \quad (4.1)$$

Where the $a_{measured}$ is the measured lattice constant, a_{free} is the theoretical value of lattice constant, $q_{measured}$ is the measured RLP coordinate of semi-polar GaN, and q_{free} is the theoretical RLP coordinate of semi-polar GaN.

The strain of a series of overgrown samples grown on nano-rod templates with different nano-rod diameters is shown in Figure 4.11, indicating that the strain reduces from 0.001 to 0.00016 with the increasing nano-rod diameter from 300 to 827 nm.

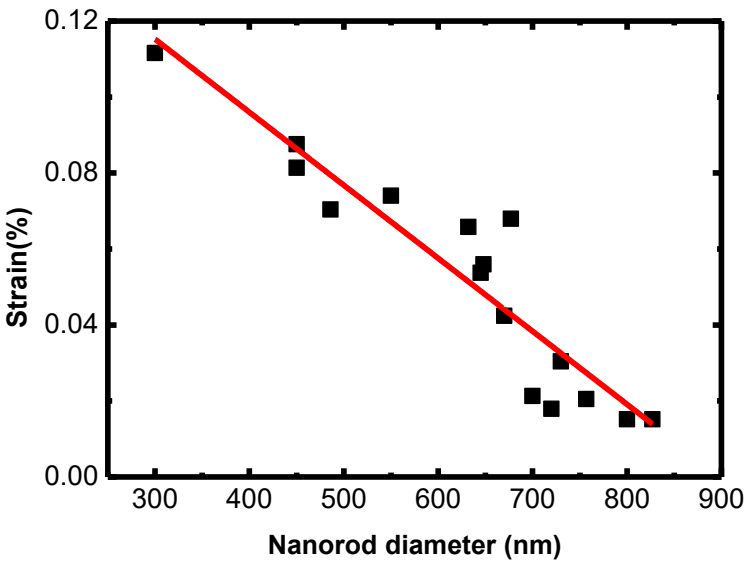

Figure 4.11 Strain relaxation as a function of nano-rod diameter, the solid line is the linear fitting of the strain relaxation

4.3.3 Influence of nano-rod diameter on wafer curvature

XRD rocking curve measurements on different points of a 2 inch wafer are used to determine wafer curvature. XRD rocking curve measurements are initially performed when the x-ray beam is incident on the center of a 2 inch wafer with the

projection direction of the incident x-ray beam parallel to GaN (11-2-3) direction. Afterwards, the wafer is moved along the (11-2-3) direction by a certain distance, for example, 5mm in our study, and XRD rocking curve measurements are then performed once again. In this case, the XRD intensity cannot reach its maximal value due to wafer bowing effects. Therefore, by only tuning the sample stage by angle "***α***", the maximized XRD intensity can be obtained. Assuming that the moving distance of the wafer is small enough, the tuned angle is approximately equal to the difference in Bragg's angle between the XRD rocking measurements before and after moving the wafer. The radius of the wafer due to wafer bowing effect can be calculated by using equation 4.2.[126] The schematic of the XRD curvature measurement is shown in Figure 4.12.

$$\mathrm{R} \cong \frac{x}{a} \qquad (4.2)$$

$$R \equiv {}^{1}/_{k} \qquad (4.3)$$

where ***α*** is the offset angle between the two rocking curve measurements mentioned above; x is the moving distance of the wafer along the GaN (11-2-3) direction; k is the wafer curvature; and R represents the radius of wafer curvature.

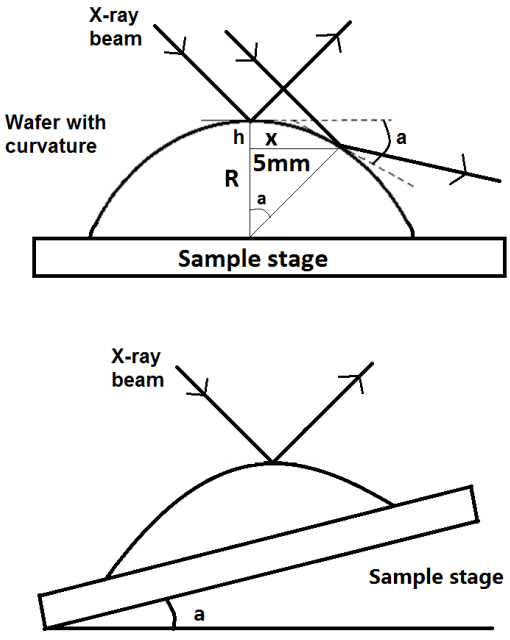

Figure 4.12 Schematic of our curvature measurements

Typically, the tuned angle is on the order of 10^{-4} rad, and thus Equation 4.2 can provide a fairly accurate wafer curvature. Figure 4.13 shows a typical example, where the tuned angle is approximately 0.0008 rad and the moving distance between the two XRD measurements is 5 mm.

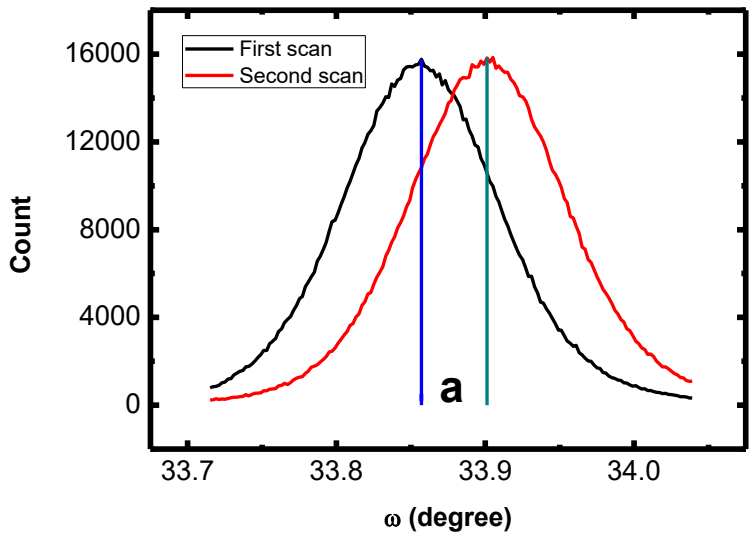

Figure 4.13 XRD rocking curves before and after moving the wafer, the solid lines indicate the peak positions of two rocking curves

The wafer curvatures of a series of overgrown samples are shown in Figure 4.14. The nano-rod diameters of these samples are ranging from 300 to 827 nm. As shown in Figure 4.14, the wafer bowing reduces from 2980 to 638 km^{-1} with increasing nano-rod diameter.

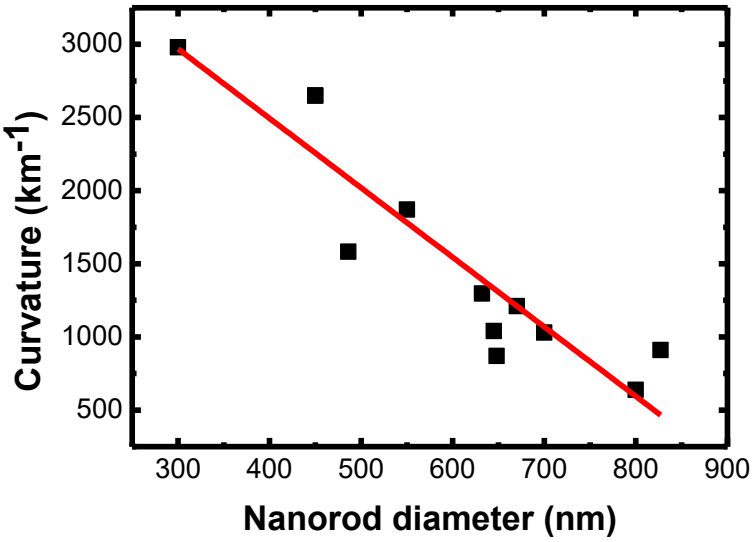

Figure 4.14 wafer curvatures as a function of the nano-rod diameter, the solid line is the linear fitting of the wafer curvatures

4.4 Study of anisotropic electrical properties in semi-polar (11-22) GaN

The electrical properties of the overgrown samples have been investigated by Hall Effect measurements via the Van der Pauw method. However, the standard Van der Pauw measurement can only allow us to obtain isotropic in-plane sheet resistance, and thus isotropic carrier mobility. Semi-polar (11-22) GaN exhibits intrinsically anisotropic properties, for example, FWHMs of x-ray rocking curve for standard c-plane GaN remains constant while those of semi-polar (11-22) GaN exhibit an anisotropic behavior as a function of azimuth angle, as shown in Figure 4.15 (the XRD rocking curve of the c-plane sample is shown in Figure A.4 of appendix A). Therefore, the standard Van der Pauw measurement cannot be applied in the measurements of anisotropic semi-polar GaN.

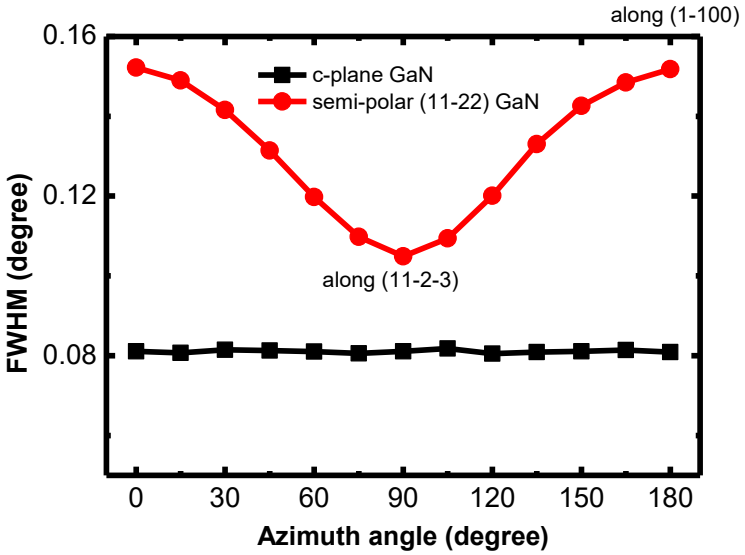

Figure 4.15 FWHMs of x-ray rocking curves as a function of azimuth angles for standard c-plane and semi-polar GaN

In this Chapter, we employed the transmission line model (TLM) method to measure directional dependent sheet resistance, which allows us to obtain electron mobility of semi-polar GaN along different orientations. The standard Van der Pauw method is used to measure the sheet electron density of our semi-polar GaN samples.

4.4.1 Sample preparation

For van der Pauw method

As discussed in section 3.5, a sample used for standard Van der Pauw measurement has to be symmetrical in shape, ideally a square shape. Since our semi-polar (11-22) GaN is grown on m-plane sapphire, it is very difficult to cleave the sapphire substrate along (1-100) direction. Furthermore, it is also very difficult to use a combination of a standard photo-lithography technique and subsequent dry etching to form such a very regular shape, as a photo-resist adopted to protect the underlying materials (including 5μm GaN, 500nm SiO_2 and 250nm AlN buffer) cannot stand for the long dry-etching time required.

In this work, by attaching a Si (111) substrate on the top of an overgrown GaN, a

new etching method has been developed to fabricate a square-shaped semi-polar GaN sample on m-plane sapphire. A schematic of our fabrication procedures is shown in Figure 4.16. Firstly, a photo-resist is spun on the top of a sample, followed by attaching a cleaved Si substrate with a regularly square shape on the top of the photo-resist layer. It is easy to obtain a square-shaped Si substrate by a simple cleavage. Afterward, the sample is baked on a hot plate at 100°C for 1 min to make the photo-resist dry and stable so that the Si substrate can be adhesive to the GaN sample very well. The sample is then exposed to UV light with 300nm wavelength by using Karl Suss Mask Aligner, followed by developing in pure MF26A developer for 1 min. Subsequently, an ICP etching with a power of 300 watt is performed on the GaN sample for 25 mins. Both this long-time and the high power ICP etching ensure that the exposed GaN can be etched off entirely. Then, acetone solution is used to remove the photo-resist and the attached Si substrate, leaving the square-shaped GaN on the top of the m-plane sapphire.

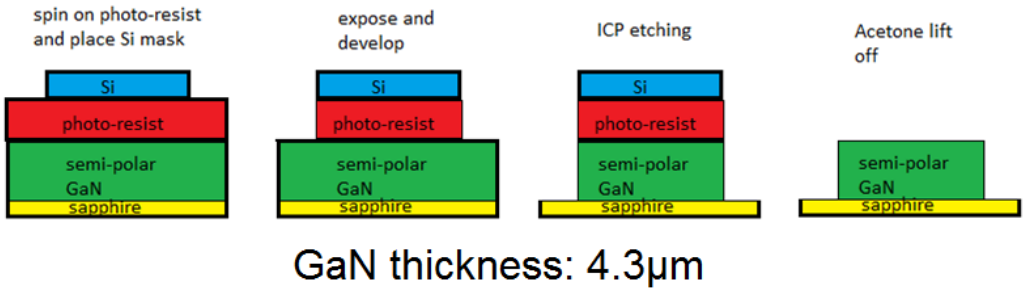

Figure 4.16 Schematic of our fabrication procedure of a square-shaped GaN sample

The top view of the etched GaN sample is shown in Figure 4.17, showing that the dimension of the remaining GaN sample is $0.8\ mm \times 0.8\ mm$. Finally, four standard metal alloy contacts (Ti/Al/Ti/Au with their thicknesses of 30/100/30/150 nm) are deposited on each corner of the GaN sample using a thermal evaporator technique. I-V measurements are performed to confirm its linearly ohmic characteristic and the typical curve is shown in Figure 4.18.

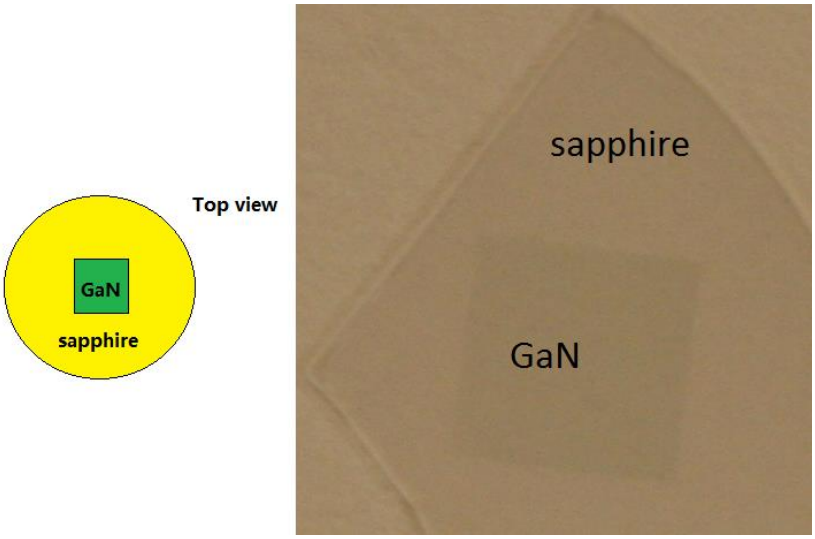

Figure 4.17 Optical image of an etched square-shaped GaN on a sapphire substrate

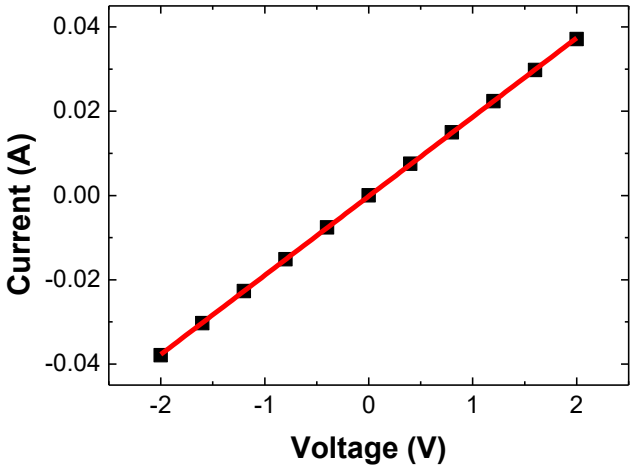

Figure 4.18 Typical I-V curve of the GaN sample for Van der Pauw measurements to confirm ohmic contacts.

As the sample is under a long time ICP etching process, there are some concerns about the etching induced damage on the edge part of the GaN sample, leading to un-accurate results of the Van der Pauw measurements. Therefore, top view SEM measurements have been performed, as shown in Figure 4.19 (a) and (b). The damaged region due to the ICP etching is about 28.2μm width, which is much narrower than the diameter of the metal contact (normally about 0.5mm). Figure 4.19 (b) shows a typical damaged area on the corner of the sample, indicating a similarity to that of the edge area. Therefore, it is safe to use such ICP etching

process to fabricate a square-shaped sample for Van der Pauw measurements without any concern.

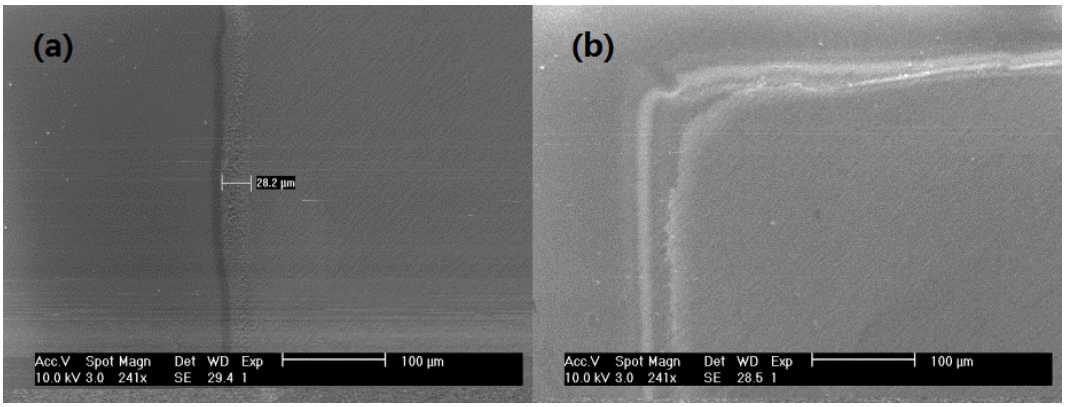

Figure 4.19 typical SEM images of the (a) edge part and (b) corner of the GaN sample after the ICP etching

Transmission-line-model (TLM) measurement

The directional dependent sheet resistance is measured using a TLM method. TLM is a useful tool to obtain the sheet resistance of the semiconductor layer. As shown in Figure 4.20, the structure consists ohmic contacts with different space between them. When a current is applied between any pair of the contact, assuming the sheet resistance is uniform underneath the contacts and in the gap, the total resistance can be calculated by equation 4.4.

$$R_t = 2R_c + \frac{R_{sh}}{W}L \qquad (4.4)$$

Where R_t is the total resistance between any pair of contact, R_c is the contact resistance, R_{sh} is the directional sheet resistance, W is the width of contact pads and L is the space between two contacts.

TLM patterns along the (1-100) and (11-2-3) directions have been fabricated by standard photo-lithography with a TLM mask. Firstly, two standard photo-lithography processes are performed by aligning the TLM mask along (11-2-3) and (1-100) orientation of the GaN sample, respectively. Then, the contacts are deposited, followed by a standard lift-off process. Ti/Al/Ti/Au alloy with their thicknesses of 30/100/30/150nm has been used in order to allow us to achieve good ohmic contacts. The top-viewing SEM image of the sample for the TLM measurements is shown in Figure 4.20 while the distances between the metal alloy contacts from left

to right are 2/5/10/15/20 μm, respectively. By measuring the resistance between these contacts, the directional dependent sheet resistance can be obtained.

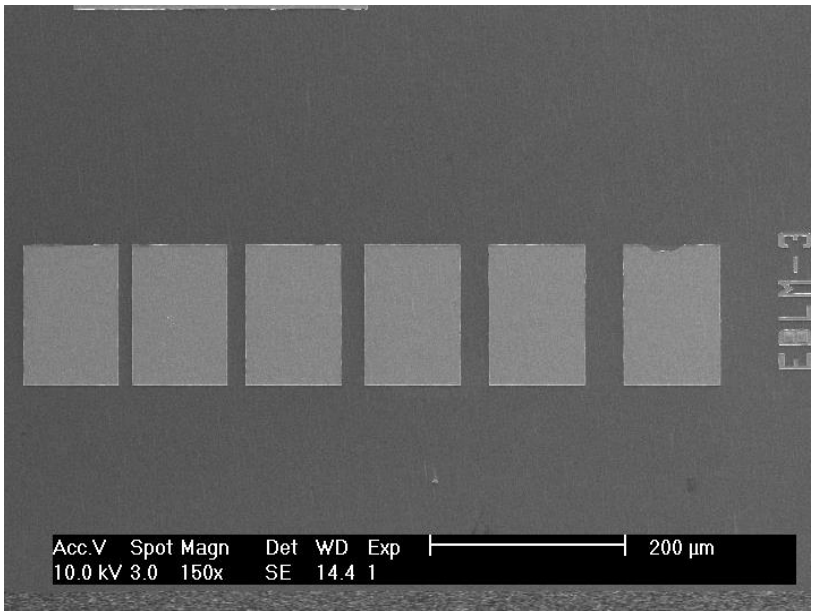

Figure 4.20 Top-viewing SEM image of the samples for TLM measurements

4.4.2 Results and discussion

Electron mobility along both orientations increase with nano-rod diameter

The free electron sheet density can still be obtained by the standard Hall Effect measurements. A sample holder with four contacts is placed in a space with a controllable magnetic field. The four contacts are connected to a matrix box which connects to a voltage meter and a current source. In this work, the applied current is 2mA and the strength of the magnetic field is 0.56 T.

Equation 4.3 has already been discussed in section 2.2.5. In order to obtain electron mobility, the sheet resistance and the sheet electron density are required.

$$\mu = 1/(q\boldsymbol{n_s}\boldsymbol{R_s}) \quad (4.3)$$

For semi-polar GaN, the sheet resistance exhibits anisotropic characteristics. Thus, equation 4.3 is manipulated into equation 4.4, which allows us to calculate the orientation dependent electron mobility.

$$\mu_{orientation} = {}^{1}/_{q\boldsymbol{n_s}\boldsymbol{R_{s-orientation}}} \quad (4.4)$$

Where the $\mu_{orientation}$ is the orientation dependeent electron mobility, q is electron

charge, n_s is sheet density and $R_{s\text{-}orientation}$ is the orientation dependent sheet resistance.

Figure 4.21 shows the directional dependent electron mobility along both (1-100) and (11-2-3) directions as a function of nano-rod diameter, performed at room temperature. Furthermore, with increasing nano-rod diameter, the electron mobility can be enhanced from 83 to 228 $cmV^{-1}s^{-1}$ along (1-100) direction and 51 to 124 $cmV^{-1}s^{-1}$ along (11-2-3) direction, respectively. To our best knowledge, the electron mobility as high as 228 $cmV^{-1}s^{-1}$ with an electron concentration of $3.42 \times 10^{17} cm^{-3}$ is the best result for semi-polar GaN grown on sapphire substrates.[127-129]

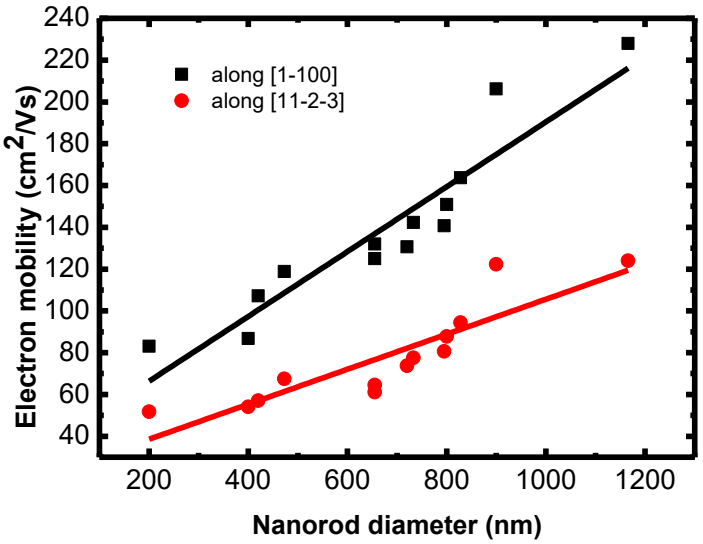

Figure 4.21 electron mobility as a function of nano-rod diameter along different orientations, the solid lines are the linear fittings of the electron motilities along [1-100] and [11-2-3], respectively

4.5 Conclusion

A systematic study has been performed on a series of overgrown semi-polar GaN layers grown on the nano-rod templates with different diameters in order to investigate the influence of nano-rod diameter on the crystal quality, strain, wafer bowing, and electrical properties of the overgrown layers. Our results demonstrate

that with increasing the nano-rod diameter, the crystal quality can be significantly improved, agreeing with the electrical properties. In detail, room temperature electron mobility of as high as 228 $cmV^{-1}s^{-1}$ has been achieved. Furthermore, larger nano-rods also lead to enhanced strain relaxation, and thus reduction in wafer bowing effects.

Chapter 5 Photo-chemical etching of semi-polar (11-22) GaN

The mechanism of chemical wet etching involves a number of chemical reaction processes (typically reduction and oxidation reactions), which can remove unwanted materials.[130] An etching rate is normally determined by crystal quality, etching temperature, the concentration of chemical solution and alloy composition. It also depends upon crystal facets which are exposed to an etchant used. For example, the etching rate of (0001) orientated GaN surface is much slower than that of (1-100) orientated GaN surface under identical conditions. The anisotropic nature in chemical wet etching rate[131] allows us to obtain selective etching on semi-polar (11-22) GaN.

In this Chapter, a photo-assisted wet etching approach has been established for a surface treatment on micro-rod templates prior to any overgrowth process, aiming to reduce or eliminate any damages induced as a result of dry-etching and hence facilitate subsequent overgrowth. As introduced in Chapter 4, the as-grown template needs an ex-situ fabrication process in order to be fabricated into micro-rod arrays before it is reloaded into the reactor for overgrowth, where a dry-etching process is performed. Consequently, some residues or damages are introduced as a result of the dry etching. Therefore, a chemical wet etching process is performed as a standard process to remove these damages. Moreover, there is a large difference in etching rate for different orientations in GaN. For c-plane GaN with Ga-polarity, the etching rate is extremely slow at room temperature and only defect sites can be etched. For other crystal planes, e.g. non-polar or semi-polar planes, the etching rate varies but is normally faster than that of c-plane under identical etching conditions.

In order to obtain an efficient etching rate at room temperature, a photo-assisted etching process has been established by introducing an ultraviolet (UV)

source. UV light is incident on GaN surface in a chemical solution, generating free electron-hole pairs, which can enhance oxidation and reduction reactions, and even c-plane GaN with Ga-polarity can be effectively etched.

It is well-known that potassium hydroxide (KOH) solution is one of the best option as a chemical etchant for GaN wet etching. Compared with H_3PO_4 solution, it is more efficient under the condition of UV illumination.

In this work, a combination of KOH solution and a Xenon lamp is introduced to perform a photo-assisted etching process. In order to achieve optimal conditions, a detailed investigation on the etching rates of GaN on different crystal planes and as a function of KOH concentration has been carried out. A systematic study has been carried out, and optimized wet etching conditions on the surface treatment of semi-polar (11-22) GaN micro-rod arrays have been obtained.

5.1 Experiment detail

5.1.1 Semi-polar GaN micro-rod arrayed template

Based on the results in Chapter 4, the crystal quality of the overgrown semi-polar (11-22) GaN can be further improved by increasing nano-rod diameter. However, by using the self-organized Ni mask approach, we have achieved a nano-rod diameter of up to 1 μm. It is extremely difficult to further increase it. In addition, overgrowth on regularly arrayed templates with designed diameters and spacing is very important for us to build a clear growth model for further investigation of overgrowth mechanisms. Furthermore, it is extremely difficult to apply the self-organized Ni nano-mask approach on larger (4 inch and above) sapphire substrates.

In order to address the above issues, our group has developed regularly arrayed micro-rods as a template for overgrowth by means of a combination of a standard photolithograph technique and subsequent dry-etching process, where the micro-rod diameter and the spacing between micro-rods can be accurately

controlled.[96] The detailed fabrication procedure of the micro-rod array templates can be found in one of the previous Ph.D. thesis in our group.[132] Figure 5.1 shows a bird-eye-view SEM image of our typical micro-rod arrayed template, where the micro-rod diameter is 2.5 µm.

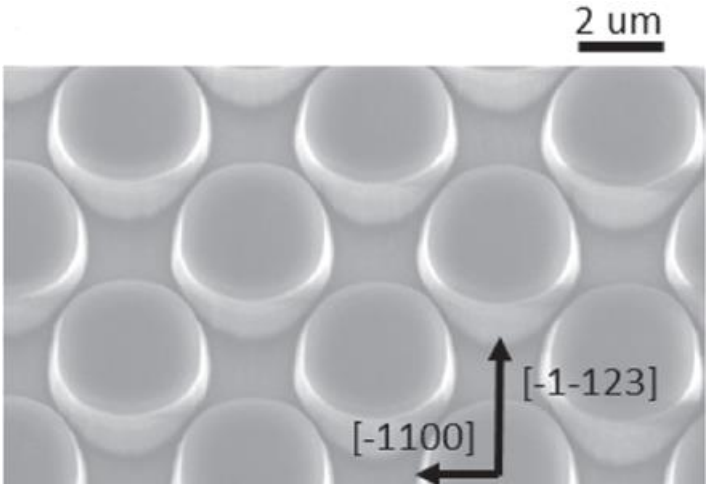

Figure 5.1 bird-eye-view SEM image of our typical micro-rod arrayed template

5.1.2 Photo-assisted etching (PAE)

In this work, photo-assisted chemical wet-etching has been performed on semi-polar (11-22) GaN micro-rods as a function of KOH concentration and as a function of GaN facet, where etching rates have been systematically studied.

The experimental setup for the PAE is sketched in Figure 5.2. A Xenon lamp with an output power of 450W is used. The measured power density is about 1 W/cm^2 with emission wavelength at 325nm. An aluminum-coated UV mirror is used, allowing the UV light to be incident on the sample which is immersed in KOH solution in a baker. In addition, a safety box is used to prevent any UV light being scattered out of the box.

There is no any heater used for the experiment set-up. The chemical solution in the beaker would be heated up to around 55°C as a result of UV illumination.

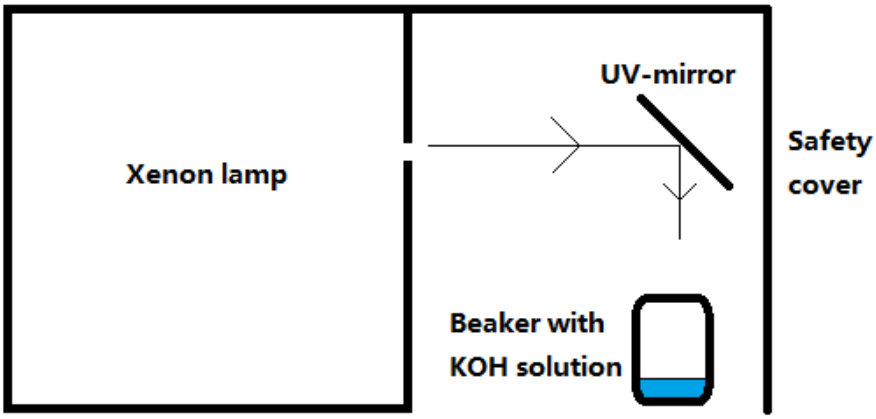

Figure 5.2 Schematic of our photo chemical etching set-up

The major factor which determines the etching rate in this work is the concentration of the KOH solution used. In addition, the damage degree of the fabricated micro-rod arrays as a result of ICP etching has also been found to affect the etching rate. Therefore, three sets of samples have been designed to investigate the influence of KOH concentration, etching time and ICP etching parameter on etching rate, respectively.

After the PAE experiments, SEM is used to observe the etching results of the semi-polar GaN micro-rod template and XRD is used to identify the crystal orientations.

5.2 Results and discussion

5.2.1 Semi-polar GaN micro-rod template

Figure 5.3 shows a bird view SEM image of a semi-polar GaN micro-rod template captured with a tilted angle at 20° and the geometric relationship between micro-rods and its oriented sidewalls. The SEM image demonstrates highly regular micro-rod arrays in terms of the shape and the diameter of micro-rods and the spacing between micro-rods.

It is well-known that GaN laterally overgrown along the c-direction is defect-free. Therefore, the growth along the c-direction can effectively block the a-direction

grown GaN,[133] if the growth rate of GaN along the c-direction is much higher than that along the a-direction. This can be achieved by optimizing the overgrowth conditions and optimizing surface treatment on the sidewalls of micro-rods. For the latter, the c-oriented sidewalls should be slightly etched, while other orientated sidewalls are preferred to be strongly etched making the initial lateral growth along these orientations more difficult and thus enhancing the growth along the c-orientation.

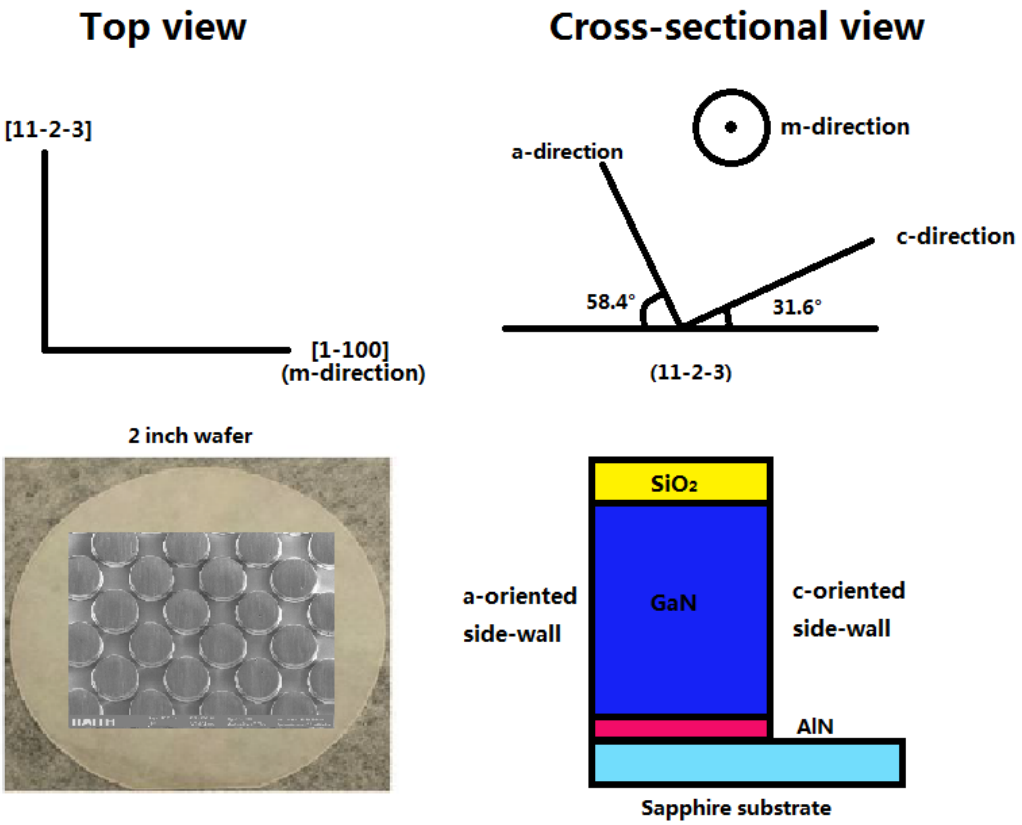

Figure 5.3 Bird-view SEM image of a micro-rod template and the geometric relationship between a micro-rod and its oriented sidewalls.

5.2.2 Morphology of the wet etching

Figure 5.4 shows some typical SEM images of the etched micro-rods, where 10% KOH solution is used and the etching time is kept to be 120 min in each case. Four SEM images are taken by rotating the sample by 0, 90, 180, and 270 degrees, respectively, in order to observe all facets. For Figure 5.4 (a), (b), (c) and (d),

c-oriented, m-oriented, a-oriented and m-oriented sidewalls are facing toward us, respectively.

In Figure 5.4 (b) and (d), it can be seen that the a-oriented side-walls are etched strongly, resulting in very rough side-walls and suspended SiO_2 on the top. In contract, the c-oriented side-walls are etched slightly, and the SiO_2 remains intact on the top of a micro-rod, indicating much slower etching rate along this direction. Such anisotropic etching rate can be attributed to different polarity.

It is worth pointing out that such an over-etched a-oriented side-wall can make overgrowth along this direction difficult, which is what we want as mentioned above. In addition, when GaN is laterally grown from the a-oriented side-walls, the suspended SiO_2 can effectively block GaN growth along the a-direction. It is also expected that such rough sidewalls could result in a reduced growth rate compared to that with smooth sidewalls.

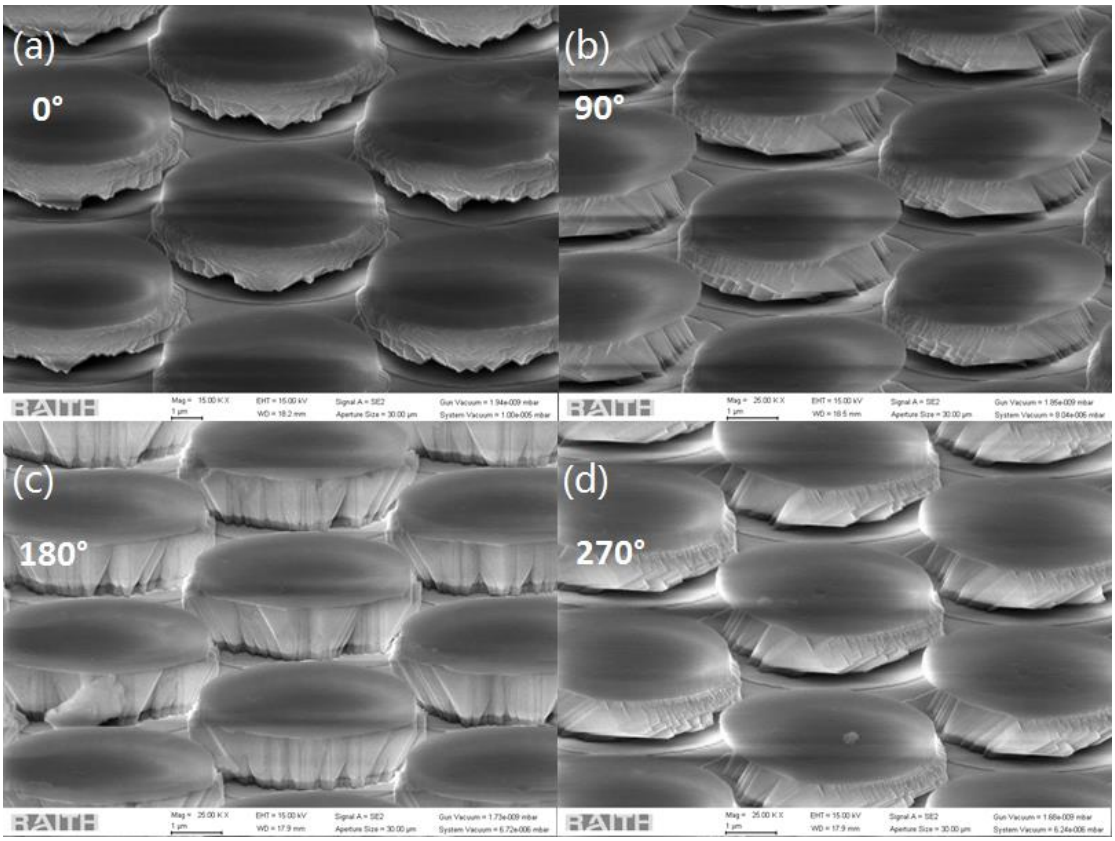

Figure 5.4 Bird-view SEM images of micro-rod templates after PAE KOH etching, taken from different angles

During the overgrowth process, lateral growth from the m-oriented sidewalls is

almost zero. Therefore, our investigation including discussion for this work is focused on comparing the growth along the a-oriented and c-oriented directions. Figure 5.5 (a) and (b) show typical cross-sectional SEM images of a GaN micro-rod before and after the PAE process, respectively.

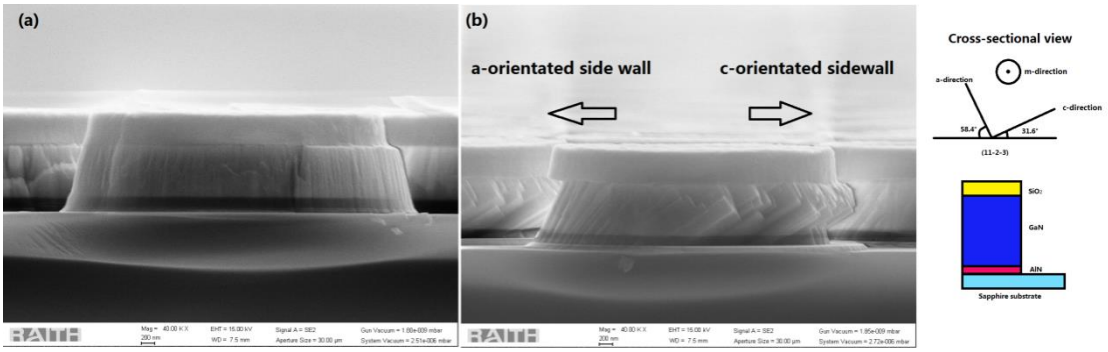

Figure 5.5 Cross-sectional SEM images of GaN micro-rod (a) before KOH etching and (b) after PAE etching.

In order to investigate the influence of UV illumination as one of the key roles for the PAE experiment on etching rate. Two semi-polar GaN micro-rod templates have been etched using 10% KOH solution for 60 mins, one under UV illumination and another without any UV illumination. As the etching temperature would be increased to 55°C under UV illumination, the sample without any UV illumination has been placed on a heater to keep the solution temperature at 55°C in order to exclude the influence of temperature.

Figure 5.6 shows the SEM cross-sectional images of both samples. The etching part with respect to the edge of the SiO_2 on the ***a***-oriented side is 234 nm for the sample under UV illumination, compared to 147 nm for the sample without any UV illumination. This confirms a faster etching rate in PAE. Furthermore, the c-oriented side-wall is slightly etched under UV illumination while nothing on the c-oriented side-wall has been etched without any UV illumination.

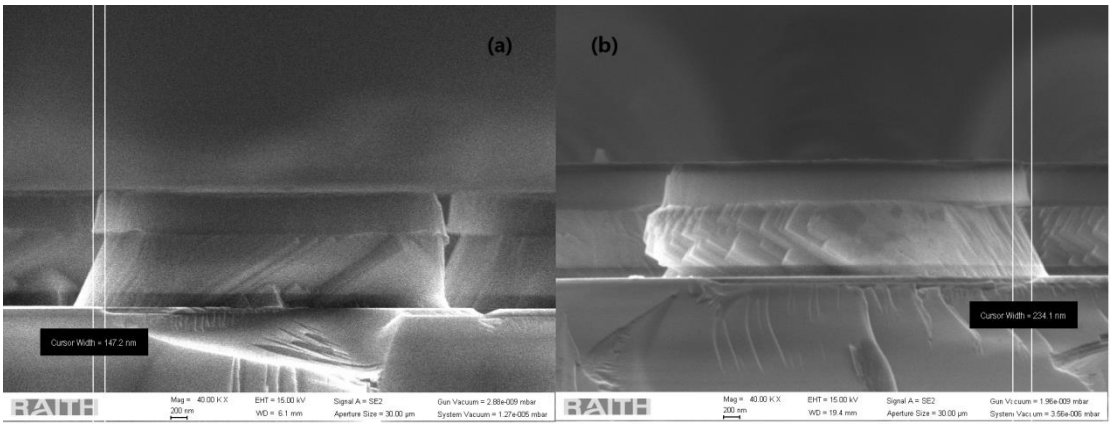

Figure 5.6 Cross-sectional SEM images of the GaN micro-rod after KOH etching (a) under UV illumination and (b) with any UV illumination.

Figure 5.7 shows detailed etching rates measured from different samples, demonstrating that the etching rate along a-orientation without any UV illumination is about 60% of that under UV illumination.

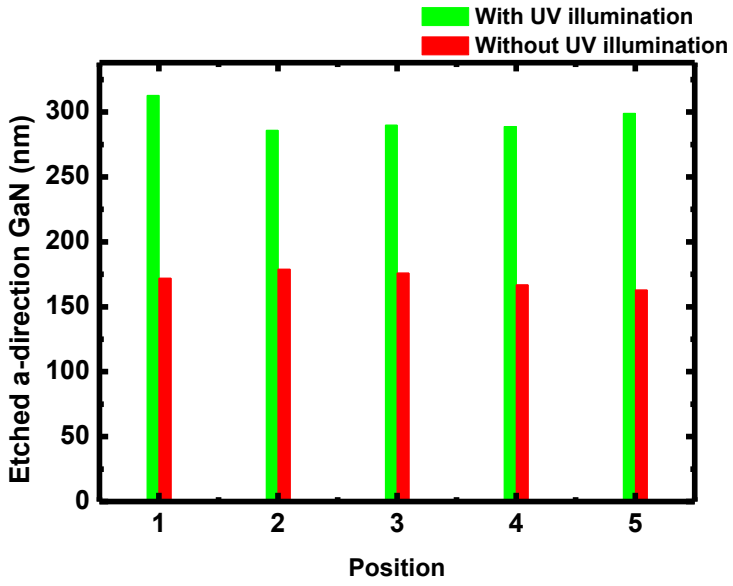

Figure 5.7 Length of the etched part of the GaN along a-direction with or without UV illumination.

5.2.3 Influence of the etching conditions on etching rate

Solution concentration

In order to study the Influence of the concentrations of KOH solution on etching

rate, the KOH concentration used is increased from 2% to 30% for our PAE experiments while all other conditions including template, UV source, solution volume and ICP etching conditions remain identical. The etching time is fixed at 60 mins.

Figure 5.8 (a)-(f) show SEM cross-sectional images of the GaN micro-rods after KOH etching using KOH concentration of 2%, 5%, 10%, 15%, 20% and 30%, respectively. For the a-oriented sidewall, the etching rate can be evaluated by examining the etching length with respect to the edge of the SiO_2 mask. The etching length increases from 133 nm to 240 nm, when the KOH concentration used is increased from 2% to 10%. However, under high KOH concentration (15% to 30%), there is no big difference in etching rate along this direction, as shown in Figure 5.8 (d) to (f).

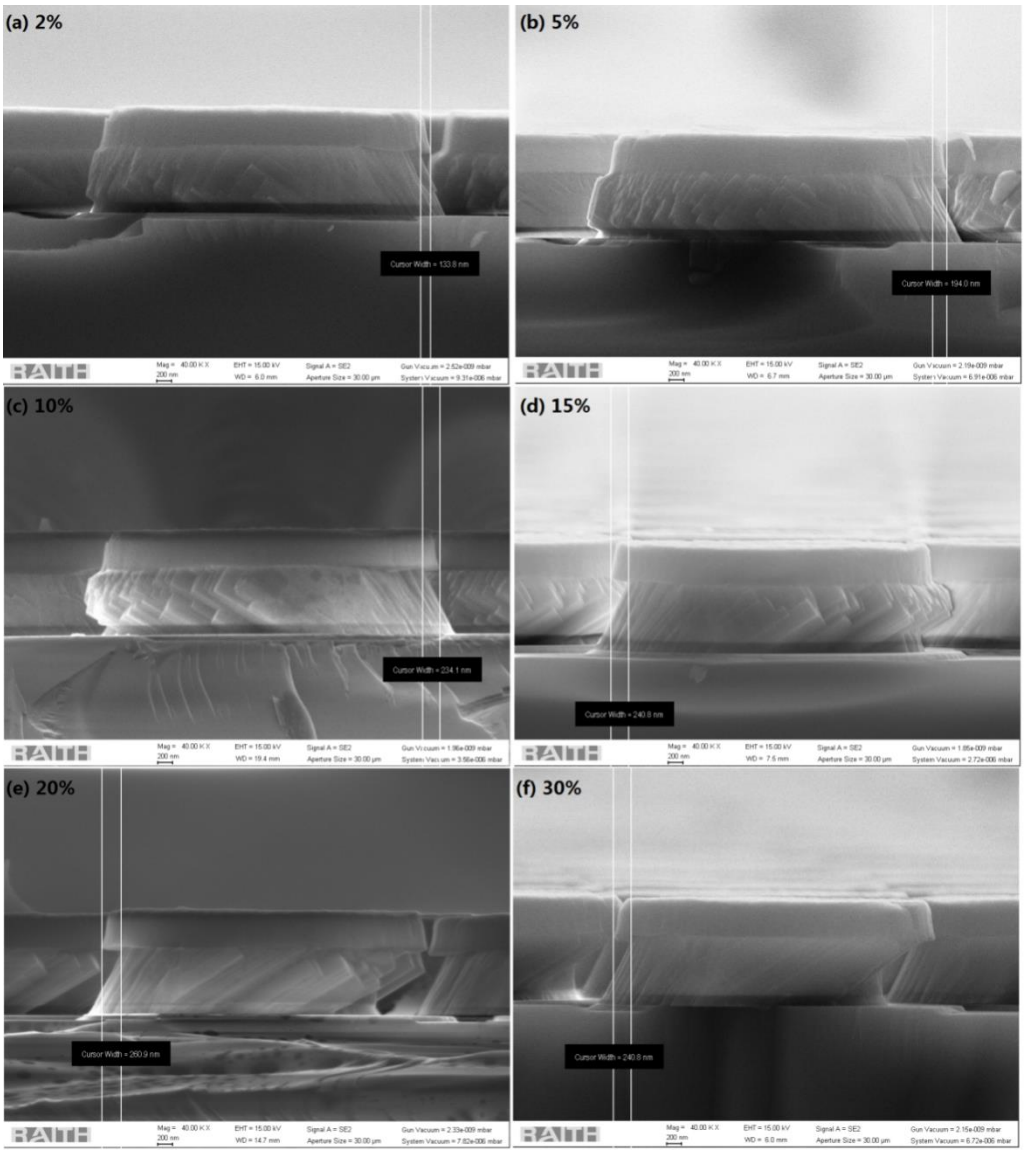

Figure 5.8 SEM images of a GaN micro-rod after wet etching by PAE using different KOH concentrations

In order to obtain an accurate etching rate along the ***a***-direction, the etching rate along this direction *l* is calculated by the following equation:

$$l = \frac{d}{sin58.4^\circ} \quad (5.1)$$

where *d* is the etching length along the horizontal direction as shown in Figure 5.9 and 58.4° is the angle of ***a***-direction with respect to the surface normal.

Figure 5.9 shows the etching length along the ***a***-direction as a function of the KOH concentration. It can be clearly observed that the etching rate along the ***a***-direction increases almost linearly with increasing concentration when the KOH concentration is below 10%. However, the etching rate remains almost unchanged

when the concentration is above 15%. The measurements have been performed for five times in order to confirm the reproducibility of the data.

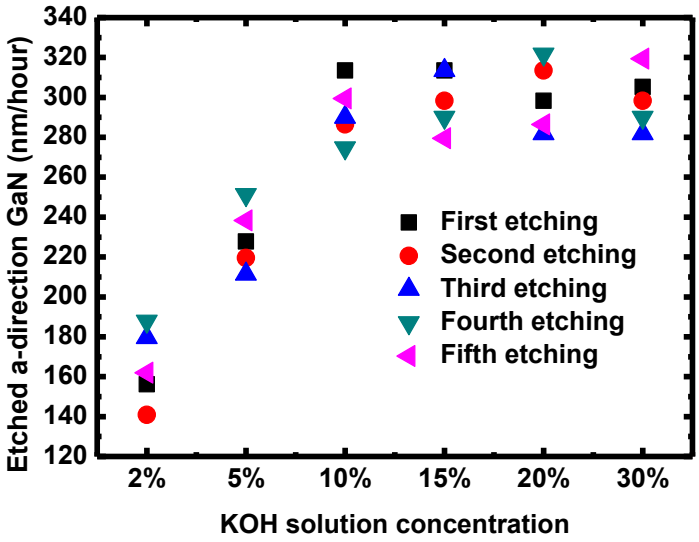

Figure 5.9 Etching rate along a-direction as a function of KOH solution

For the c-oriented side-walls, the GaN is almost not etched (or has a very slow etching rate) with low KOH concentration (2% to 5%), as shown in Figure 5.8 (a) and (b). With increasing the KOH concentration (10%-20%), the GaN at the bottom of micro-rods starts to be etched, forming inclined sidewalls with a tilting angle of ~32°, as shown in Figure 5.8 (c)-(e). Moreover, it can be seen that the inclined hexagonal features (c-facets) become more and more obvious by increasing the KOH concentration, indicating an enhancement in anisotropic etching. In contrast, when the concentration is up to 30% as shown in Figure 5.10 (f), there is no clear c-facet observed.

In order to carefully study the etching on c-oriented side-walls. Two zoom-in cross-sectional SEM images are taken on the samples etched using 5% and 10% KOH solution, respectively, as shown in Figure 5.10. The sidewall of c-oriented GaN is very smooth after 5% KOH etching while it becomes rough using 10% KOH, indicating a clear etching on c-plane GaN if the KOH concentration exceeds 10%.

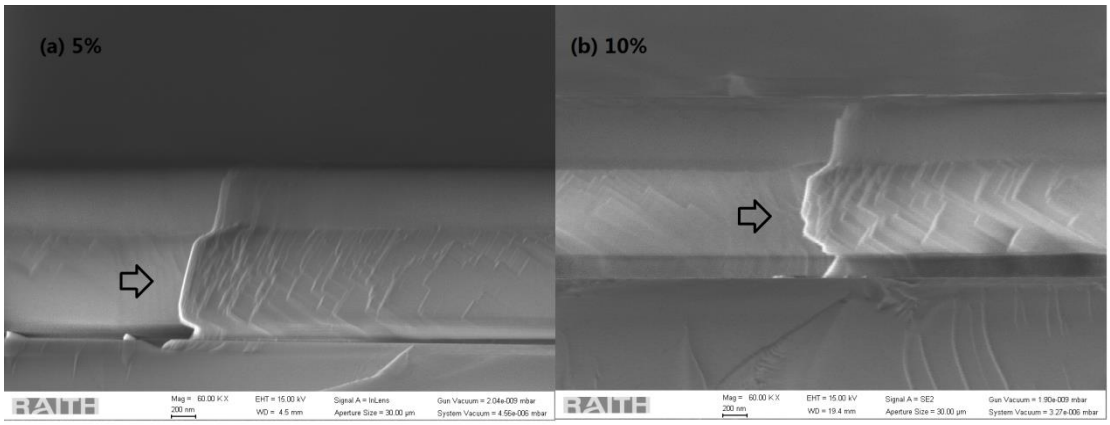

Figure 5.10 Zoom-in cross-sectional SEM images of c-orientated sidewall of GaN micro-rods after KOH etching using (a) 5% and (b) 10% concentration

On the other hand, as shown in Figure 5.9, a higher etching rate along a-direction has been achieved using 10% KOH solution. Since the sidewalls on both the ***c***-side and ***a***-side can be etched effectively, 10% KOH concentration is our optimized condition for our PAE process.

Etching time

One further condition which needs to be optimized is due to etching time. In this section, except that the etching time varies from 10 to 240 minutes the other etching conditions remain identical. The optimal 10% KOH solution is used.

The cross-sectional SEM images of two extreme cases are shown in Figure 5.11, where the etching time is 10 and 240 mins, respectively. When the PAE is performed for 10 mins, the c-plane facets of the GaN micro-rod can be clearly observed. This demonstrates that the PAE treatment using 10% KOH is effective even for a short etching time, and the sidewalls of micro-rods could be cleaned very well. After the PAE treatment is performed for 240 mins, both a-orientated and c-orientated GaN have been heavily etched, as shown in Figure 5.11 (b).

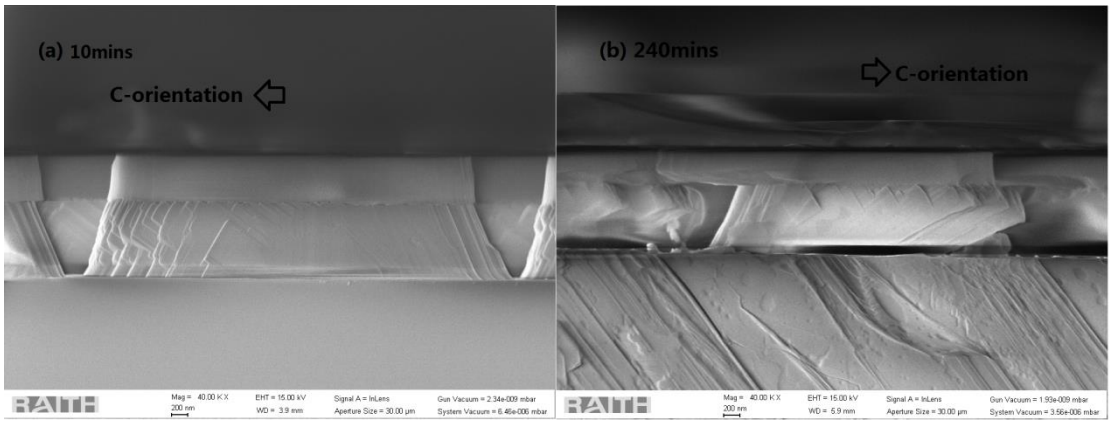

Figure 5.11 Cross-sectional SEM images of GaN micro-rod after KOH treatment for (a) 10 mins and (b) 240mins.

Figure 5.12 shows the length of etched part of GaN along a-direction as a function of etching time, where the slope represents the etching rate along the a-direction. It shows that the etching rate along this direction actually remains almost constant (nm/min) although the etching time varies.

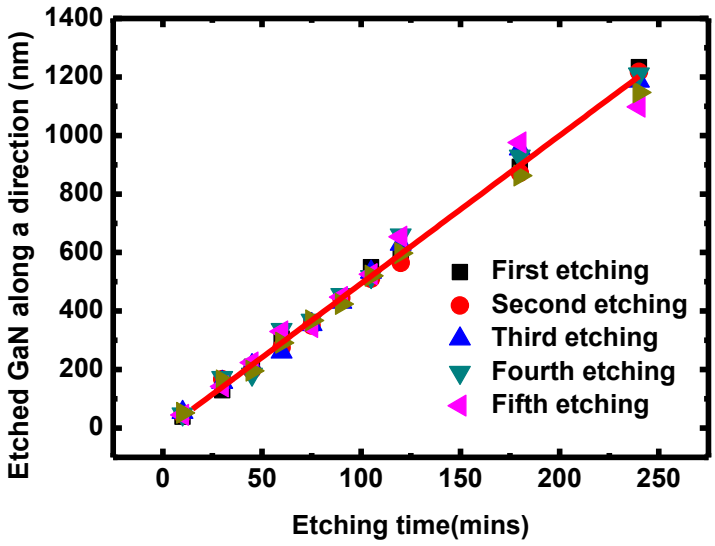

Figure 5.12 Length of etched part of GaN along a-direction as a function of etching time, the solid line is the linear fitting of etched part of GaN along a-direction

ICP over-etching

One of the major disadvantages of ICP dry-etching compared with wet etching is due to damage induced as a result of physical bombardment during the dry etching

process. This damage can be exacerbated by higher ICP power and longer etching time. Therefore, more severe damage can be generated under ICP over-etching processes. In this case, the subsequent wet etching rate can be affected.

One as-grown sample had been cleaved into two pieces before any ICP etching process. Our standard ICP etching process was performed on one piece for 8mins, while ICP etching with extra 5 mins (13mins in total) was performed on another piece. The other ICP etching conditions including etchants flow rates and ICP/RF power remain identical.

Figure 5.13 (a) and (b) show the cross sectional SEM images of the micro-rod before and after wet etching, respectively, where the micro-rod arrays are fabricated using our standard ICP etching conditions. In contrast, Figure 5.13 (c) and (d) show the cross sectional SEM images of the micro-rod before and after wet etching, respectively, where the ICP etching with extra 5 mins is used to fabricate the micro-rod arrays.

As shown in Figure 5.13 (a) and (c), two GaN micro-rods does not exhibit any obvious difference after the dry etching. However, after etching in 10% KOH solution for 60mins, the results are significantly different. As shown in Figure 5.13 (b) and (d), although the etching rates along the a-orientation are similar for both samples, c-oriented sidewalls show major difference for the two samples. Figure 5.13 (d) indicates that the micro-rod has been etched by about 2μm while Figure 5.15 (b) shows slight etching on the c-orientated sidewall. It indicates that the heavily physical damage caused as a result of ICP over-etching can strongly increase the wet etching rate along the c-orientation.

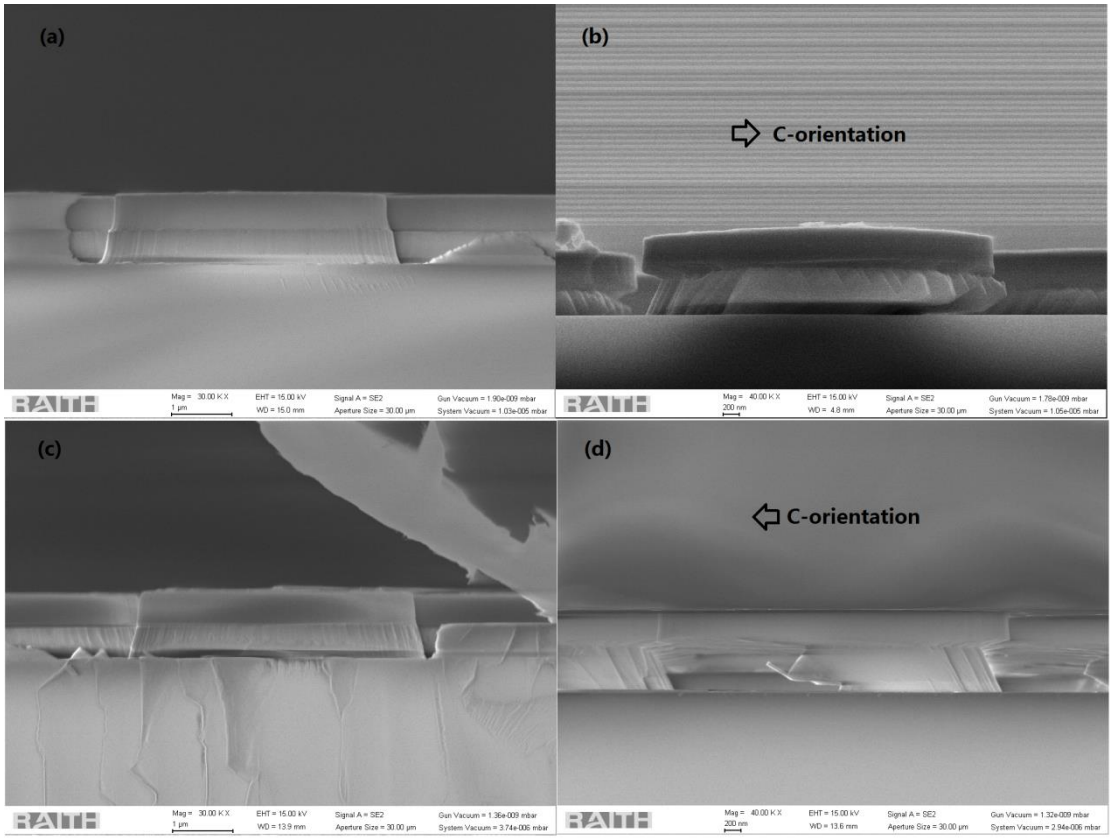

Figure 5.13 Cross-sectional SEM images of micro-rods (a) with regular ICP etching processes, (b) after the KOH treatment; the micro-rod with (c) extra 5mins ICP etching processes, and (d) after the KOH treatment.

5.3 Conclusion

The chemical etching treatment is very important as it can effectively remove any damage on the sidewalls of GaN micro-rod introduced as a result of ex-situ fabrication process, mainly due to ICP dry-etching.

UV illumination has been proved that it can effectively enhance the KOH etching rate on GaN. A series of PAE experiments have been carried out to investigate the KOH etching on GaN along different orientations under various etching and template conditions. The KOH solution with 10% concentration has been found to be optimized for our chemical treatment, which provides simultaneous high etching rate along the a-orientation sidewalls of micro-rod arrays and slight etching on their

c-oriented sidewalls. By using 10% KOH solution, the etching rate along the a-orientation remains almost constant when the etching time increases from 10 to 240 mins. The c-oriented sidewalls of GaN micro-rod arrays can be also etched even for a short time etching (10 mins). Furthermore, the wet etching rate is greatly affected by the ICP dry etching process. If the GaN micro-rods are over-etched during the ICP dry etching process, the etching rate along the c-orientation increases massively due to the sidewall damage induced by the dry etching, while the etching rate along the a-orientation is much less sensitive to the ICP over-etching.

Chapter 6 Stimulated emission from semi-polar (11-22) GaN on sapphire substrates by using micro-rod overgrowth technique

The last two decades have seen unprecedented progress in the field of III-nitride optoelectronics, but mainly limited to InGaN based LEDs and LDs in the blue spectral region. Very recently, a number of emerging technologies based on visible LDs have been developed, such as laser color display[134], smart-phones with pico-projectors, opto-genetics [135] and wireless communication [136], where long-wavelength green/yellow LDs are the key missing components. Growth of III-nitrides along a semi-polar direction, in particular the (11-22) orientation, would be a promising solution to achieve long wavelength LDs, as such an orientation is expected to lead to both reducing so-called QCSE and increasing indium incorporation efficiency in InGaN, which are the two fundamental limitations posed by current c-plane III-nitrides.[137] So far, all the III-nitride semi-/non- polar LDs reported have been exclusively achieved by means of growth on extremely expensive GaN substrates with a very limited size (typically $10\times10\ mm^2$).[138,139] These free-standing substrates are obtained by slicing a thick *c-plane* GaN layer grown on sapphire along a semi-/non- polar orientation[138,139], and such homo-epitaxial growth is therefore not very attractive to the optoelectronics industry in terms of mass production.

A practical way forward, which could address the two major challenges, is to grow long wavelength such as green and yellow LDs along the semi-polar (11-22) orientation on sapphire substrates.[137] However, the major issue is due to the unsatisfactory crystal quality of (11-22) semi-polar GaN grown on sapphire. Recently, our team has developed a semi-polar (11-22) GaN overgrowth approach based on regularly arrayed micro-rod templates on *m-plane* sapphire, leading to significant

improvement in crystal quality.[3,96] Our approach has demonstrated a number of major advantages compared with other technical routes.[119,140] For details, please refer to a topical review published very recently.[137] As a consequence, we have demonstrated (11-22) semi-polar InGaN LEDs from green to amber grown on such high quality semi-polar GaN templates.[3] However, a stimulated emission has never been achieved on any overgrown semi-polar GaN on sapphire.

In this Chapter, we have observed a stimulated emission optically pumped at room temperature on our semi-polar (11-22) GaN overgrown on regularly arrayed micro-rod templates with an optimized design on *m-plane* sapphire. Furthermore, a standard laser stripe-length dependent optical measurement has been performed in order to investigate optical gain characteristics, and an optical gain of 130 cm^{-1} has been measured. The results presented further validate the satisfactory crystal quality of our overgrown semi-polar (11-22) GaN on sapphire, representing a major step towards the development of III-nitride semi-polar LDs on sapphire.

6.1 Experiment detail

6.1.1 Template preparation and overgrowth

A 500nm thick semi-polar (11-22) GaN sample is grown on m-plane sapphire by MOCVD after a 50nm thick high temperature AlN buffer. The growth conditions are identical to those of the as-grown template used for the self-organized Ni nano-mask overgrowth approach introduced in Chapter 4.

The detailed fabrication procedure of the micro-rod array templates has been introduced can be found in one of the previous Ph.D. thesis in our group.[132] Eventually, a regularly-arrayed micro-rod template with the SiO_2 remaining on the top of each micro-rod is obtained. The bird-view SEM image of the micro-rod arrayed template is shown in Figure 6.1.

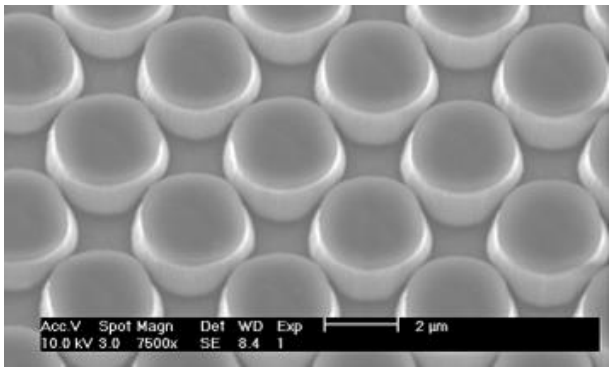

Figure 6.1 Bird-view SEM image of the template for overgrowth

We specifically chose an overgrown (11-22) GaN sample on a template with a micro-rod diameter of 4 µm, where the semi-polar GaN exhibits the lowest dislocation density but not the lowest density of basal stacking faults (BSFs).[133]

Subsequently, the semi-polar micro-rod GaN template undergoes the KOH chemical treatment discussed in Chapter 5, before any GaN overgrowth. Finally, a 4µm thick nominally undoped GaN layer is grown with a V/III ratio, a growth temperature and a pressure of 1600, 1120°C and 75torr, respectively.

6.1.2 Optical pumping set-up

A 266 nm diode pumped pulsed Nd: YAG laser with a pulse duration of 9 ns and a repetition frequency of 850 Hz is employed as an excitation source for the optical pumping measurements. Two cylindrical lenses are placed in front of the sample to focus the laser into a stripe-shaped beam incident on the surface of the sample, and the width and length of the laser beam are 0.2 and 1 mm, respectively. A motorized transition stage with an accuracy of 1 µm is employed to control the stripe length of the laser beam incident on the samples accurately. The emission is collected from the edge of the sample, and then detected by a high sensitivity CCD array detector. The stripe-length dependent optical pumping measurements have been carried out as a function of the laser stripe length from 0.3 to 0.9 mm. It has to be highlighted that the non-uniformity in laser beam due to the edge effect can be safely ignored, as a linear increase in emission intensity below the threshold for lasing has been found

with increasing the laser stripe length even in a small step. This can allow us to obtain an accurate optical gain. A schematic of an optical pumping system is shown in Figure 6.2.

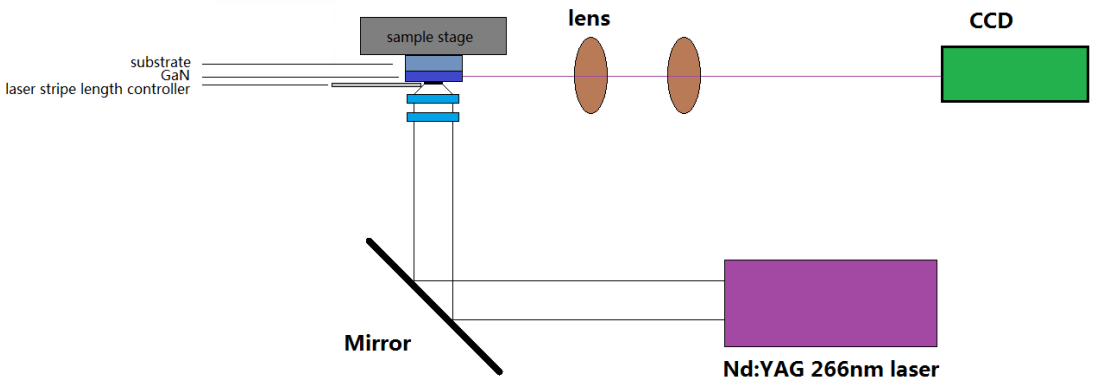

Figure 6.2 Schematic of our optical pumping system

6.2 Results and discussion

Figure 6.3 shows the emission spectra of the overgrown semi-polar GaN sample measured as a function of an optical pumping density from 130 to 1100 kW/cm^2. Under the low optical pumping densities, a broad emission peak at around 363 nm has been observed as expected, corresponding to the spontaneous near band edge emission (NBE) of the GaN sample. However, when the optical pumping power density increases, another peak on the long wavelength side at around 374 nm appears. With further increasing the optical pumping power density, this peak becomes narrower and stronger, indicating a stimulated emission process.

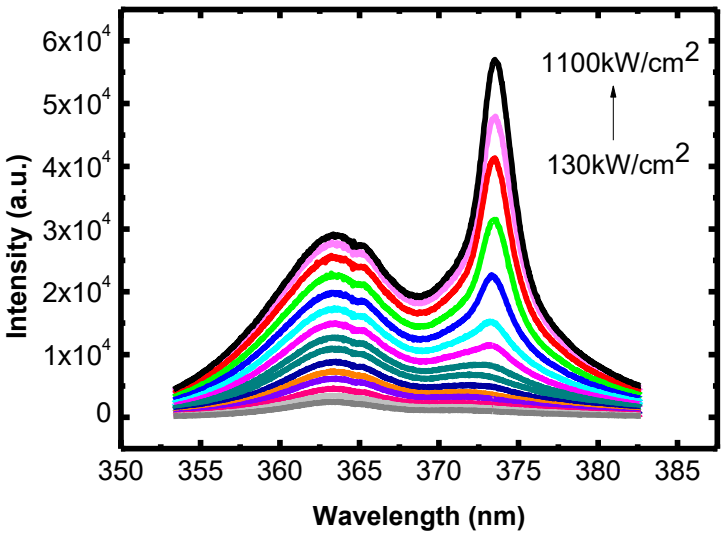

Figure 6.3 PL spectra of the semi-polar overgrown GaN versus optical pumping peak power density while the excitation length is kept to be 1mm.

Figure 6.4 shows both the integrated intensity and the line-width of the stimulated emission at 374 nm as a function of excitation power density. Under the low excitation power densities, the integrated intensity increases linearly with increasing excitation power density. A nonlinear increase in integrated intensity has been observed when the excitation power density exceeds 725kW/cm^2. Simultaneously, the line-width shows a dramatic reduction from around 7 to 3 nm. Both this super-linear increase in intensity and the reduction in line-width further confirm the stimulated emission, and the threshold for lasing optically pumped labeled as E_{th} can be estimated to be 725kW/cm^2. For comparison, optical pumping measurements have been performed on a standard *c-plane* GaN grown on (0001) sapphire under identical conditions, and a stimulated emission at around 374 nm has been observed. The Figure 6.5 presents the integrated intensity of the stimulated emission from the standard c-plane GaN grown on sapphire as a function of an excitation power density, showing a threshold of around 576kW/cm^2.

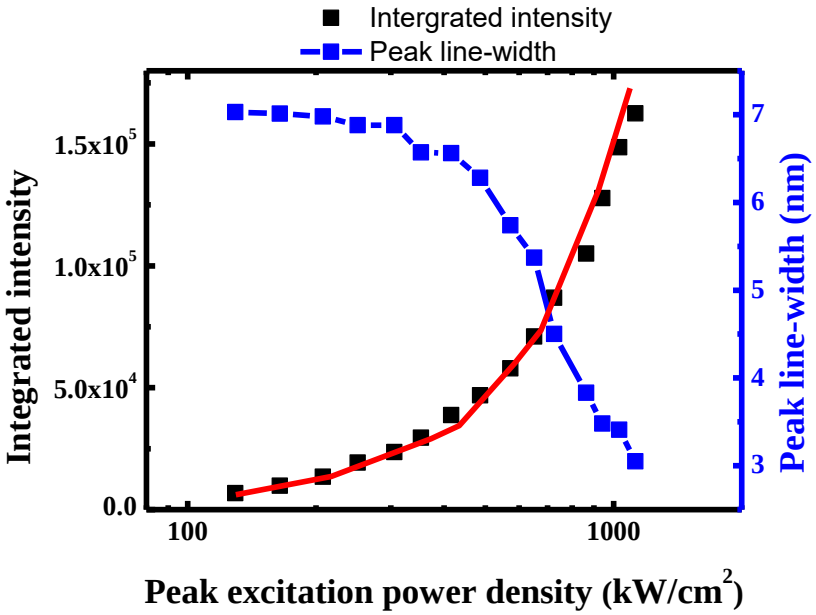

Figure 6.4 the integrated intensities and peak line-width versus peak excitation power densities, the red solid line is a guide line for eyes

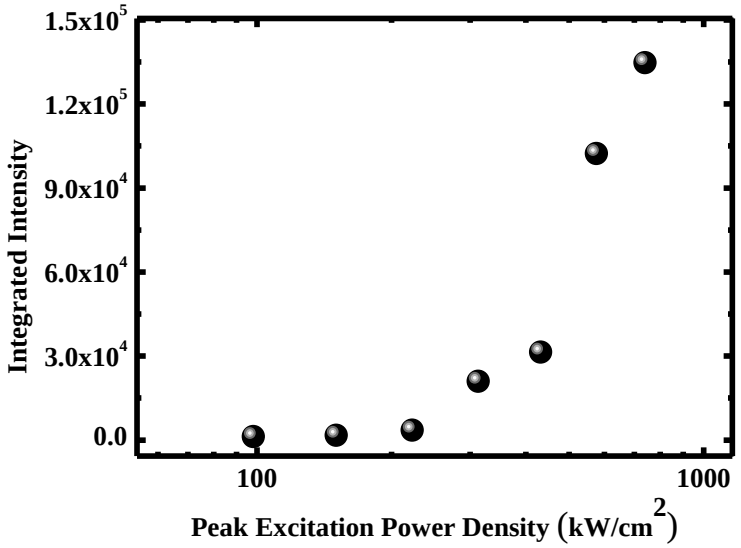

Figure 6.5 the integrated intensities versus peak excitation power densities for c-plane bulk GaN on sapphire

Other reports on *c-plane* GaN have also been listed in Table 6.1, where Amano[141] reported a stimulated emission at around 374 nm on *c-plane* GaN with a thickness of ~3.5μm grown on (0001) sapphire when an optical pumping density exceeds 0.7MW/cm^2. Stimulated emission for GaN grown on SiC[142] or bulk GaN[143] have also been reported. As revealed from Table 6.1, the E_{th} obtained for our

overgrown semi-polar (11-22) GaN (725kW/cm^2) is generally comparable to those for *c-plane* GaN, which should be attributed to the significantly improved material quality as a result of our overgrowth technology. It is worthwhile to highlight that the shift of the stimulated emission wavelength for our semi-polar GaN with increasing excitation power density is negligible, from 373.2nm at E_{th} to 373.4 nm at $1.56E_{th}$, demonstrating a great advantage compared with c-plane GaN in terms of wavelength stability.[141]

Ref.	E_{th} and G_{mod}	Structure
Amano[141]	0.7MW/cm^2	c- GaN (3.5μm):sapphire
A. S. Zubrilov[142]	3.4MW/cm^2	c- GaN (1μm):SiC
Shiro Sakai[143]	0.86MW/cm^2	c- GaN (0.6μm):GaN
Sheff	0.725MW/cm^2 130cm^{-1} along [1-100]	Bulk semipolar (11-22) GaN
	0.576MW/cm^2	Bulk c-GaN on sapphire

Table 6-1 Comparison of threshold excitation power density of optically pumped stimulated emission for semi-polar (11-22) and c-plane bulk GaN

Based on the overgrown (11-22) GaN sample with such high quality, standard stripe-length dependent optical-pumping measurements have been performed in order to measure its optical modal gain. Generally speaking, an optical modal gain can be quantitatively obtained using the well-known equation provided below.[144-146]

$$\mathrm{I}(L) = \frac{A}{g_{mod}} \times (e^{g_{mod} \times L} - 1) \quad (6.1)$$

where I is the emission intensity as a function of the laser stripe length incident on the sample tested; L is the laser stripe length incident on the sample; g_{mod} is optical modal gain and A is a constant. By changing the length of the laser beam stripe, g_{mod} can be calculated.

Figure 6.6 shows the typical amplified spontaneous emission (ASE) spectra recorded as a function of the laser stripe length incident on the sample from 0.3 to 0.9 mm with an increment step of 0.1 mm. When the laser stripe length incident on the sample is less than 0.7 mm, only a broad peak at 363 nm due to spontaneous emissions can be observed. When the laser strip length is increased up to 0.7 mm,

another peak on the long wavelength side at 374 nm appears. The peak becomes narrower and the emission intensity increases rapidly when the laser stripe length on the sample is further increased, a typical fingerprint for a stimulated emission. This can be clearly observed in Figure 6.7, the integrated intensity of the ASE as a function of the laser stripe length incident on the sample. The excitation power density remains constant (namely, above 725kW/cm^2) during the measurements.

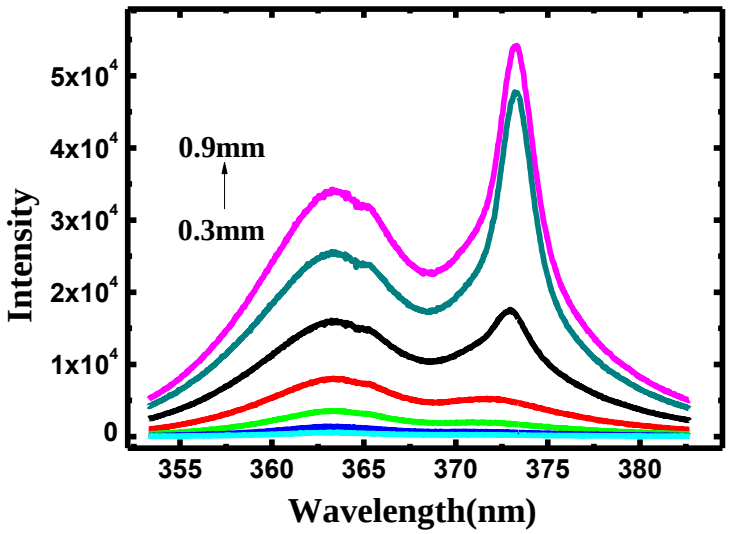

Figure 6.6 PL spectra of semi-polar overgrown GaN versus laser stripe length

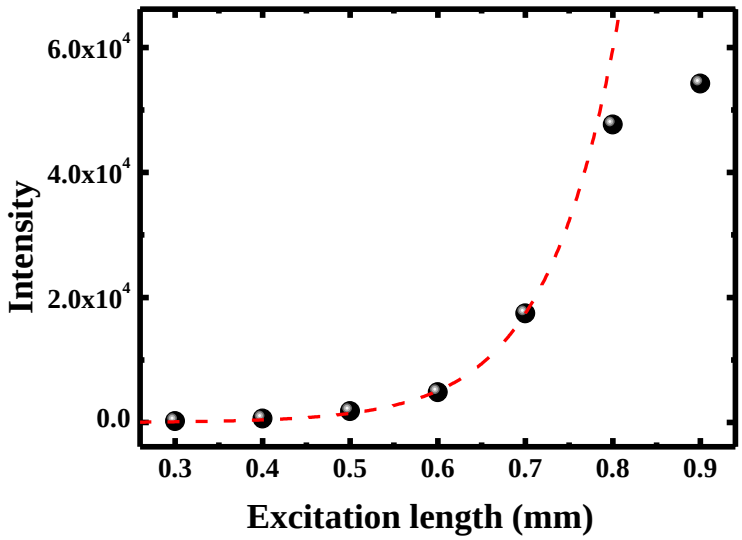

Figure 6.7 absolute intensity at the stimulated emission position versus the excitation length, the red dash line is fitting line based on the data points and equation 6.1

Figure 6.6 shows that the stimulated emission peak starts to appear when the laser stripe length on the sample is above 0.7 mm. Therefore, our optical gain is calculated based on the data with the laser stripe length on the sample is larger than 0.7 mm, namely, 0.8 mm. Figure 6.8 shows the gain spectra, exhibiting that the maximal net modal gain is around 130 cm^{-1} at ~374 nm.

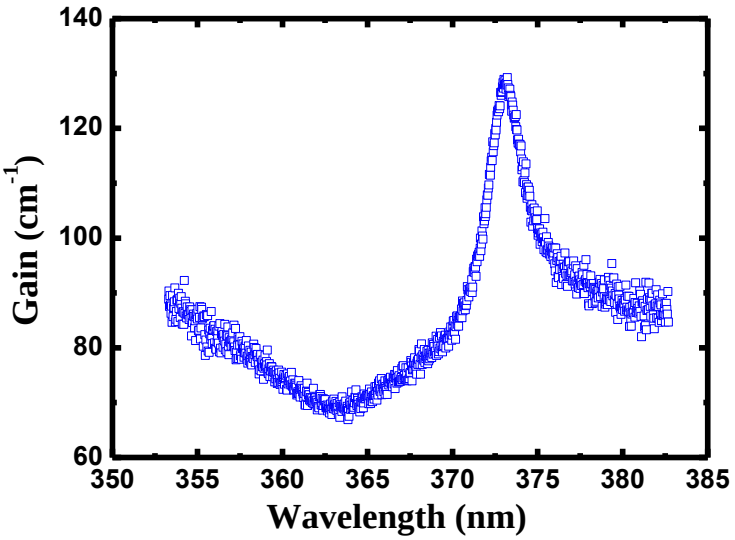

Figure 6.8 Typical gain spectrum measured on the semi-polar overgrown GaN sample, showing the maximal net modal gain of around 130 cm^{-1} at ~374 nm.

As stated above, our overgrowth approach has led to a significant reduction in dislocation density, which is crucial for obtaining a stimulated emission. Unlike *c-plane* GaN, there generally exist two kinds of defects, namely, dislocations and BSFs. A systematic micro-structural investigation has been carried out on a number of semi-polar (11-22) GaN samples achieved by our overgrowth on the regularly arrayed micro-rods with different micro-rod diameters, indicating that an increase in micro-rod diameter from 2 to 7 μm can effectively reduce both the dislocation density and the BSF density of the overgrown (11-22) GaN, but in different ways.[133] For example, a 4 μm micro diameter leads to the lowest dislocation density, typically below $2 \times 10^8/cm^2$ (i.e., the sample used for the present study) measured by detailed TEM measurements. The TEM data indicates that the crystal quality of our semi-polar GaN approaches or is even better than that of current standard *c-plane* GaN on sapphire. The bright field cross-sectional TEM image of the overgrown GaN layer is

shown in Figure 6.9. It is found that the significant defect reduction is attributed to the SiO_2 blocking and coalescence of laterally-grown GaN layers during the overgrowth.

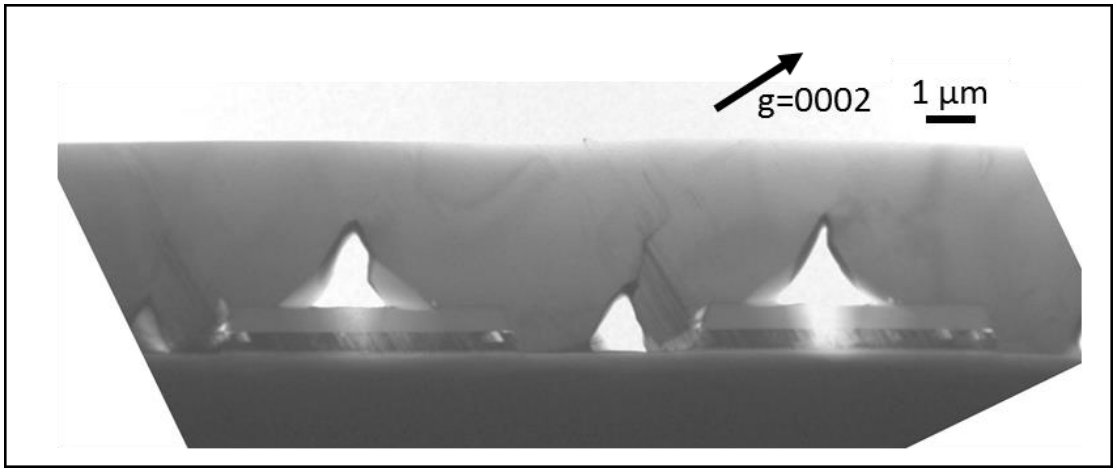

Figure 6.9 Bright field cross-sectional TEM images of overgrown GaN layer viewed along the [1-100] zone-axis under diffraction vector g=0002.

The TEM results are also in good agreement with detailed on-axis (11-22) XRD rocking curve measurements along the on-axis direction performed as a function of azimuth angle due to the anisotropy nature of semi-polar (11-22) GaN. The azimuth angle is defined as 0° when the projection of the x-ray beam onto the sample surface is parallel to the [10–10] direction, and 90° when the x-ray beam is parallel to the [11–23] direction. The FWHMs are typically 330 and 272 arcsec for the two directions, respectively.

Figure 6.10 shows the FWHMs of XRD rocking curves as a function of azimuth angles ranging from 0° to 180° for both overgrown and as-grown (11-22) GaN. The XRD FWHMs of the overgrown GaN are between 330 and 272 arcsec while those of the as-grown GaN are 1350 and 625 arcsec, meaning that the FWHMs have been significantly reduced by 1020 and 353 arcsec at 0° and 90° azimuth angles, respectively (the XRD rocking curve along (1-100) and (11-2-3) orientation of the overgrown sample is shown in Figure A.5 of appendix A). The significant reductions of FWHMs in XRD rocking curves demonstrate a step-change in crystal quality by using our micro-rod template overgrowth approach.

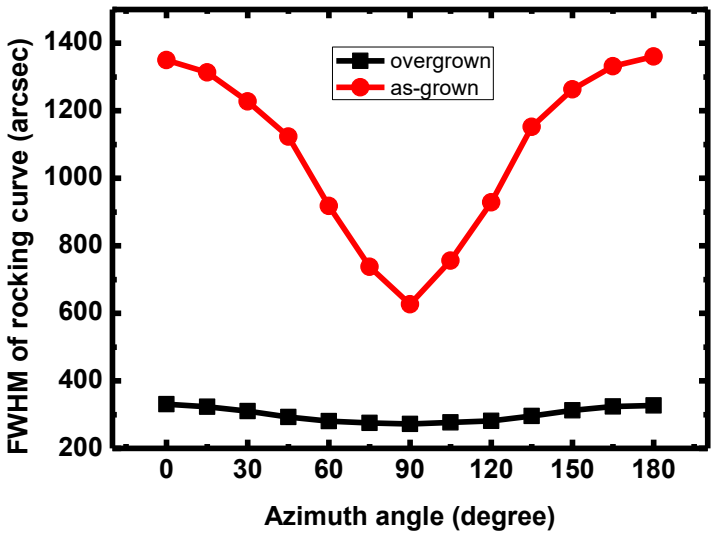

Figure 6.10 FWHMs of x-ray rocking curves for semi-polar as-grown and overgrown GaN

However, a 5 µm micro diameter instead of the 4 µm micro-rod diameter gives rise to the lowest BSF, but not the lowest dislocation density. So far, we have observed a stimulated emission on the sample grown on the regularly arrayed micro-rods with the 4 µm micro-rod diameter. Therefore, the high crystal quality of our overgrown semi-polar GaN, in particular the sample with a low dislocation density, is crucial for achieving the stimulated emission.

6.3 Conclusion

In summary, we have reported a simulated emission optically pumped at room temperature on our semi-polar (11-22) GaN overgrown on a micro-rod arrayed template with an optimized design on *m-plane* sapphire, which has never been reported previously on any semi-polar GaN grown on sapphire. This is attributed to the significantly improved crystal quality achieved by the overgrowth approach. Based on the high crystal quality sample, an optical gain of 130cm^{-1} has been measured by means of performing a standard laser stripe length dependent optical measurement. Both the threshold and the optical gain obtained are comparable to

those of the c-plane GaN grown on (0001) sapphire reported so far, implying that our cost-effective overgrowth approach paves the way for the development of semi-polar GaN based long wavelength LDs on sapphire substrates with a large size.

Chapter 7 (11-22) semi-polar InGaN emitters from green to amber on overgrown GaN on micro-rod templates

Long wavelength emitters such as green/yellow are crucial not only for the energy-saving solid state lighting, but also for increasingly demanding opto-genetics applications (especially yellow emitters). Semi-polar orientations, in particular, (11-22) orientation, offer a major advantage, meaning that the (11-22) semi-polar surface significantly favours indium incorporation into GaN due to its lower chemical potential than either polar or non-polar surface,[147] which is crucial for the development of green or even yellow emitters.

Some impressive results of InGaN-based semi-polar LEDs grown on sapphire or Si substrates have been reported,[148-151] which are, however, still limited to the blue and green spectral range. Yellow or even longer wavelength such as amber semi-polar LEDs with high device performance grown on foreign substrates has not yet been reported, as improvement in growth technologies including crystal quality and enhancing indium incorporation into GaN is requested.

Recently, our group has demonstrated a cost-effective overgrowth technique using a self-organized nano-mask approach, leading to a significantly improved crystal quality of (11–22) semi-polar GaN on m-plane sapphire.[37] The approach could reduce not only non-uniformity which is a typical issue for conventional ELOG but also coalescent thickness down to 1 μm significantly. Very recently, we demonstrate another even simpler approach for overgrowth of semi-polar GaN based on micro-rod array templates, where the diameter of micro-rods can be accurately controlled. The crystal quality of semi-polar GaN achieved using this approach has been further improved, leading to the demonstration of InGaN/GaN QW structures

with strong photoluminescence (PL) intensity in a spectral region of up to red.[152]

In this Chapter, we demonstrate a number of InGaN SQW LEDs overgrown on such (11-22) GaN templates, emitting strong green, yellow, yellow-green and amber emission with good electrical properties.

After many runs of test, the structures of those four LEDs have been finally designed which will be discussed in the experiment detail section. The number of QW pairs, the thickness and the In content of QW are crucial. Firstly, the number of QW is a trade-off between quantum confinement of the carriers and the crystal quality of the QW. On one hand, it is well known that increase the number of QW would increase the probability of confining carrier in the QW until they recombine to each other. On the other hand, dislocations are generated during the growth of InGaN due to the lattice mismatch between the QW and the barrier. All those dislocations act as non-radiative recombination centres. Secondly, the thickness and the In content of the QW will be another trade-off. Either increasing the QW thickness (due to QCSE) or increasing the In content of the QW can increase the emission wavelength. However, thicker QW leads to a stronger QCSE which is not preferred for a LED. Additionally, higher In content requires a lower growth temperature which results in significant worse crystal quality, while a higher In composition in the QW leads to larger lattice mismatch between the QW and the barrier.

7.1 Experiment details

7.1.1 Template preparation and LED growth

A single layer of (11-22) GaN subsequently fabricated into a micro-rod array template is grown on m-plane sapphire using our high temperature AlN buffer approach by MOCVD.[86]

The micro-rod masks with different diameters between 1.5 to 4 μm have been

employed for the fabrication of the micro-rod array template. Figure 7.1 shows a SEM image of our typical (11-22) GaN micro-rod template, with the SiO_2 layer remaining on top of micro-rods.

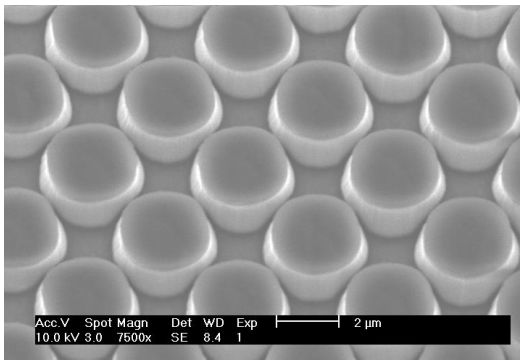

Figure 7.1 Bird-viewed SEM image of the template

The semi-polar GaN template with micro-rod arrays is subsequently reloaded into the MOCVD chamber for the overgrowth of GaN. The overgrown layer thickness is around 4 µm. The V/III ratio, temperature and pressure of the growth are 1600, 1120°C and 75torr, respectively.

Four InGaN SQW LED samples with different indium compositions were overgrown on such micro-rod templates by MOCVD. The growth temperature of the SQW in green, green-yellow, yellow and amber semi-polar LEDs is 766^{o}C, 762^{o}C, 760^{o}C and 756^{o}C, respectively. The thickness of the SQW is 3nm. The 8nm InGaN barrier is grown at 850^{o}C for the green, green-yellow and yellow LEDs. For the amber LED, in order to protect the SQW with very high In composition, the growth temperature is reduced to 840^{o}C. Then, a very thin GaN capping layer (about two molecular layers thick) is grown at the same temperature as the barrier layer. The growth pressure for the InGaN/InGaN SQW and the GaN capping layer is 250 torr. Finally, a 150nm thick Mg-doped *p*-type GaN layer is grown under 75 torr.

7.1.2 Device fabrication

Before any device fabrication process, p-type GaN activation is needed for our LED samples. This is generally performed by annealing the samples in nitrogen ambient using rapid thermal annealing (RTA). The normal activation temperature for

c-plane LEDs is 750-800°C, which will definitely damage the InGaN QWs in these samples since they were grown at a relatively lower temperature. Therefore, through optimization, all the semi-polar LED samples in this work are annealed at 650°C for 15min using RTA.

After the p-type activation, the samples can be fabricated into LED devices by standard photolithography and dry etching techniques. In order to make n-type contact on the n-type GaN layer, the samples need to be etched down to the n-GaN to expose part of the n-GaN. Mesa patterns with a size of 0.33×0.33 mm^2 are first transferred onto the surface of the LED samples by exposing under UV light and developing after spinning and baking photoresist. Subsequently, the patterned samples are etched using ICP, forming mesas with a depth of 700nm. The etching gases ware Cl_2 and Ar. The etching power is RF150W/ICP650W. Then, p-/n-type metal contacts are deposited one after another. Before deposition, patterns are formed. A film of 100 nm ITO is deposited on top of mesa (p-type GaN layer) by electron beam (E-beam) deposition, followed by a lift-off process using acetone. Then, the samples are annealed in air at 600°C for 1 min using RTA to form a transparent and ohmic *p*-type contact. A typical n-type contact, i.e., a Ti/Al/Ti/Au alloy with their thickness of 30/100/30/150nm, is deposited on the n-GaN using a thermal evaporator, followed by a lift-off process using acetone. Finally, a 30/200nm Ti/Au alloy is thermally deposited as pad electrodes on the top of both *p*-type and *n*-type contacts. After a lift-off process using acetone, (11-22) InGaN-based SQW LEDs are finally achieved. The LED structure is shown in Figure 7.2.

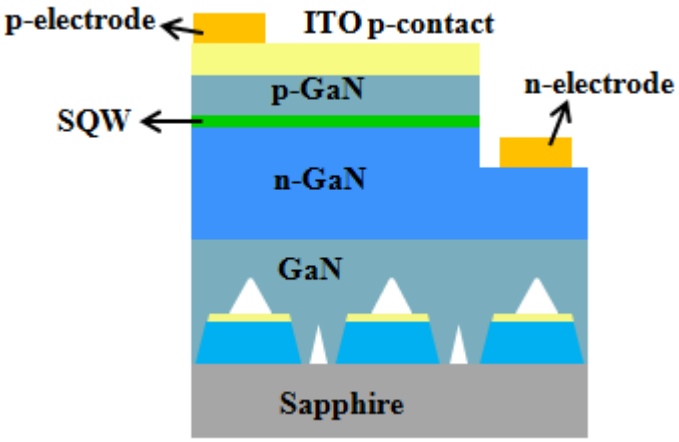

Figure 7.2 Schematic of the LED structure

7.2 Results and discussion

7.2.1 Crystal quality of (11-22) semi-polar overgrown GaN

The crystal quality is characterized by high resolution XRD measurement and TEM. Due to the anisotropy nature of semi-polar (11-22) GaN, standard x-ray rocking curve measurements along the on-axis direction are carried out as a function of azimuth angle. The azimuth angle is defined as 0°, where the projection of the x-ray beam onto the sample surface is parallel to the [10-10] direction, and 90° where the x-ray beam is parallel to the [11-2-3] direction.[153,154]

Figure 7.3 displays FWHMs of XRD rocking curves as a function of azimuth angle ranging from 0° to 180°, for both the overgrown (11-22) GaN and the as-grown (11-22) GaN before being fabricated into a micro-rod template. The XRD FWHMs for the as-grown GaN are 612 arcsec and 1370 arcsec at 0° and 90° azimuth angle, respectively, the typical values for a standard (11-22) GaN grown on sapphire. In remarkable contrast, the FWHMs of XRD for the overgrown (11-22) GaN are significantly reduced, with less than 360 arcsec and 252 arcsec at 0° and 90° azimuth angle, respectively. This demonstrates an excellent crystal quality of our (11-22) GaN, approaching the crystal quality of current *c*-plane GaN on sapphire for growth of

ultra-high brightness blue LEDs.

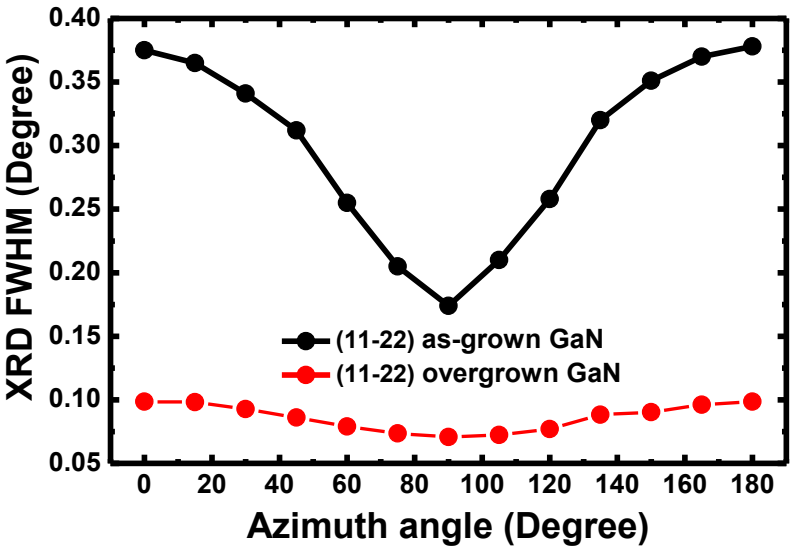

Figure 7.3 FWHM of rocking curve as a function of azimuth angle for semi-polar (11-22) as-grown and overgrown GaN.

It is worth mentioning that the overgrown (11-22) GaN has an excellent uniformity in crystal quality across a 2-inch wafer. The FWHMs of rocking curve at azimuth angle 0^{o} and 90^{o} across a 2-inch wafer are shown in Figure 7.4.

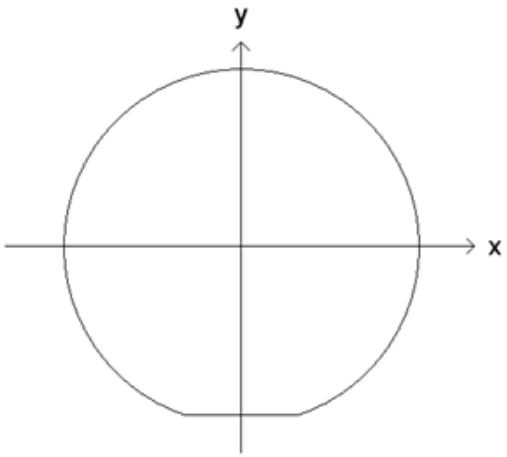

	Coordinate (X,Y) (mm)	FWHM at 0° (arcsec)	FWHM at 90° (arcsec)
Centre	(0,0)	360	250
Top	(0,10)	364	252
Bottom	(0,-10)	360	251
Right	(10,0)	367	256
Left	(-10,0)	362	254

Figure 7.4 FWHMs of XRD rocking curves measured at 0° and 90° azimuth angle across a 2 inch wafer

The cross-sectional TEM image as shown in Figure 7.5 demonstrates that the defects in the overgrown GaN are significantly reduced compared to the GaN micro-rods as a result of the SiO_2 blocking and coalescence processes during the overgrowth. Detailed TEM measurements indicate a dislocation density ranging from 1 to $4\times10^8/cm^2$ and a BSF density of 1 to $4\times10^4/cm$, respectively.[133]

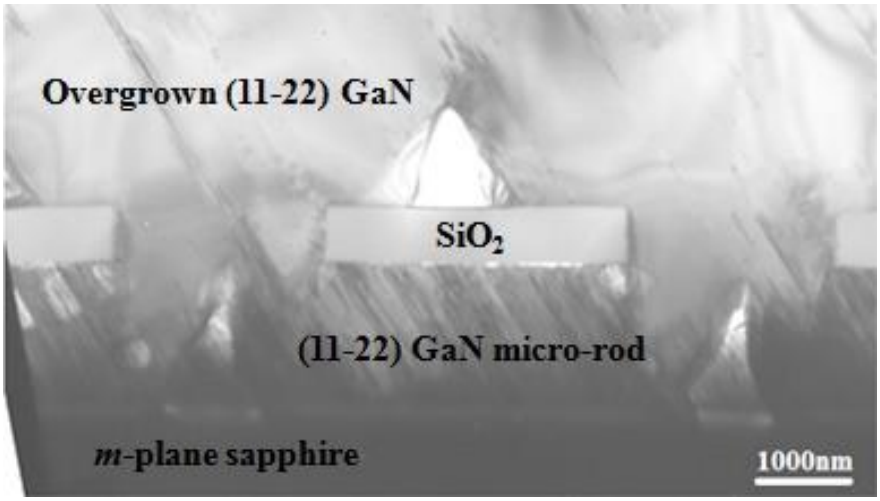

Figure 7.5 Cross-sectional TEM image of the semi-polar overgrown GaN

7.2.2 Device performance

All the electroluminescence (EL) measurements were carried out on bare-chip devices at room temperature in a continuous wave (cw) mode, using a LCS-100-UV characterization system equipped with a CCD APRAR spectrometer.

EL measurements have been performed on all these LEDs in a cw mode under injection current of up to 100 mA. Figure 7.6 shows a series of EL images for the four LEDs, each taken at 5, 20, 100 mA, respectively, demonstrating bright emissions in green, yellow-green, yellow and amber spectra regions, respectively.

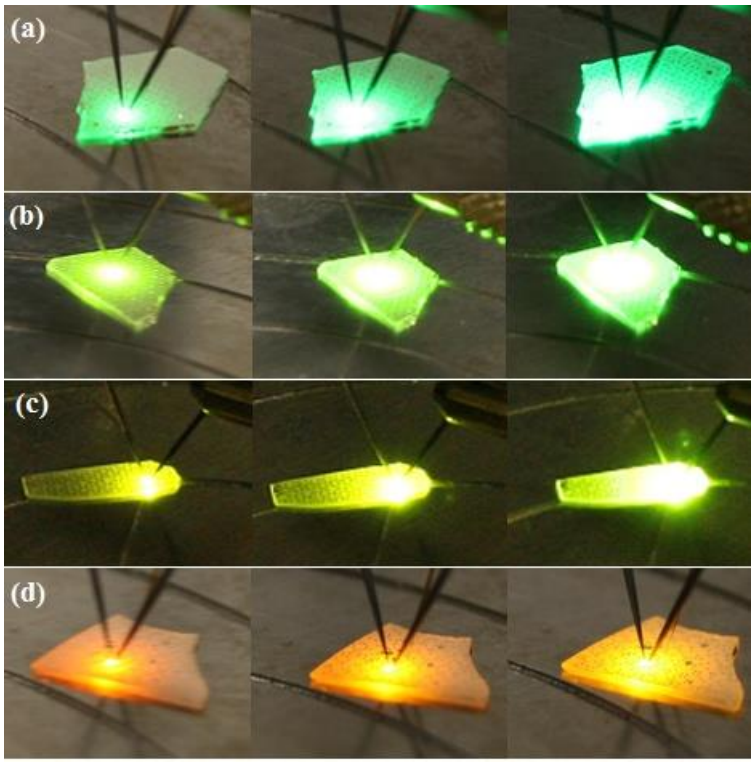

Figure 7.6 EL Emission photos of (a) green, (b) yellow-green, (c) yellow, and (d) amber LEDs, taken at 5, 20, and 100 mA, respectively.

Figure 7.7 shows the EL spectra of the four LEDs at different driving currents. The green, yellow-green and yellow LEDs all show a strong EL peak. An extra shoulder peak of the amber LEDs has been observed at 630 nm in addition to a main peak at 600 nm. It has been observed that the line-width of the EL spectra becomes broader as the emission light of LEDs moves towards long wavelength, indicating that higher indium composition leads to more significant indium segregation.

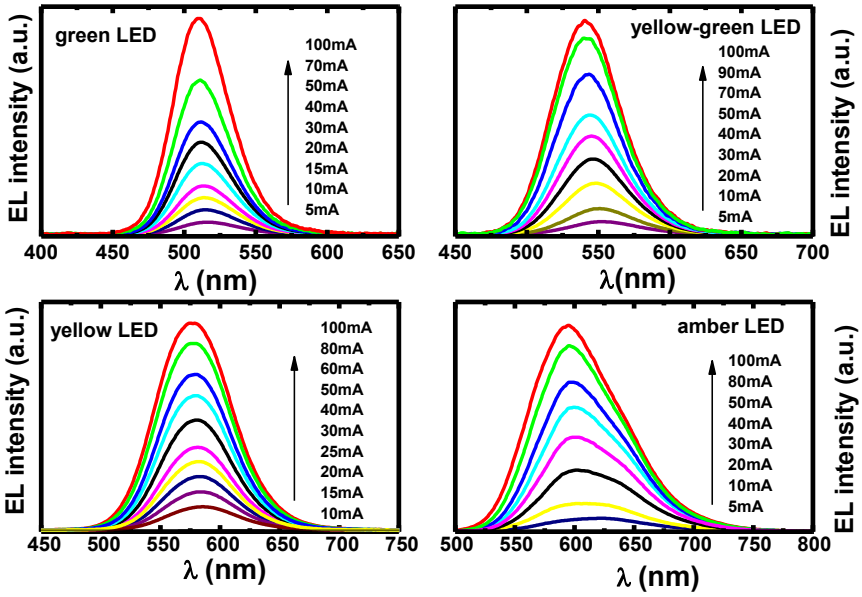

Figure 7.7 EL spectra of the four semi-polar LEDs measured at different injection currents.

The detailed peak wavelengths of the four LEDs are displayed in Figure 7.8, demonstrating a blue shift of the wavelength with increasing injection current from 1 mA to 100 mA. For the green (11-22) LED, the shift is only 8 nm. The blue-shift slightly increases to 15 nm and 19 nm for the yellow-green and yellow LEDs, respectively. For comparison, the blue-shift of a green LED on *c*-plane is typically about 13 nm.[155] This suggests that the QCSEs in our (11-22) LEDs are effectively suppressed. For the amber LED, there exists a fairly strong blue-shift in peak wavelength at low injection current. Our con-focal photo-luminescence measurements (not shown here) indicate that there exists very strong indium localisation effect in the amber LED as a result of very high indium content.[156] The shoulder peak of the amber LED could originate from significant indium segregation induced localized states. When increasing injection current, the carriers first occupy low-energy localized states, for example, at 630 nm, and then higher energy states. Therefore, part of the blue-shift at low injection current could be due to the carrier filling of low-energy localized potentials.

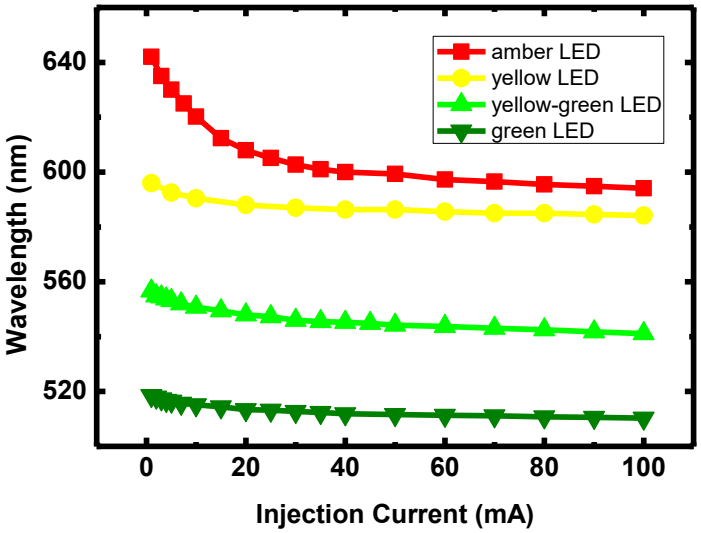

Figure 7.8 Peak wavelength of the four LEDs as a function of injection current

Figure 7.9 shows the typical current–voltage curves for all the four LEDs, also plotted in a logarithmic scale in an inset. It displays a standard behaviour of InGaN/GaN based LEDs with a typical turn-on voltage of 3.0-3.4 V at 20 mA injection current for the green, yellow-green and yellow LEDs, which are comparable to *c*-plane InGaN-based LEDs. For the amber LED, the voltage at 20 mA is relatively higher which indicates a higher series resistance of the amber LED device. This is very likely related to the p-type GaN which has to be grown at a lower temperature than those of other samples in order to eliminate any damage to the InGaN SQW with the highest indium content. In addition, due to very high In content in the InGaN SQW, the lattice mismatch between the QW and the barrier is large, thus dislocations are generated and penetrate to the surface of the device which would also increase the series resistance.

Higher series resistance makes a LED less efficient, because more electrical power transforms into thermal energy rather than optical emission. In order to achieve a more efficient device with similar emission wavelength, the device structure or the In content in the InGaN SQW needs to be further optimised.

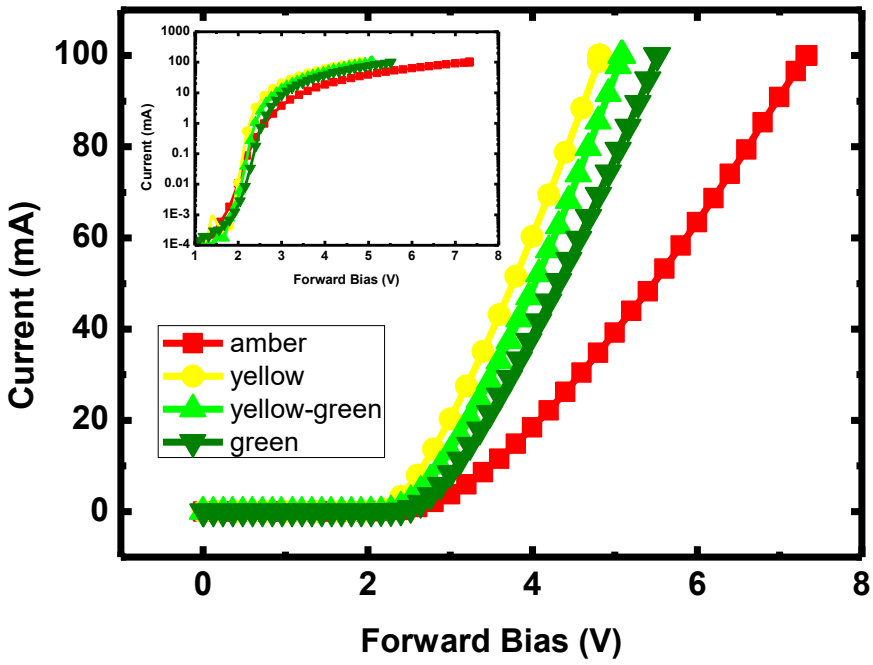

Figure 7.9 Current-voltage characteristics of the four semi-polar LEDs, the inset shows a semi-log scale.

Light output vs current (L-I) characteristics has been performed through measuring integrated EL intensity as a function of injection current, and the EQE has been assessed as a function of current as well. Figure 7.10 (a) and (b) shows light output (integrated EL intensity) and normalised EQE of the four LEDs as a function of injection current, respectively. With increasing the current from 1mA to 100 mA, the light output increases lineally without a saturation tendency for the green and yellow-green LEDs; whereas a weak saturation is observed for the yellow and amber LEDs. Furthermore, for all the four LEDs, the EQE initially increases with increasing injection current, and then reaches a maximum at 10-20 mA, followed by a slow reduction with further increasing injection current. In detail, the EQE at 100 mA drops down to 87%, 80%, 79% and 69% of the maximum for the green, yellow-green, yellow and amber LEDs, respectively. As a reference, the EQE of a *c*-plane green LED fabricated based on commercial LED wafers is also shown in Figure 7.10 (b) by one dashed line. In contrast, it starts to decrease from a very low current (~3 mA) and then drops down to 49% of the maximum at 100 mA. It suggests that the

efficiency-droop issue could be potentially reduced through growth and fabrication of (11-22) semi-polar LEDs.

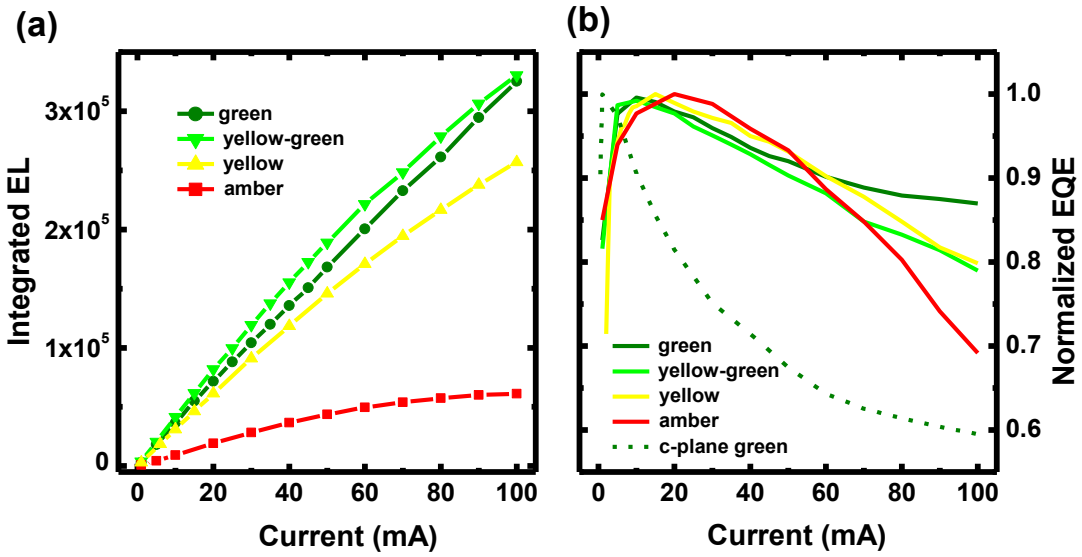

Figure 7.10 Light output (a) and normalized EQE (b) of the four LEDs as a function of current from 1 mA to 100 mA, a commercial c-plane green LED (dashed line) is measured as a reference.

Since semi-polar InGaN QWs emit polarized light owing to the low in-plane crystal symmetry, polarized EL spectra have been measured on the (11-22) LEDs to assess the polarization ratio by rotating a polarizer positioned between the device and a spectrometer. It was confirmed that the *c*-plane LEDs have negligible polarization characteristics by using this system. Polarization ratio ρ is defined as $(I_m - I_c)/(I_m + I_c)$, where I_m and I_c represent the integrated EL intensities parallel to the [1-100] and [11-23] directions, respectively. ρ has been estimated to be about 0.25 for our semi-polar LEDs. Considering that light scattering in any standard planar LED will lead to a significant reduction in the optical polarization,[157,158] the assessed polarization ratio is highly likely underestimated.

7.3 Conclusion

In summary, we have demonstrated semi-polar (11-22) InGaN LEDs with a wide spectral region of up to amber on our semi-polar GaN templates with significantly improved crystal quality, which highlight major advantages of semi-polar LEDs compared with current c-plane LEDs in terms of reducing efficiency droop and resolving the "green and yellow" gap issues. A significant reduction on injection current induced blue-shift has been achieved, compared with c-plane LEDs, indicating that the QCSEs which is a typical issue on c-plane LEDs has been effectively suppressed. The preliminary results suggest that our overgrowth technology is a potentially cost-effective approach to achieving semi-polar GaN emitters with high performance in a long wavelength region.

Chapter 8 Summary and Future Work

8.1 Summary

A systematic study has been performed on overgrown semi-polar GaN layers obtained using our self-organized Ni nano-rod templates with different nano-rod diameters in order to investigate the influences of the nano-rod diameter on crystal quality, strain, wafer bowing, and electrical properties of the overgrown layers. With increasing the nano-rod diameter, the crystal quality is greatly improved. Specifically, when the nano-rod diameter increases from 300 to 827 nm, the FWHMs of on-axis (11-22) XRD rocking curves measured along the (1-100) and (11-2-3) directions have been dropped down to 0.1528° and 0.1048°, respectively. Tensile strain reduces from 0.001 to 0.00016 and the wafer bowing reduces from 2980 to 638 km^{-1}. Furthermore, the room temperature electron mobility of up to 228 $cmV^{-1}s^{-1}$ has been achieved.

A KOH chemical treatment plays an important role in the surface cleaning of the templates prior to the subsequent overgrowth, as it can effectively remove the damages induced during the ICP dry-etching process. A systematic study of PAE processes by using a KOH solution on GaN nano or micro rod arrayed templates has been carried out. The etching rates along different orientations have been investigated under a number of etching and template conditions. A 10% KOH has been found to be optimal for the chemical treatment, providing a maximal etching rate along the “a” orientation and slightly etching the “c” orientated sidewalls simultaneously. Moreover, with such a 10% KOH solution, even for a short etching time (10mins), the c-oriented sidewalls of the GaN micro-rods are clearly etched.

Compared with the self-organized Ni nano-rod templates, the regularly arrayed micro-rod templates have demonstrated a number of major advantages in terms of reproducibility and further improving crystal quality. The FWHMs of x-ray rocking curves have been further reduced down to 330 and 272 arcsec at 0° and 90° azimuth

angle, respectively, meaning that the crystal quality has approached or even better than that of current standard c-plane GaN grown on sapphire. Stimulated emission from our overgrown semi-polar GaN has been successfully achieved. A maximal optical gain of 130cm^{-1} has been measured at room temperature by means of stripe-dependent optical pumping measurements.

A series of semi-polar (11-22) InGaN SQW LEDs with a wide spectral range of up to amber have been grown on our semi-polar GaN templates with significantly improved crystal quality, demonstrating excellent optical performance. These LEDs have exhibited reduced efficiency droop, significantly reduced QCSE, and significantly enhanced indium incorporation rate into GaN, greatly contributing to resolve the "green and yellow" gap issues. The results also indicate that our overgrowth technology is a very promising approach to achieving semi-polar GaN emitters with high performance in the long wavelength spectrum region.

8.2 Future Work

High crystal quality of overgrown semi-polar GaN with a low defect density is the key to realize high efficiency semi-polar GaN based LEDs which cover the whole visible spectral region. Therefore, in future, it is necessary to further investigate the influence of chemical wet-etching treatment on defect reduction. Simulations concerned about shape, height, diameter, spacing, growth rates along different direction of micro-rods and TEM measurements would be powerful tools to further understand the defect reduction mechanism of the overgrown semi-polar GaN.

One of the major challenges towards achieving longer wavelength stimulated emission from semi-polar InGaN QWs grown on sapphire is that the optical gain is still too low. This is due to the broad emission line-width which results from the strong indium inhomogeneity. The QW growth conditions needed to be optimized, aiming to suppress the indium inhomogeneity.

As progress has been made in high efficiency (11-22) semi-polar InGaN-based

LED from green to amber by using our overgrowth technique, white LEDs with an improved color quality is the next research objective. Development of high efficiency semi-polar InGaN based dual color LEDs can be an initial step.

Appendix A

Some of the XRD rocking curve which are mentioned in Chapter 4 and 6 are shown below.

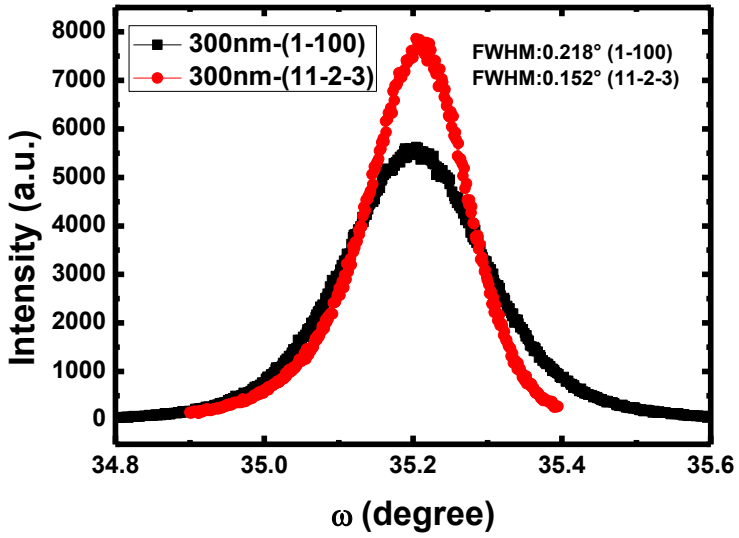

Figure A.1 XRD rocking curve along (1-100) and (11-2-3) orientation of semi-polar (11-22) GaN overgrown on template with 300nm diameter nanorod. These FWHMs is presented in Figure 4.6.

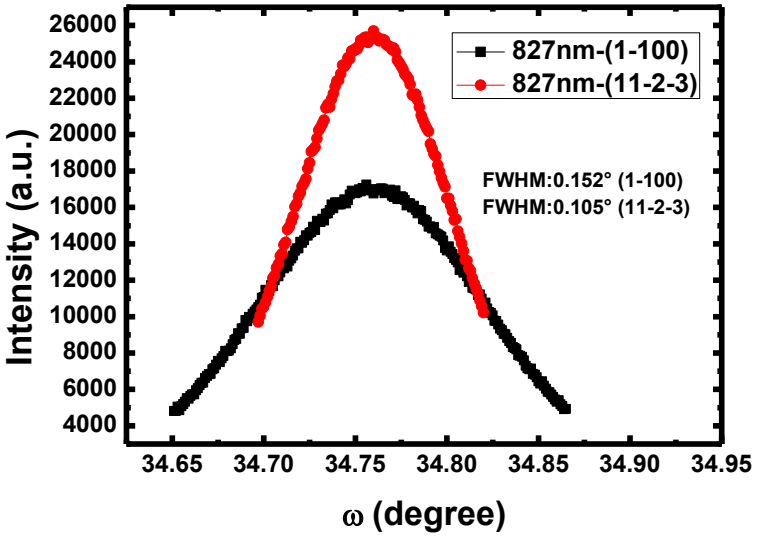

Figure A.2 XRD rocking curve along (1-100) and (11-2-3) orientation of semi-polar (11-22) GaN overgrown on template with 827nm diameter nanorod. These FWHMs is presented in Figure 4.6 and 4.15.

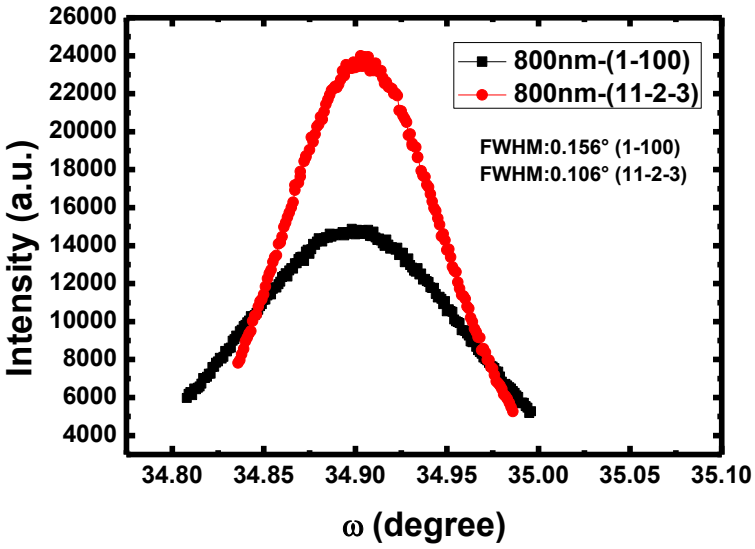

Figure A.3 XRD rocking curve along (1-100) and (11-2-3) orientation of semi-polar (11-22) GaN overgrown on template with 800nm diameter nanorod. These FWHMs is presented in Figure 4.7.

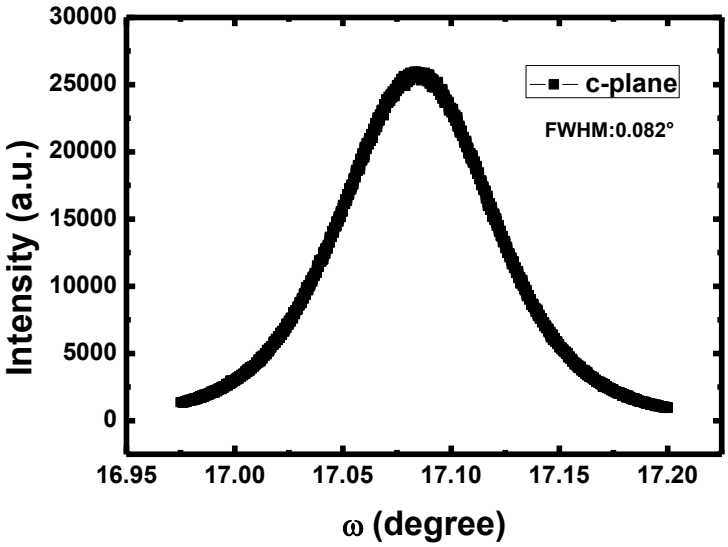

Figure A.4 XRD rocking curve data of c-plane GaN. This FWHM is presented in Figure 4.15.

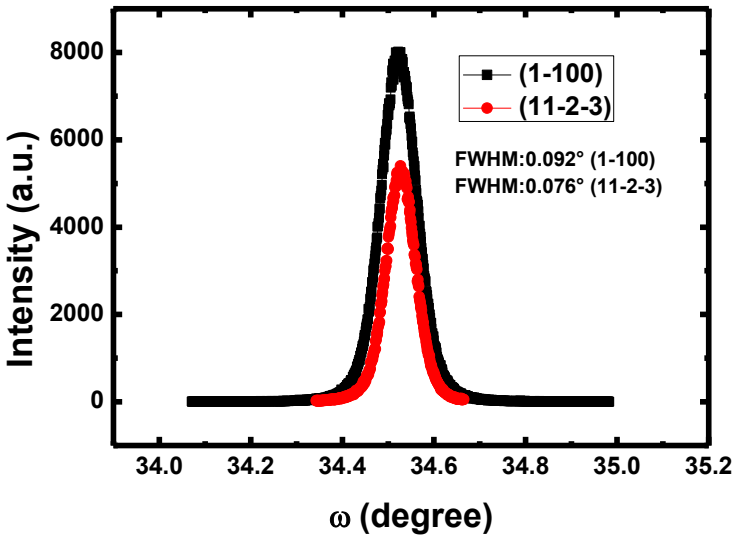

Figure A.5 XRD rocking curve along (1-100) and (11-2-3) orientation of semi-polar (11-22) overgrown sample which stimulated emission is obtained. These FWHMs is presented in Figure 6.10.

Reference:

[1]S. Nakamura, M. Senoh, and T. Mukai, *Jpn. J. Appl. Phys.* **32**, 8 (1993)

[2]Y. Taniyasu, M. Kasu and T. Makimoto, *Nature* **411**, 325 (2006)

[3]J.Bai, B.Xu, F. G. Guzman, K. Xing, Y. Gong, Y. Hou, and T. Wang, *Appl. Phys. Lett.* **107**, 261103 (2015)

[4] R. Juza and H. Hahn, *Zeitschriftfüranorganische und allgemeineChemie.* **239**, 282–287 (1938)

[5]H. P. Maruska and J. J. Tietjen, *Appl. Phys. Lett.* **15**, 327–329 (1969)

[6]H. Amano, N. Sawaki, I. Akasaki, and Y. Toyoda, *Appl. Phys. Lett.* **48**, 355 (1986)

[7]S. Nakamura, *Jpn. J. Appl. Phys.* **30**, 1620 (1991)

[8]H. P. Maruska, W. C. Rhines, D. A. Stevenson, *Mat. Res. Bull.* **7**, 777 (1972)

[9]H. Amano, M. Kito, K. Hiramatsu, and I. Akasaki, *Jpn. J. Appl. Phys.* **28**, 2112 (1989)

[10]S. Nakamura, T. Mukai, M. Senoh, and N. Iwasa, *Jpn. J. Appl. Phys.* **31**, 139 (1992)

[11]S. Nakamura, M. Senoh, and T. Mukai, *Jpn. J. Appl. Phys.* **32**, 8 (1993)

[12]S. Nakamura, Y. Harada, and M. Senoh, *Appl. Phys. Lett.* **58**, 2021 (1991)

[13]S. Nakamura, M. Senoh, S. Nagahama, N. Iwasa, T. Yamada, T. Matsushita, Y. Sugimoto, and H. Kiyoku, *Appl. Phys. Lett.* **70**, 868 (1997)

[14]M. Khan, J. van Hoven, J. Kuznia, and D. Olson, *Appl. Phys. Lett.* **58,** 2408 (1991)

[15]P. Waltereit, O. Brandt, A. Trampert, H. T. Grahn, J. Menniger, M. Ramsteiner, M. Reiche and K. H. Ploog, *Nature*, **406**, 865–868 (2000)

[16]Y. Kobayashi, K. Kumakura, T. Akasaka and T. Makimot, *Nature*, **484**, 223–227 (2012)

[17]W. L. Wang, H. Yang and G. Q. Li, *J. Mater. Chem. C*, **1**,4070–4077 (2013)

[18]C. Y. Cho, N. Y. Kim, J. W. Kang, Y. C. Leem, S. H. Hong, W. Lim, S. T. Kim and S. J. Park, *Appl. Phys. Express*, **6**, 042102 (2013)

[19]Y. J. Zhao, S. H. Oh, F. Wu, Y. Kawaguchi, S. Tanaka, K. Fujito, J. S. Speck, S. P. DenBaars and S.Nakamura, *Appl. Phys. Express*, **6**, 062102 (2013)

[20]Y. J. Zhao, S. Tanaka, C. C. Pan, K. Fujito, D. Feezell, J. S. Speck, S. P. DenBaars and S. Nakamura, *Appl. Phys. Express*, **6**, 082104 (2013)

[21]N. Yukio, S. Masahiko, S. Takahiko, Y. Takao, M. Takashi. *Phys. Stat. Sol. A.* **205**, 1081 (2008)

[22]Y. Narukawa, M. Ichikawa, D. Sanga, M. Sanoand T. Mukai, *J. Phys. D: Appl. Phys.* **43** 354002 (2010)

[23]S. P. DenBaars, D. Feezell, K. Kelchner, S. Pimputkar, C. Pan,C. Yen, S. Tanaka, Y. Zhao, N. Pfaff, R. Farrell, M.Iza,S. Keller, U. Mishra, J. S. Speck, S. Nakamura, *ActaMaterialia*. **61,** 945-951 (2013)

[24]Q. Bao, M. Saito, K. Hazu, K. Furusawa, Y. Kagamitani, R. Kayano, D. Tomida, K. Qiao, T. Ishiguro, C. Yokoyama, and S. F. Chichibu, *Cryst. Growth Des.* **13**, 4158–4161 (2013)

[25]R. Kucharski, M. Zajac, R. Doradzinski, M. Rudzinski, R. Kudrawiec, and R. Dwilinski, *Semicond. Sci. Technol.* **27**, 024007 (2012)

[26]R. Dwilinski, R. Doradzinski, J. Garczynski, L. Sierzputowski, R. Kucharski, M. Zajac, M. Rudzinski, R. Kudrawiec, W. Strupinski, and J. Misiewicz, *Phys. Stat. Sol. A*. **208**,1489–1493 (2011)

[27]T. Paskova, D. A. Hanser, and K. R. Evans, *Proc. IEEE.* **98**, 1324–1338 (2010)

[28]T. Hanada, "Basic Properties of ZnO, GaN, and Related Materials", in Oxide and nitride semiconductors se - 1, Vol. **12**, edited by T. Yao and S.-K. Hong, Advances in Materials Research (Springer Berlin Heidelberg, 2009), pages 1–19

[29]N. Grandjean, B. Damilano, S. Dalmasso, M. Leroux, M. Lauugt and J. Massies, *J. Appl. Phys.* **86**, 3714 (1999)

[30]S. H. Park and S. L. Chung, *Appl. Phys. Lett.* **72**, 3103 (1998)

[31]M. Leroux, N. Grandjean, M. Laugt, J. Massies, B. Gil, P. Lefebvre and P. Bigenwald, *Phys. Rev. B* **58**, R13371 (1998)

[32]K. B. D. Cullity and S. R, Stock, *Elements of X-Ray Diffraction* **3**rd ed. (Englewood Cliffs, NJ: Prentice-Hall) (2001)

[33]A. D. Bykhovski, B. L. Gelmont, and M. S. Shur, *J. Appl. Phys.* **81**, 6332 (1997)

[34]C. F. Lin, J. H. Zheng, Z. J. Yang, J. J. Dai, D. Y. Lin, C. Y. Chang, Z. X. Lai, and C. S. Hong, *Appl. Phys. Lett.* **88**, 083121 (2006)

[35]Q. Wang, J. Bai, Y. P. Gong, and T. Wang, *J. Phys. D: Appl. Phys.* **44**, 395102 (2011)

[36]T. H. Hsueh, H. W. Huang, C. C. Kao, Y. H. Chang, M. C. Ou-Yang, H. C. Kuo, and S.C. Wang, *Jpn J. Appl. Phys.* **44**, 2661–2663 (2005)

[37]K. Xing, Y. Gong, J. Bai, and T. Wang, *Appl. Phys. Lett.* **99**, 181907 (2011)

[38]J. Iveland, L. Martinelli, J. Peretti, J. S. Speck, and C. Weisbuch, *Phys. Rev. Lett.* **110**, 177406 (2013)

[39]J. Cho, E. F. Schubert, and J. K. Kim, *Laser Photon. Rev.* **7**, 408–421 (2013)

[40]J. Hader, J. V. Moloney, and S. W. Koch, *Appl. Phys. Lett.* **96**, 221106 (2010)

[41]J. Hader, J. V. Moloney, and S. W. Koch, *Appl. Phys. Lett.* **99**, 181127 (2011)

[42]Y. C. Shen, G. O. Mueller, S. Watanabe, N. F. Gardner, A. Munkholm, and M. R.Krames, *Appl. Phys. Lett.* **91**, 141101 (2007)

[43]E. Kioupakis, P. Rinke, K. Delaney, and C. Van de Walle, *Appl. Phys. Lett.* **98**, 161107 (2011)

[44]J. Hwang, R. Hashimoto, S. Saito, and S. Nunoue, *Jpn. J. Appl. Phys.* **52**, 08JL13 (2013)

[45]M. R. Krames, O. B. Shchekin, R. Mueller-Mach, G. O. Mueller, L. Zhou, G. Harbers, and M. G. Craford, *J. Display Technol.* **3**, 160–175 (2007)

[46]IPCC, Summary for Policymakers. In: Climate Change 2007: The Physical Science Basis. Contribution of Working Group I to the Fourth Assessment Report of the Intergovernmental Panel on Climate Change, technical report (Cambridge University Press, Cambridge, United Kingdom and New York, NY, USA, 2007)

[47] University of Ulm, "*Lecture Notes in Optoelectronics, ScholzF.*" http://www-opto.e-technik.uni-ulm.de/lehre/cs/ (Accessed 16/09/2013)

[48]Stony Brook University, "*Lecture Notes 4 in The structure and Entropy of Ice, Marivi "*, http://mini.physics.sunysb.edu/~marivi/TEACHING-OLD/PHY313/doku.php?id=lectures:4 (Accessed 16/09/2015)

[49]R. J. Molnar, W. Götz, L. T. Romano, and N. M. Johnson, *J. Cryst. Growth* **178**, 147 (1997)

[50]S. Nakamura, Y. Harada, and M. Seno, *Appl. Phys. Lett*. **58**, 2021 (1991)

[51]H. Amano, N. Sawaki, I. Akasaki, and Y. Toyoda, *Appl. Phys. Lett.* **48**, 353 (1986)

[52]R. J. Malik, "III-V Semiconductor Materials and devices", north-Holand (1989)

[53]S. C. Jain, M. Willander, J. Narayan, and R. Van Overstraeten, *J. Appl. Phys.* **87**, 965 (2000)

[54]M. A. L. Johnson, Z. Yu, J. D. Brown, F. A. Koeck, N. A. El-Masry, H. S. Kong, J. A.

Edmond, J. W. Cook, and J. F. Schezina, *MRS Internet J. Nitride Semicond. Res.* **4S1**, G5.10 (1999)

[55]H. Moffat, and K. F. Jensen, *J. Cryst. Growth.* **77**, 108 (1986)

[56]S. A. Kukushkin, A. V. Osipov, V. N. Bessolov, B. K. Medvedev, V. K. Nevolin, and K. A. Tcarik, *Rev. Adv. Mater. Sci.* **17**, 1 (2008)

[57]R. Liu, A. Bell, F. A. Ponce, C. Q. Chen, J. W. Yang and M. A. Khan, *Appl. Phys. Lett.* **86** 021908 (2005)

[58]P. P. Paskov and B. Monermar, *Nitrides with Nonpolar Surfaces: Growth, Properties and Devices* ed T. Paskova (Weinheim:Wiley-VCH) chapter **8**, pp 185–217

[59]J. Bai, T. Wang, P. J. Parbrook, and A. G. Cullis, *Appl. Phys. Lett*. **89**, 131925 (2006)

[60]T. Palacios, F. Calle, M. Varela, C. Ballesteros, E. Monroy, F. B. Naranjo, M. A. Sa´nchez-Garcı´a, E.Calleja, E. Mun˜oz, *Semicond. Sci. Technol.* **15**, 996 (2000)

[61]H. M. Ng, N.G. Weimann, A. Chowdhury, *J. Appl. Phys.* **94**, 650(2003)

[62]H. M. Ng, A. Chowdhury, W. Parz, N. G. Weimann, the Electrochemical Society: State-of-the-Art Program on Compound Semiconductors XXXIX and Nitride and Wide Band gap Semiconductors for Sensors, Photonics and Electronics IV, vol. **2003**, pp 3 (2003)

[63]H. M. Ng, W. Parz, N.G. Weimann, A. Chowdhury, *Jpn. J. Appl. Phys.* Part 2, **42**, L1405 (2003)

[64]D. Huang, P. Visconti, K. M. Jones, M. A. Reshchikov, F. Yun, A. A. Baski, T. King, H. Morkoc, *Appl. Phys. Lett.* **78**, 4145 (2001)

[65]P. Visconti, K. M. Jones, M.A. Reshchikov, R. Cingolani, H. Morkoc¸, R. J. Molnar, *Appl. Phys. Lett.* **77**, 3532 (2000)

[66]P. Visconti, D. Huang, M. A. Reshchikov, F. Yun, T. King, A. A. Baski, R. Cingolani, C. W. Littion, J. Jasinski, Z. Liliental-Weber, H. Morkoc, *Phys. Stat. Sol. B.* **228** (2), 513(2001)

[67]P. Visconti, D. Huang, F. Yun, M. A. Reshchikov, T. King, R. Cingolani, J. Jasinski, Z. Liliental-Weber and H. Morkoc, *Phys. Stat. Sol. A.***190** (1), 5 (2002)

[68]P. Visconti, D. Huang, M. A. Reshchikov, F. Yun, R. Cingolani, D. J. Smith, J. Jasinski, W. Swider, Z. Liliental-Weber and H. Morkoc, *Mater. Sci. Eng.* B **93** 229 (2002)

[69]D. Zhuang, J. H. Edgar, *Mater. Sci. Eng.* R **48**, 1–46 (2005)

[70]M. Frentrup, S. Ploch, M. Pristovsek, and M. Kneissl, *Phys. Stat. Sol. B.* **248**, 583

(2011)

[71]Z. Bougrioua, M. Laügt, P. Vennéguès, I. Cestier, T. Gühne, E. Frayssinet, P. Gibart, and M. Leroux, *Phys. Stat. Sol. A.* **204**, 282–289 (2007)

[72]Y. Enya, Y. Yoshizumi, T. Kyono, K. Akita, M. Ueno, M. Adachi, T. Sumitomo, S. Tokuyama, T. Ikegami, K. Katayama and T. Nakamura, *Appl. Phys. Express* **2**, 082101 (2009)

[73]Y. Zhao, Q. Yan, C. Y. Huang, S. C. Huang, P. S. Hsu, S. Tanaka, C. C. Pan, Y. Kawaguchi, K. Fujito,C. G. Van de Walle, J. S. Speck, S. P. DenBaars, S. Nakamura, and D. Feezell, *Appl. Phys. Lett.* **100**, 201108 (2012)

[74]P. D. Mierry, T. Guehne, M. Nemoz, S. Chenot, E. Beraudo, and G. Nataf, *Jpn J. Appl. Phys.* Part 2 **48**, 031002 (2009).

[75]M. T. Hardya, D. F. Feezella, S. P. DenBaars, and S. Nakamura, *Mater. Today* **14**, P408-415 (2011)

[76]J. E. Northrup, *Appl. Phy. Lett.* **95**, 133107 (2009)

[77]F. Scholz, *Semicond. Sci. Technol.* **27** 024002 (15pp) (2012)

[78]B. Liu, R. Smith, M. Athanasiou, X. Yu, J. Bai, and T. Wang, *Appl. Phys. Lett.* **105**, 261103 (2014)

[79]M. J. Kappers, J. L. Hollander, C. McAleese, C. F. Johnston,R. F. Broom, J. S. Barnard, M. E, Vickers, C. J. Humphreys, *J. Cryst. Growth.* **300**, 155 (2007)

[80]T. Matsuoka, and E. Hagiwara, *Phys. Stat. Sol. A.* **188**, 485 (2001)

[81]M. Frentrup, S. Ploch, M. Pristovsek, and M. Kneissl, *Phys. Stat. Sol. B*. **248**, 583 (2011)

[82]T. J. Baker, B. A. Haskell, F Wu U, J. S. Speck and S. Nakamura, *Jpn. J. Appl. Phys.* **45**, No. 6, L154-157 (2006)

[83]R. Sharma, P. M. Pattison, H. Masui, R. M. Farrell, T. J. Baker, B. A. Haskell, F. Wu, S. P. DenBaars, J. S. Speck, and S. Nakamura, *Appl. Phys. Lett.* **87**, 231110 (2005)

[84]T. Sasaki and S. Zembutsu, *J. Appl. Phys.* **61**, 2533 (1987)

[85]P. Waltereit, O. Brandt, A. Trampert, H. T. Grahn, J. Menniger, M. Ramsteiner, M. Reiche and K. H. Ploog, *Nature (London)* **406**, 865 (2000)

[86]T. Wang, J. Bai, P. J. Parbrook, and A. G. Cullis, *Appl. Phys. Lett.* **87**, 151906 (2005)

[87]P. de Mierry, N. Kriouche, M. Nemoz and G. Natal, *Appl. Phys. Lett*. **94**, 191903

(2009)

[88]P. Fini, L. Zhao, B. Moran, M. Hansen, H. Marchand, J. P. Ibbetson, S. P. DenBaars, U. K. Mishra, and J. S. Speck, *Appl. Phys. Lett.* **75**, 1706 (1999)

[89]K. Hiramatsu, K. Nishiyama, M. Onishi, H. Mizutani, M. Narukawa, A. Motogaito, H. Miyake, Y. Iyechika, and T. Maeda, *J. Cryst. Growth* **221**, 316 (2000)

[90]B. Imer, F. Wu, S. P. DenBaars, and J. S. Speck, *Appl. Phys. Lett*. **88**, 061908 (2006)

[91]K. Linthicum, T. Gehrke, D. Thomson, E. Carlson, P. Rajagopal, T. Smith, D. Batchelor, and R. Davis, *Appl. Phys. Lett*. **75**, 196 (1999)

[92]I. Kidoguchi, A. Ishibashi, G. Sugahara, and Y. Ban, *Appl. Phys. Lett*. **76**, 3768 (2000)

[93]B. A. Haskell, F. Wu, M. D. Craven, S. Matsuda, P. T. Fini, T. Fujii, K. Fujito, S. P. DenBaars, J. S. Speck, and S. Nakamura, *Appl. Phys. Lett.* **83**, 644 (2003)

[94]D. Iida, M. Iwaya, S. Kamiyama, H. Amano, and I. Akasaki, *J. Cryst. Growth* **311**, 2887 (2009)

[95]J. Bai, Y. Gong, K. Xing, X. Yu, and T. Wang, *Appl. Phys. Lett.* **102**, 101906 (2013)

[96]Y. Gong, K. Xing, B. Xu, X. Yu, Z. Li, J. Bai and T. Wang, *ECS Trans.* **66**, (1) 151-155 (2015)

[97]R. Ravash, J. Blaesing, A. Dadgar and A. Krost, *Appl. Phys. Lett*. **97**, 142102 (2010)

[98]T. Tanikawa, T. Hikosaka, Y. Honda, M. Yamaguchi, and N.Sawaki, *Phys. Stat. Sol. C.* **5**, 2966 (2008)

[99]M. Yang, H. S. Ahn, T. Tanikawa, Y. Honda, M. Yamoguchi and N. Sawaki, *J. Cryst. Growth* **311**, 2914 (2009)

[100]H. Ishikawa, K. Yamamoto, T. Egawa, T. Soga, T. Jimboand M. Umeno, *J. Cryst. Growth* **189-190,** 178 (1998)

[101]X. Yu, Y. Hou, S. Shen, J. Bai, Y. Gong, Y. Zhang, and Tao Wang, *Phys. Stat. Sol. C.* **13**, 1–5 (2016)

[102]Y. Yoshizumi, M. Adachi, Y. Enya, T. Kyono, S. Tokuyama, T. Sumitomo, K. Akita, T. Ikegami, M. Ueno, K. Katayama and T. Nakamura, *Appl. Phys. Express* **2**, 092101 (2009)

[103]R. Kucharski, M. Zajac, R. Doradzinski, J. Garcynski, L. Sierzputowski, R. Kudrawiec, J. Serafinczuk, J. Misiewica and R. Dwilinski, *Appl. Phys. Express* **3**, 101001 (2010)

[104]M. Yang, H. S. Ahn, T. Tanikawa, Y. Honda, M. Yamoguchi and N. Sawaki, *J. Cryst.*

Growth **311**, 2914 (2009)

[105]N. Suzuki, T. Uchida, T. Tanikawa, T. Hikosaka, Y. Honda, M. Yamaguchi, and N. Sawaki, *J. Cryst. Growth* **311**, 2875(2009)

[106]T. J. Baker, B. A. Haskell, F Wu U, P. T. Fini, J. S. Speck and S. Nakamura, *Jpn. J. Appl. Phys*. **44**, L920-L922 (2005)

[107]S. N. Lee, H. S. Paek, H. Kim, Y. M. Park, T. Jang, and Y. Park, *Appl. Phys. Lett.* **92**, 111106 (2008)

[108]X. Ni, U. Ozgur, A. A. Baski, H. Morkoc, L. Zhou, D. J. Smith, and C. A. Tran, *Appl. Phys. Lett.* **90**, 182109 (2007)

[109]T. Guhne, Z. Bougrioua, P. Vennegues, M. Leroux, and M. Albrecht, *J. Appl.Phys.* **101**, 113101 (2007)

[110]P. Vennegues, Z. Bougrioua, and T. Guehne, Jpn. *J. Appl. Phys.* **46**, 4089 (2007)

[111]N. Kriouche, M. Lerous, P. Vennegues, M. Nemoz, G. Nataf, and P. deMierry, *Nanoscale Res. Lett.* **5**, 1878 (2010)

[112]S. A. Smith, C. A. Wolden, M. D. Bbremser, A. D. Hanser, R. F. Davis, and W. V. Lampert, *Appl. Phys. Lett.* **71**, 3631 (1997)

[113]R. J. Shul, G. B. McClellan, S. A. Casalnuovo, D. J. Rieger, S. J. Pearton, C. Constantine, and C. Barratt, *Appl. Phys. Lett.* **69**, 1119 (1996)

[114]J. K. Sheu, Y. K. Su, G. C. Chi, M. J. Jou, C. C. Liu, C. M. Chang, and W. C. Hung, *J. Appl. Phys.* **85**, 1999 (1970)

[115]T. Palacios, F. Calle, M. Varela, C. Ballesteros, E. Monroy, F.B. Naranjo, M.A. Sánchez-Garcia, E. Calleja, E. Munöz, *Semicond. Sci. Technol.* **15**, 996 (2000)

[116]H. M. Ng, N. G. Weimann, A. Chowdhury, *J. Appl. Phys.* **94**, 650 (2003)

[117]F. Bernardini, V. Fiorentini and D. Vanderbilt, *Phys. Rev.B* **56**,R10024 (1997)

[118]F. Ranalli, P. J. Parbrook, J. Bai, K. B. Lee, T. Wang and A. G. Cullis, *Phys. Stat. Sol. C* **6**, S780 (2009)

[119]Q. Sun, B. Leung, C. D. Yerino, Y. Zhang, J. Han, *Appl. Phys. Lett.* **95** 231904 (2009)

[120]F. Ranalli, P. J. Parbrook, J. Bai, K. B. Lee, T. Wang, and A. G. Cullis, *Phys. Status Solidi C* **6**, S780 (2009)

[121]Z. Cai, K. A. Vallis, and R. M. Reilly, *Int. J. Radiat. Biol.* **85**, 262 (2009)

[122]T. Collins, *BioTechniques* **43**, S25 (2007)

[123]C. A. Schneider, W. S. Rasband, and K. W. Eliceiri, *Nature Methods* **9**, 671 (2012)

[124]B. Leung, Q. Sun, C. Yerino, Y. Zhang, J. Han, B. H. Kong, H. K. Cho, K. Y. Liao, and Y. L. Li, *J. Cryst. Growth* **341**, 27–33 (2012)

[125]S. N. Lee, J. Kim, and H. Kim, *J. Electrochem. Soc.* **158**, H994–H996 (2011)

[126]M. A. Moram and M. E. Vickers, *Rep. Prog. Phys.* **72**, 036502 (2009)

[127]S. Jung, S. Lee and H. Kim, *Appl. Phys. Lett.* **102**, 151603 (2013)

[128]S. Jang, H. Kim, D. S. Kim, S. M. Hwang, J. Kim and K. H. Baik, *Appl. Phys. Lett.* **103**, 162103 (2013)

[129]C. Jung, J. Jang, J. Hwang, J. Jeong, J. Kim, K. Lee and O. Nam, *J. Cryst Growth* **370**,26-39 (2013)

[130]D. Zhuang, J.H. Edgar, *Mater. Sci. Eng.* R **48,** 1–46 (2005)

[131]D. Li, M. Sumiya, S. Fuke, D. Yang, D. Que, Y. Suzuki, Y. Fukuda, *J. Appl. Phys.* **90**, 4219 (2001)

[132]K. Xing, 'Fabrication and Overgrowth of Semi-polar and Non-polar GaN on Sapphire for Advanced III-nitride Optoelectronics' Ph.D. thesis, University of Sheffield, Sheffield UK (2015)

[133]Y. Zhang, J. Bai, Y. Hou, R. M. Smith, X. Yu, Y. Gong and T. Wang, *AIP Adv.* **6**, 025201 (2016)

[134]K. Minami, *SID Symposium Digest of Technical Papers* **45**, 1, 839-841 (2014)

[135]K. Deisseroth, *Nat. Methods* **8**, 1 (2011)

[136]D. Tsonev, H. Chun, S. Rajbhandari, J. J. McKendry, S. Videv, E. Gu, M. D. Dawson, *IEEE Photonics Technol. Lett.* **26**, 7, (2014)

[137]T. Wang, *Semicond. Sci. Technol.* **31**, 9, (2016)

[138]H. Asamizu, M. Saito, K. Fujito, J. S. Speck, S. P. DenBaars, S. Nakamura, *Appl. Phys. Exp.* **1**, 9, (2008)

[139]Y. Enya, Y. Yoshizumi, T. Kyono, K. Akita, M. Ueno, M. Adachi, T. Nakamura, *Appl. Phys. Exp.* **2**, 8, (2009)

[140]T. Gühne, Z. Bougrioua, P. Vennéguès, M. Leroux, M. Albrecht, *J. Appl. Phys.* **101**, 11, (2007)

[141]H. Amano, T. Asahi, I. Akasaki, *Jpn. J. Appl. Phys.* **29**, 2A, (1990)

[142]A. S. Zubrilov, V. I. Nikolaev, D. V. Tsvetkov, V. A. Dmitriev, K. G. Irvine, J. A. Edmond,

C. H. Carter Jr., *Appl. Phys. Lett.* **67***,* 4, (1995)

[143]S. Kurai, Y. Naoi, T. Abe, S. Ohmi, S. Sakai, *Jpn. J. Appl. Phys.* **35**, 1B, (1996)

[144]K. L. Shaklee, R. E. Nahory and R. F. Leheny, *J. Lumin.* **7**, 284 (1973)

[145]T. Oto, R. G. Banal, M. Funato, and Y. Kawakami, *Appl. Phys. Lett.* **104**, 181102 (2014)

[146]H. Kalt, M. Umlauff, M. Kraushaar, M. Scholl, J. Sollner, and M. Heuken, *J. Cryst. Growth* **184**, 627 (1998)

[147]A. Strittmatter, J. E. Northrup, N. M. Johnson, M. V. Kisin, P. Spiberg, H. El-Ghoroury, A. Usikov, and A. Syrkin, *Phys. Stat. Sol. B* **248,** 561 (2011)

[148]N. Okada, K. Uchida, S. Miyoshi, and K. Tadatomo, *Phys. Stat. Sol. A* **209**(3), 469 (2012)

[149]D. Min, G. Yoo, Y. Ryu, S. Moon, K. Nam, H. Lim, and O. Nam, *Jpn. J. Appl. Phys.*, Part 1 **52**, 10MA03 (2013)

[150]T. Hikosaka, T. Tanikawa, Y. Honda, M. Yamaguchi, and N. Sawaki, *Phys. Stat. Sol. C*, **5**(6), 2234 (2008)

[151]J. Jeong, J. Jang, J. Hwang, C. Jung, J. Kim, K. Lee, H. Lim, and O. Nam, *J. Cryst. Growth*, **370**, 114 (2013)

[152]Y Gong, K Xing, B Xu, X Yu, Z Li, J Bai, Tao Wang, *ECS Transactions* **66**, 151 b (2015)

[153]H. R. Yi, K. R. Song, S. H. Han, J. H. Lee, and S. N. Lee, *J. Vac. Sci. Technol. B* **31**, 061208 (2013)

[154]F. Tendille, P. DeMierry, P. Vennéguès, S. Chenot, and M. Teisseire, *J. of Cryst. Growth* **404**, 177 (2014)

[155]R. Sharma, P. M. Pattison, H. Masui, R. M. Farrell, T. J. Baker, B. A. Haskell, F. Wu, S. P. DenBaars, J. S. Speck, and S. Nakamura, *Appl. Phys. Lett.* **87**, 231110 (2005)

[156]R. M. Smith, B. Xu, K. Xing, Y. Gong, X. Yu, Y. Zhang, Y. Hou, J. Bai, and T. Wang, "An optical study of the influence of basal plane stacking faults on semi-polar (11-22) InGaN/InGaN quantum wells," *NanoLett.* (submitted)

[157]H. Masui, A. Chakraborty, B. A. Haskell, U. K. Mishra, J. S. Speck, S. Nakamura, and S. P. Denbarrs, *Jpn. J. Appl. Phys., Part 2* **44**, L1329–L1332 (2005)

[158]M. Athanasiou, R. M. Smith, Y. Hou, Y. Zhang, Y. Gong, and T. Wang, *Appl. Phys. Lett.* **107**, 141110 (2015).